
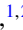



Ab initio Van der Waals electrostatics: Polaritons and electron scattering from plasmons and phonons in BN-capped graphene

Francesco Macheda ¹, Francesco Mauri ^{1,2} and Thibault Sohier ³

¹*Dipartimento di Fisica, Università di Roma La Sapienza, Piazzale Aldo Moro 5, I-00185 Roma, Italy*

²*Istituto Italiano di Tecnologia, Graphene Labs, Via Morego 30, I-16163 Genova, Italy*

³*Laboratoire Charles Coulomb (L2C), Université de Montpellier, CNRS, 34095 Montpellier, France*

 (Received 21 March 2024; revised 9 August 2024; accepted 14 August 2024; published 3 September 2024)

Plasmons and polar phonons are elementary electrodynamic excitations of matter. In two dimensions and at long wavelengths, they couple to light and act as the system polaritons. They also dictate the scattering of charged carriers. Van der Waals heterostructures offer the opportunity to couple excitations from different layers via long-range Coulomb interactions, modifying both their dispersion and their scattering of electrons. Even when the excitations do not couple, they are still influenced by the screening from all layers, leading to complex dynamical interactions between electrons, plasmons, and polar phonons. We develop an efficient *ab initio* model to solve the dynamical electric response of Van der Waals heterostructures, accompanied by a formalism to extract relevant spectroscopic and transport quantities. Notably, we obtain scattering rates for electrons of the heterostructure coupling remotely with electrodynamic excitations. We apply those developments to BN-capped graphene, in which polar phonons from BN couple to plasmons in graphene. We study the nature of the coupled excitations, their dispersion and their coupling to graphene's electrons. Regimes driven by either phonons or plasmons are identified, as well as a truly hybrid regime corresponding to the plasmon-phonon-polariton at long wavelengths. Those are studied as a function of the graphene's Fermi level and the number of BN layers. In contrast with standard descriptions in terms of surface-optical phonons, we find that the electron-phonon interaction stems from several different modes. Moreover, the dynamical screening of the coupling between BN's LO phonons and graphene's electrons crosses over from inefficient to metal-like depending on the relative value of the phonons' frequency and the energetic onset of interband transitions. While the coupling is significant in general, the associated scattering of graphene's carriers is found to be negligible with respect to the particularly large one coming from intrinsic phonons in the context of electronic transport.

DOI: [10.1103/PhysRevB.110.115407](https://doi.org/10.1103/PhysRevB.110.115407)

I. INTRODUCTION

Van der Waals heterostructures [1,2] (vdWH) have emerged as some of the most promising ways to explore and exploit the properties of materials at the nanoscale [3]. Stacking different layers of two-dimensional (2D) materials offers the opportunity to tailor novel properties. Unsurprisingly, this comes with some challenges on the modeling side. The electrodynamic response of a material, i.e., the response to a momentum and frequency-dependent electric potential $V(\mathbf{q}, \omega)$, dictates a wide range of physical properties. This is evident from the fundamental importance of the inverse screening function [4] in describing optical and electronic properties. The electrodynamic elementary excitations of the system are intrinsic, self-sustained collective modes driven by long-range electromagnetic interactions [5]. This work will focus on plasmons and polar phonons, that is collective oscillations of electronic or atomic plasma. Other excitations such as excitons or magnons are out of scope.

In 2D and at long wavelengths, longitudinal plasmons and phonons couple to light [6–8]. The resulting light-matter quasiparticles, polaritons, are usually discussed at momenta close to the light cone ($q_0 \gtrsim \omega/c$, where c is the speed of light). However, highly confined plasmon- and phonon-polaritons [9–16] in 2D materials have been observed at

momenta 10 to 100 times larger. Those can be studied without accounting for relativistic retardation effects, as will be done here. Electrodynamic collective modes in general are also a major source of scattering, via remote interactions between layers [17,18]. A good understanding and predictive models for the emerging interlayer couplings between collective modes thus lead to the exciting prospect of engineering light-matter interactions [6,7] and electron scattering [19] in future photonic and electronic devices based on vdWH.

To obtain polariton dispersions, one can resort to empirical and analytical approaches such as continuum electrodynamics (EDC) solved with the transfer matrix method [20–22]. Those top-bottom approaches rely on parametrized models for the dielectric functions of the bulk parent materials. This parametrization can become challenging when the heterostructure is made of several layer types, some of which not as extensively studied as graphene or hexagonal BN. In addition, those approach typically yield a limited number of physical observables (reflection, transmission). EDC-like models have been used to obtain more complex quantities like electron scattering involving coupled plasmons and phonons [23–27], but their complexity quickly grows with the size and diversity of the vdWH, ultimately requiring some simplifications to be tractable.

To be predictive in complex systems, a bottom-up, microscopic *ab initio* approach that directly simulates the electrodynamic response of vdWH is highly desirable. Unfortunately, direct *ab initio* calculations of vdWH including plasmonic and phononic excitations are costly. Indeed, lattice mismatches imply large supercells which in addition to the number of layers increases considerably the number of atoms in the simulation cell. Another strategy is to coarse-grain the layer properties and focus on interlayer interactions. The single-layer quantities are easily obtained from first principles, and used in a model to build the properties of the multilayer. In the current framework, this amounts to extracting single-layer dynamical responses from *ab initio*, and model the multilayer response. This seamlessly allows to build the response of arbitrarily complex stacks containing many different layers.

We build on a previous work based on this strategy in the static limit [19] and add dynamical electronic and atomic contributions. With respect to similar efforts in the literature [28–31], the Van der Waals electrodynamics (VED) model presented here offers both technical and conceptual improvements.

Technical improvements include the full momentum-dependent phononic response, rather than resorting to the long-wavelength limit of Born effective charge models [29], which are shown to fail at larger momenta relevant for transport. Here, we show that VED results in the static limit match density functional perturbation theory (DFPT) results in terms of both dispersion and intensity of the collective modes. This supports the validity and accuracy of VED beyond the static limit, i.e., in the dynamical regime not accessible by standard DFPT techniques due to the Born-Oppenheimer approximation. Thus, the VED method goes beyond the capabilities of current first-principles calculations with a comparable accuracy and a negligible computational cost. Further, matching DFPT results also supports that interlayer interactions can be neglected in the systems studied, since they are included in DFT calculations.

Conceptual progress stems from a simple yet powerful setup and exploitation of the formalism. We first build a matrix describing the response of given layer when a potential perturbation is applied to another layer. The imaginary part of this matrix yields the elementary excitations of the vdWH. From those, the response to an arbitrary external potential or charge density perturbation can be reconstructed and then projected on a given probe. When perturbation and probe are uniform over the layers, the model yields the basic spectroscopic properties of the slab, such as the electronic energy loss spectroscopy (EELS) cross-section in transmission. More complex quantities describing surface-probing experiments can also be extracted, providing realistic comparison between theoretical predictions and experiments performing polariton interferometry via scattering-type scanning near-field optical microscopy (sSNOM) [32,33]. Another significant progress achieved by this work is the extraction of scattering rates for electrons coupling with plasmons, phonons, and hybrid excitations [23,26,27,34], obtained by perturbing and probing with a charge density localized on a given layer. Such *ab initio* calculation of interlayer electron scattering mechanism, including

dynamical screening from electrons and phonons, opens exciting perspectives for the study of vdWH. Indeed, they can be used for transport calculations [24,27,35–41], Raman scattering [42–44], excited carriers relaxation [17,45–49], and superconductivity [50–52]. Note that combining the long-range electrodynamic interactions described by VED with state-of-the-art DFPT calculations of short-range intralayer electron-phonon interactions [53,54], one reaches a complete description of intrinsic scattering mechanisms in vdWHs.

We focus here on graphene encapsulated with multilayer hexagonal boron nitride, a prototypical vdWH system both for polaritonics and electronic transport. It hosts both charge plasmons from graphene and polar phonons from BN. Their coexistence in the same energy range leads to their mixing and anticrossing [12,26,55]. We present an extensive exploitation of the VED framework, discussing spectroscopic spectral functions and electron scattering including contributions from plasmons, phonons, and hybrid excitations. We analyze the contributions of different layers to gain insight on the nature of the excitations (plasmon, phonon, or hybrid), and propose a method to separate the corresponding scattering strengths. We study the impact of two main parameters for BN-capped graphene, i.e., the number of BN layers and the Fermi level (electron doping) of graphene, that can be tuned experimentally [56,57] to change the properties of the plasmons, phonons, and their scattering of electrons. We focus notably on the nature of the polaritonic states, and the dynamical screening of the remote coupling between graphene’s electrons and BN’s LO phonons. Gaining access to the microscopic origin of the interactions, we progress over state-of-the-art modeling and show that in realistic systems the remote coupling is mediated by several different LO phonon branches rather than a single surface-optical phonon [58]. Finally, we assess the impact of our findings on graphene’s resistivity at room temperature.

The paper is structured as follows. Section II describes the theoretical and computational frameworks. Section III describes the collective modes of the BN/graphene systems. Section III A considers graphene’s plasmons and BN’s phonons before coupling, validating the method against known results and DFPT calculations. Section III B explores the nature of the excitations in the coupled system, as well as their dependence on the number of BN layers and graphene’s Fermi level. Finally, Sec. IV studies the coupling of graphene’s electrons with those collective modes, and compares the associated scattering rates to those associated with graphene’s intrinsic optical modes.

II. ELECTRODYNAMIC RESPONSE OF VAN DER WAALS HETEROSTRUCTURES

The density-density response of a system at momentum q and frequency ω , $\chi(q, \omega)$, enters the determination of many physical quantities, from spectroscopic responses to intrinsic scattering mechanisms. This section first shows how the VED model builds the response of a layered heterostructure from single-layer responses. Then, it shows how it can be used to obtain the collective modes dispersions, their EELS and surface-probes responses, and their coupling to electrons to deduce scattering rates.

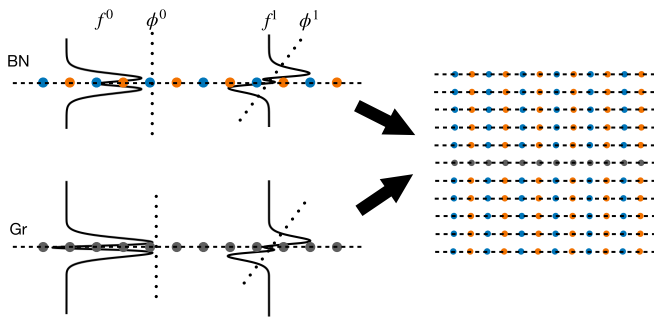


FIG. 1. Sketch of the Van der Waals electrostatics (VED) model. Single-layer monopole (f^0) and dipole (f^1) density responses to even (ϕ^0) and odd (ϕ^1) potentials are extracted from DFPT. This is then used to build the multilayer response to arbitrary potential or charge perturbation.

A. Van der Waals electrostatics (VED) model

The VED is the dynamical generalisation of the model developed in Ref. [19]. The general idea, sketched in Fig. 1, is to build the electrodynamic response of a layered vdWH from the response of appropriately defined building blocks, usually single layers. The model provides an accurate description of the interplay between electrodynamic excitations from 2D building blocks that are coupled via long range Coulomb interactions. In cases where other interlayer interactions significantly modify the excitations, e.g., flat bands in twisted bilayer graphene, the building blocks need not be single layers. The vdWH can and should be course-grained to the appropriate building blocks, e.g., twisted bilayer graphene. The following methodology is general, but we will specialize to BN-capped graphene as a prototypical system. The response of each different layer is simulated and parametrized from first principles. The static, clamped-ions electronic response is directly extracted from density functional perturbation theory (DFPT) calculations, therefore including local-fields and exchange-correlation effects. The dynamical contribution from free carriers is modeled within the random phase approximation (RPA), equivalent to a time-dependent Hartree theory without local-fields. The dynamical atomic response is evaluated from DFPT ingredients. The *ab initio* simulation of the whole vdWH, very costly even in the static Born-Oppenheimer approximation of DFPT, is avoided. Direct *ab initio* simulations of the interplay of dynamical contributions from plasmons and phonons would further require time-dependent density-functional theory, extremely costly in large supercells.

Here, the dynamical response of the full vdWH is obtained by solving a self-consistent set of equations that determine the potentials and charges on each layer. The computational burden of our method is limited to the single-layer static DFPT response calculations needed for each different kind of layer, plus a small overhead to solve the coupled equations of the VED model [59]. The single-layer responses are easily parametrized and stored, such that for all vdWH combining layers in the database, only the VED coupled equations are left to solve. The main approximation of this methodology is to neglect the wave-function overlap between layers. This essentially comes down to an interlayer

coarse-graining approximation where different layers see each other only through average macroscopic potentials. This approximation holds remarkably well in vdWH, where the interlayer bonds are weak by definition.

1. General definitions

The general aim is to simulate the macroscopic charge density response of the vdWH to a macroscopic external potential. When working with screening and dielectric properties in 2D, it is preferable to Fourier transform only the in-plane space variables ($x, y \rightarrow \mathbf{q}$), while keeping the full out-of-plane z dependence of the response. The external potential perturbation $V_{\text{ext}}(\mathbf{q}, \omega, z)$ is thus periodic in-plane and monochromatic at momentum \mathbf{q} and frequency ω . The total charge density response $\rho(\mathbf{q}, \omega, z)$ is determined by both the rearrangement of the electronic cloud and the displacement of the pointlike ions. For both electrons and atoms, the responses are assumed to be isotropic in the plane, depending only on $q = |\mathbf{q}|$. This is usually a good approximation for many 2D material (e.g., hexagonal materials like BN and graphene). Within linear response theory, the charge density is obtained via the density-density response function χ as

$$\rho(q, \omega, z) = \int dz' \chi(q, \omega, z, z') V_{\text{ext}}(q, \omega, z'). \quad (1)$$

The integration in the out-of-plane variable is meant to cover all the space, since z is free of periodic boundary conditions. The connection between the total and the external potential is then given by the inverse dielectric matrix

$$\epsilon^{-1}(q, \omega, z, z') = \delta(z - z') + \frac{2\pi e^2}{q} \int dz'' e^{-q|z-z''|} \times \chi(q, \omega, z'', z'). \quad (2)$$

The possibility of having any kind of external potential has to be reduced to have a tractable problem, while at the same time maintaining the main physical features of the perturbations. Therefore, we find it useful to restrict the z dependence of the external potential to a simplified functional form. As formalized in the following section, we follow the approach of Ref. [19], which is an approximation of the exact method of Ref. [60].

2. Dual basis set

To write the response problem in an easily solvable matrix form, the first step is to approximate the continuous out-of-plane variables of the response function of Eq. (1) with discrete indices over the layers. For each layer, $V_{\text{ext}}(z)$ is expanded over N_b elements composing a subset of a complete basis set. The induced density can itself be expressed as a linear combination of (different) N_b basis vectors. Equation (1) then transforms into a matrix equation with densities and potentials expanded over a dual basis set (in the same spirit as Ref. [28]).

We start by defining the mapping between the out-of-plane coordinate z and the layer index. For N_l layers, $k \in \{1, \dots, N_l\}$ and

$$z \in [z_k - d/2, z_k + d/2] \rightarrow k. \quad (3)$$

We assume that each layer has a finite thickness d in the out-of-plane direction around its central coordinate z_k , within which the density response is fully contained. d depends on the kind of layer but for simplicity, here, we take it to be layer independent. Within the “boxes” defined in Eq. (3), we define the restricted ($N_b = 2$) basis set for the external potential in the form

$$\phi_k^i(z) = \begin{cases} (z - z_k)^i & z \in k \\ 0 & z \notin k \end{cases}, \quad (4)$$

with $i = 0, 1$. Analogously, we define the restricted basis set for the densities as

$$f_k^i(z) = \begin{cases} \mathcal{F}_k^i(z - z_k) & z \in k \\ 0 & z \notin k \end{cases}, \quad (5)$$

which we refer to as profile functions. $\mathcal{F}_k^i(z)$ are the normalized out-of-plane profiles of the density response to the basis potentials of Eq. (4) when the k layer is placed at $z_k = 0$, as depicted in Fig. 1. They separate the density response into monopolar (z -symmetric, $i = 0$) and dipolar (z -antisymmetric, $i = 1$) components. In principle, they might depend on q and ω . However, we have observed negligible dependence on q and assume the same for ω , as discussed in Sec. II A 6. The profile functions [Eq. (A2) of Ref. [19]] are normalized as

$$\int dz f_k^i(z) \phi_l^j(z) = \delta_{ij} \delta_{kl}. \quad (6)$$

The admitted potentials in our problem can now be written as

$$V(q, \omega, z) = \sum_{ik} V_k^i(q, \omega) \phi_k^i(z), \quad (7)$$

$$V_k^i(q, \omega) = \int dz f_k^i(z) V(q, \omega, z). \quad (8)$$

Similarly, for the density

$$\rho(q, \omega, z) = \sum_{ik} \rho_k^i(q, \omega) f_k^i(z), \quad (9)$$

$$\rho_k^i(q, \omega) = \int dz \phi_k^i(z) \rho(q, \omega, z). \quad (10)$$

Notice that in Eq. (1) and in the RPA, the induced density is the sum of two contributions due to the purely electronic polarization (“el”) and the atomic (phonon) mediated one (“ph”). Since the observables that we study in this work are integrated quantities along z , it is convenient to approximate atomic polarization to have the same z profile of the electronic one, with a small error as discussed later. In formulas,

$$\rho_k^i(q, \omega) = \rho_{k,\text{el}}^i(q, \omega) + \rho_{k,\text{ph}}^i(q, \omega). \quad (11)$$

3. Single-layer response function

We here consider the basic building block of our methodology, i.e., the response of each single layer to potential perturbations. As shown in Ref. [60], the out-of-plane dependence of the single-layer density-density response function can be written in a separable form, i.e., with functions of only z or z' . Accordingly, in this work we express the

density-density response function for a single layer in the dual basis set as

$$[\chi_{\text{IL}}]_k(q, \omega, z, z') = \sum_i Q_k^i(q, \omega) f_k^i(z) f_k^i(z'), \quad (12)$$

$$Q_k^i(q, \omega) = \int dz dz' \phi_k^i(z) [\chi_{\text{IL}}]_k(q, \omega, z, z') \phi_k^i(z'), \quad (13)$$

where Q_k^0 and Q_k^1 are the amplitudes of the “monopole” and “dipole” response functions [61]. Note that the off-diagonal matrix elements of χ_{IL} [i.e., $f_k^i(z) f_k^j(z')$ with $i \neq j$ terms] are null since for the single layers considered in this work we have in-plane mirror symmetry. To simplify notations, we will now drop the (q, ω) dependence when not essential. The density response for a single layer embedded in an heterostructure reads

$$\rho_k^i = Q_k^i V_{k,\text{eff}}^i, \quad (14)$$

where $V_{k,\text{eff}}^i$ is the effective potential felt by the embedded single layer. It is the sum of the actual external potential and of the tails of the macroscopic Hartree potential induced by all the other layers. $V_{k,\text{eff}}^i$ reduces to just the external potential if the single layer is suspended in vacuum.

4. Interaction between layers

The process of obtaining the multilayer response from the single-layer response functions above is described in Ref. [19]. Only the main steps are summarized here. The objective is to reduce the problem to a finite and limited number of elements, i.e., the layers, interacting with each other via simple interlayer couplings. Those interlayer couplings contain all the information about the out-of-plane structure of the system. The starting point is the Poisson equation for the potential induced by the charge variations

$$V_{\text{ind}}(q, \omega, z) = \frac{2\pi e^2}{q} \int dz' e^{-q|z-z'|} \rho(q, \omega, z'). \quad (15)$$

In the dual basis set introduced in this work, the matrix elements of the Coulomb interaction read

$$v_{kl}^{ij}(q) = \frac{2\pi e^2}{q} F_{kl}^{ij}(q),$$

$$F_{kl}^{ij}(q) = \int f_k^i(z) \int e^{-q|z-z'|} f_l^j(z') dz dz', \quad (16)$$

which essentially describe the potential generated by a unit monopole ($j = 0$) or dipole ($j = 1$) charge-density on layer l and projected on layer k . Equation (15) then becomes

$$V_{k,\text{ind}}^i = \sum_{jl} v_{kl}^{ij} \rho_l^j. \quad (17)$$

Notice that in the above equations the Coulomb potential is assumed to be frequency-independent. This assumption is valid if we restrict to wave vectors much larger than the light cone $q \gg \frac{\omega}{c}$, i.e., if we can disregard relativistic retardation effects. The collective modes discussed in this work, including highly confined plasmon-phonon-polaritons, are far from the light cone. In general though, relativistic retardation effects are important when discussing phonon-polaritons in 3D materials [62], meaning that there will be a critical

threshold for the thickness of any heterostructure after which the approximation of Eq. (16) fails to describe the physics of phonon-polaritons, i.e., their wave vectors get near to the light cone.

5. Multilayer response function

Given the coupling of Eq. (16), one can build a set of linear equations describing the collective response of the layers [19]. As anticipated, each individual layer k is assumed to respond to an effective external potential V_{eff}^i which is the sum of the applied external potential plus the sum of the potentials induced by all other layers through Eq. (17), i.e., to

$$V_{k,\text{eff}}^i = V_{k,\text{ext}}^i + \sum_{l \neq k, j=0,1} v_{kl}^{ij} \rho_l^j. \quad (18)$$

Using Eq. (14), we can write a self-consistent system of equations for ρ_k^i :

$$\rho_k^i = Q_k^i \left[V_{k,\text{ext}}^i + \sum_{l \neq k, j=0,1} v_{kl}^{ij} \rho_l^j \right]. \quad (19)$$

Equation (19) is composed of $2 \times N_l$ equations to solve for ρ_k^i at each q and ω , where $i = 0, 1$ and $k = 0, \dots, N_l$.

Once the system is solved, one can determine the density-density response function of the full heterostructure. In fact, the matrix-form of the multilayer density-density response function of Eq. (1) is

$$\chi_{kl}^{ij}(q, \omega) = \int dz dz' \phi_k^i(z) \chi(q, \omega, z, z') \phi_l^j(z'), \quad (20)$$

and its value can be deduced from

$$\rho_k^i = \sum_{jl} \chi_{kl}^{ij} V_{l,\text{ext}}^j. \quad (21)$$

Mind that the above equation is the matrix form of Eq. (1) written in the dual basis set introduced in Sec. II A 2, and it is different from the single-layer density-density response function of Eq. (12), because it relates the induced density on each layer to the external potential applied to the full heterostructure, rather than to the effective potential felt by each layer.

6. Computation of single-layer response

While the basis set in which potentials are decomposed are simple analytical functions, the profile functions used as a basis set for densities are material dependent and computed in DFPT, as explained in Appendix B. As anticipated, their dependence in q is very mild. Including it for graphene and BN brings less than 1% impact on the observables treated in this work, with respect to taking the $q = 0$ value. We therefore neglect it.

The fundamental building block of the VED method is the single-layer density response function to a potential perturbation. As anticipated, in RPA it is split in purely electronic (clamped-ion) and atomic-mediated contributions (total minus clamped-ion) as

$$Q^i(q, \omega) = Q_{\text{el}}^i(q, \omega) + Q_{\text{ph}}^i(q, \omega), \quad (22)$$

where we have dropped the layer index for simplicity, as we will do for the rest of this section. In this work, we will only consider dynamical contributions from plasmons in metals (doped graphene) and longitudinal polar-optical LO phonons in semiconductors or insulators (BN). They contribute to the monopolar component of the electronic and atomic contributions to the response, respectively. The dipolar atomic contribution is neglected, while the electronic dipolar contribution is evaluated in its static limit. In other words, we assume

$$Q^0(q, \omega) \simeq \begin{cases} Q_{\text{el}}^0(q, \omega = 0) + Q_{\text{ph}}^0(q, \omega) & (\text{semiconductors}), \\ Q_{\text{el}}^0(q, \omega) & (\text{metals}), \end{cases} \quad (23)$$

$$Q^1(q, \omega) \simeq Q_{\text{el}}^1(q, \omega = 0). \quad (24)$$

In the general case, the dipolar atomic contribution stemming from the out-of-plane response of ZO phonons would appear in Eq. (24). Neglecting it is a safe approximation in the main energy range of interest for this work, i.e., around the BN's LO phonons energy. Indeed, $Q^1(q, \omega_{\text{LO}}) = Q_{\text{el}}^1(q, 0) \gg Q_{\text{ph}}^1(q, \omega_{\text{LO}})$, as numerically shown in Appendix B 2. For energies close to the BN's ZO phonon ($\omega_{\text{ZO}} \sim \omega_{\text{LO}}/2$), the approximation does not hold, since the response is dominated by ZO phonons. We choose to neglect ZO phonons in this work. However, one might wonder if the ZO phonon's response could lead to significant alterations of the plasmon response. This is not the case for the doping levels studied in this work, since the ZO coupling to graphene's plasmons is much weaker than for LO, as also noted in Ref. [29]. This weaker coupling can be understood as follows. The electric field generated by graphene's plasmon extend to other layers as $e^{-q|z-z_{\text{Gr}}|}$. Since the plasmon dispersion is at relatively small momenta, this generated potential is fairly flat and its projections on the dipole profile functions of BN layers are small (compared to the monopole ones). The ZO mode being associated with the dipole part of the atomic response Q_{ph}^1 , it will only be weakly coupled to the plasmon. Neglecting the atomic dipolar term in Eq. (24) is therefore justified also for the determination of the plasmon dispersion.

The static ($\omega = 0$) electronic contributions of Eqs. (23) and (24) are parametrized from DFPT calculations, as detailed in Appendix B and Ref. [19], while the dynamical ones are modeled as follows. For graphene, we need $Q_{\text{el}}^0(q, \omega)$. One can include the dynamical contribution from free carriers by using the RPA through the noninteracting (irreducible) polarizability, as

$$Q_{\text{el}}^0(q, \omega) = \frac{\chi_{\text{irr}}(q, \omega)}{1 - v_{\text{Gr,Gr}}^{00} \chi_{\text{irr}}(q, \omega)}, \quad (25)$$

$$\chi_{\text{irr}}(q, \omega) = \frac{2}{(2\pi)^2} \sum_{nm} \int d^2\mathbf{k} \frac{n_{\varepsilon_{n\mathbf{k}}}^{\text{FD}} - n_{\varepsilon_{m\mathbf{k}+\mathbf{q}}}^{\text{FD}}}{\varepsilon_{n\mathbf{k}} - \varepsilon_{m\mathbf{k}+\mathbf{q}} + \hbar\omega + i\hbar\eta_{\text{pl}}} \times | \langle u_{n\mathbf{k}} | u_{m\mathbf{k}+\mathbf{q}} \rangle |^2, \quad (26)$$

where $n_{\varepsilon_{n\mathbf{k}}}^{\text{FD}} = \frac{1}{e^{(\varepsilon_{n\mathbf{k}} - \varepsilon_{\text{F}})/k_{\text{B}}T} + 1}$ is the Fermi-Dirac occupation function for state of momentum \mathbf{k} in band n with energy $\varepsilon_{n\mathbf{k}}$ and Bloch periodic function $u_{n\mathbf{k}}$, ε_{F} being the Fermi energy, k_{B} the Boltzmann constant, and T the temperature. There is a factor 2 for spin degeneracy. The plasmon linewidth η_{pl} is an external

parameter in the model. In the case of graphene considered in this work, we simply compute the above χ_{irr} seminumerically in the Dirac cone model, with a Fermi velocity that includes GW corrections [63]. The wave-function overlap is $|\langle u_{n\mathbf{k}} | u_{m\mathbf{k}+\mathbf{q}} \rangle|^2 = \frac{1+nm\cos\theta}{2}$ with $n, m = \pm 1$ for π, π^* bands and θ the angle between \mathbf{k} and $\mathbf{k} + \mathbf{q}$. Deviations from the Dirac cone model are assumed negligible for the frequencies and doping levels studied in the following. The effect of other band levels beside π and π^* is also neglected because their contribution to metallic screening is very weak [64].

For semiconducting materials with polar phonons, long-range Coulomb interactions induce macroscopic electric fields in the crystal. The microscopic responses to such fields add up in a contribution $Q_{\text{ph}}^0(q, \omega)$ that can be expressed in terms of macroscopic quantities only [60]. We deduce $Q_{\text{ph}}^0(q, \omega)$ from the atomic contribution to the inverse dielectric function

$$[\epsilon_{\text{IL}}^{-1}]^i(q, \omega) = \int dz dz' \phi^i(z) \epsilon_{\text{IL}}^{-1}(q, \omega, z, z') \phi^i(z'). \quad (27)$$

For a single layer of BN, the monopolar contribution may be written as (see Appendix A 2 b)

$$[\epsilon_{\text{IL}}^{-1}]^0(q, \omega) = [\epsilon_{\text{IL,el}}^{-1}]^0(q) \left(1 + \frac{\mathbf{e}_{\text{LO}q} \mathcal{D}^{\text{L}}(q) \mathbf{e}_{\text{LO}q}^*}{(\hbar\omega + i\hbar\eta_{\text{LO}})^2 - \hbar^2\omega_{\text{LO}q}^2} \right), \quad (28)$$

where $\mathbf{e}_{\text{LO}} \mathcal{D}^{\text{L}} \mathbf{e}_{\text{LO}}^*$ is the long-range, in-plane polar contribution to the dynamical matrix projected on the eigenvector of mode LO [65], and

$$[\epsilon_{\text{IL,el}}^{-1}]^0(q) = 1 + v_{\text{BN,BN}}^{00}(q) Q_{\text{el}}^0(q) \quad (29)$$

is the static electronic dielectric function. The expression for $\mathbf{e}_{\text{LO}q} \mathcal{D}^{\text{L}}(q) \mathbf{e}_{\text{LO}q}^*$ where the profile of the atomic polarizations are approximated with the electronic ones is given in Eq. (A26). We found that a simpler yet more accurate approximation (discussed in Appendix A 2 b) is to deduce $\mathbf{e}_{\text{LO}q} \mathcal{D}^{\text{L}}(q) \mathbf{e}_{\text{LO}q}^*$ from the difference of the squared frequencies of the LO phonon with respect to the TO phonon,

$$\mathbf{e}_{\text{LO}q} \mathcal{D}^{\text{L}}(q) \mathbf{e}_{\text{LO}q}^* = \hbar^2\omega_{\text{LO}q}^2 - \hbar^2\omega_{\text{TO}q}^2, \quad (30)$$

where $\omega_{\text{LO}q}$ and $\omega_{\text{TO}q}$ are computed via direct DFPT calculations. In particular, for BN the single-layer LO mode has a q -dependent DFPT frequency increasing from $\omega_{\text{TO}} = 1348 \text{ cm}^{-1}$ to the bulk limit of ω_{LO} around 1590 cm^{-1} . The phonon linewidth η_{LO} is an external parameter for our model, that we take as a constant ($\sim 1 \text{ meV}$). We finally get

$$[\epsilon_{\text{IL}}^{-1}]^0(q, \omega) = 1 + v_{\text{BN,BN}}^{00}(q) [Q_{\text{el}}^0(q) + Q_{\text{ph}}^0(q, \omega)], \quad (31)$$

with

$$Q_{\text{ph}}^0(q, \omega) = \frac{\hbar^2\omega_{\text{LO}q}^2 - \hbar^2\omega_{\text{TO}q}^2}{(\hbar\omega + i\hbar\eta_{\text{LO}})^2 - \hbar^2\omega_{\text{LO}q}^2} \times [\epsilon_{\text{IL,el}}^{-1}]^0(q) \frac{1}{v_{\text{BN,BN}}^{00}(q)}. \quad (32)$$

The above expression contains all in-plane multipolar orders of the charge density expansions, going beyond the leading order from Born effective charges at $q \rightarrow 0$, an improvement with respect to Ref. [29]. Notice that Eq. (32), as well as

Eq. (25), contain the Coulomb kernel in the profile basis function, instead of its $q \rightarrow 0$ form $2\pi e^2/q$ used in Ref. [29]. While asymptotically equivalent at $q \rightarrow 0$, this has significant quantitative impacts on the atomic response, phonon dispersions and electron-phonon couplings as q increases, as shown in Fig. 19.

As a final comment, we remind that the disregard of dynamical effects in Eq. (24) means that we cannot study the out-of-plane plasmons of the heterostructures, which we leave for future studies.

B. Measurable quantities

1. Density-density response

The density-density response function of the heterostructure χ defined in the previous section can be used to evaluate several fundamental response functions. For example, in the transmission setup of EELS, one is interested in the scattering of an electron-beam with all the possible excitations of the system. An electron in the beam of energy $E_i = \hbar^2 q_i^2 / 2m_e$ (with a typical order of magnitude of $\sim 10 \text{ keV}$) is scattered by the material, that absorbs a quantity of energy ω through the excitation of internal degrees of freedom. The Stokes EELS cross-section is then proportional to [66,67]

$$\frac{d^2\sigma}{d\Omega d\omega}(q, \omega) \propto \frac{-1}{(q^2 + q_z^2)^2} [1 + n_{\omega}^{\text{BE}}] \text{Im} \times \left[\int dz dz' e^{iq_z(z-z')} \chi(q, z, z', \omega) \right], \quad (33)$$

where $q_z = q_z(q, \omega) = q_i - \sqrt{q_i^2 - q^2 - 2m_e\omega/\hbar}$, m_e is the electron mass, and $n_{\omega}^{\text{BE}} = \frac{1}{e^{\omega/k_{\text{B}}T} - 1}$ is the Bose-Einstein statistical distribution. The q -dependent prefactors of Eq. (33) are not important to the aims of this work, and we will drop them in the following. We will also drop n_{ω}^{BE} , since it can be easily reinserted a posteriori in the evaluation of the cross-section. Then, in the approximation where q_z is negligible—as in typical EELS experiments on heterostructures that are not too thick—the cross section is proportional to

$$\frac{d^2\sigma}{d\Omega d\omega}(q, \omega) \propto -\text{Im}[\chi_{\text{M}}(q, \omega)], \quad (34)$$

$$\chi_{\text{M}}(q, \omega) = \int dz dz' \chi(q, \omega, z, z'). \quad (35)$$

“M” stands for “macroscopic,” since χ_{M} is the in-plane average of the full heterostructure’s density-density response integrated along the out-of-plane coordinates. Equation (35) is rewritten, in our formalism, as

$$\chi_{\text{M}}(q, \omega) = \sum_{kl} \chi_{kl}^{00}(q, \omega), \quad (36)$$

i.e., as the response to an external potential perturbation of the form $V_{\text{ext}}(q, \omega, z) = \sum_k \phi_k^0(z)$. Consistently with the neglect of q -dependent prefactors, in this work we will always normalize χ -related quantities at each q to their maximum, unless otherwise stated. In doing so, the plots of $-\text{Im}\chi_{\text{M}}$ or EELS scattering cross-sections become equivalent [68].

The peaks of $-\text{Im}\chi_{\text{M}}$ in the (q, ω) plane determine the collective modes of the system that are symmetrical with respect

to the out-of-plane center of the heterostructure. The anti-symmetric modes instead average to zero when integrated in the out-of-plane direction, and are therefore dark in an EELS experiment. The antisymmetric modes are though visible in the total spectral function of the density-density response, defined as

$$\chi_{\text{Tr}}(q, \omega) = \sum_{ik} \chi_{kk}^{ii}(q, \omega). \quad (37)$$

Minus the imaginary part of Eq. (37), in fact, contains all the collective excitations of the system, and it is well defined even where modes cross.

More complex response functions can be defined from the χ matrix, in particular for perturbations that are non uniform over the layers or containing finite projections on the dipole response. As an example, one could consider evanescent waves as a way to reveal plasmons of graphene on a substrate [9,10]. We here propose a simple modelization for such kind of measurement. We assume that we have a tip that can both induce exponentially suppressed potentials in the heterostructure and measure averages of the induced potential on a given surface layer S . In our formalism, the form of the evanescent (“ev”) external potential has components

$$V_{k,\text{ev}}^i(q, \omega) = \int dz f_k^i(z) e^{-q|z-z_S|}, \quad (38)$$

where z_S is the central coordinate of the surface layer. Using Eq. (17), the average of the potential on the surface layer, i.e., its monopolar component, is proportional to

$$V_{S,\text{ind}}^0 = \sum_{ik} v_{S_k}^{0i}(q) \rho_k^i(q, \omega) = \sum_{ijkl} v_{S_k}^{0i} \chi_{kl}^{ij}(q, \omega) V_{l,\text{ev}}^j(q, \omega). \quad (39)$$

From this induced potential we can define a ‘local’ density-density response via the Coulomb kernel

$$\chi_{\text{loc}}(q, \omega) = V_{S,\text{ind}}^0(q, \omega) / v_{SS}^{00}(q). \quad (40)$$

More realistic and complicate descriptions are possible, but they go beyond the scope of this work. We end this section reminding that from χ one can also derive the sheet optical conductivity, to define figures of merit such as the propagation quality factor, i.e., the distance (in number of wavelength) traveled before decay, and reflectivity [16,20].

2. Scattering rates

The electrons of the heterostructure experience scattering from collective modes. Understanding and quantifying those processes is essential to characterise the relaxation of the electron energy and momentum. In the single-layer case, the squared modulus of the electron-phonon and/or electron-plasmon couplings describing this scattering are obtained [23,69] via the product of the imaginary part of the inverse total dielectric function, containing electronic and atomic contributions, and the Coulomb kernel, as shown in Appendix A.3. For the multilayer, if we only assume that the matrix elements of $(z - z_k)$ between Bloch states is small for every k , then the scattering rate for an electron in the Bloch

state $n\mathbf{k}$ reads (Appendix A.3)

$$\begin{aligned} \tau_{n\mathbf{k}}^{-1} &= \frac{2\pi}{\hbar} \frac{1}{N_{\mathbf{q}}} \sum_{\mathbf{q}} \int_{-\infty}^{\infty} d\omega \mathcal{A}(\omega) \delta(\hbar\omega + \varepsilon_{m\mathbf{k}+\mathbf{q}} - \varepsilon_{n\mathbf{k}}) \\ &\quad \times \sum_{kl} \langle u_{n\mathbf{k}} | \phi_k^0 | u_{m\mathbf{k}+\mathbf{q}} \rangle \langle u_{m\mathbf{k}+\mathbf{q}} | \phi_l^0 | u_{n\mathbf{k}} \rangle g_{kl}^2(q, \omega), \\ \mathcal{A}(\omega) &= \left[n_{\omega}^{\text{BE}} + \frac{1}{2} + \text{sign}(\omega) \frac{1}{2} - \text{sign}(\omega) n_{\varepsilon_{m\mathbf{k}+\mathbf{q}}}^{\text{FD}} \right], \end{aligned} \quad (41)$$

where $N_{\mathbf{q}}$ is the number of points in the \mathbf{q} -grid, while g_{kl}^2 is

$$g_{kl}^2(q, \omega) = \text{sign}(\omega) \sum_{ijk'l'} \frac{-1}{A\pi} \text{Im} \left[v_{kk'}^{0i}(q) \chi_{k'l'}^{ij}(q, \omega) v_{l'l}^{j0}(q) \right]. \quad (42)$$

A is the area of the unit cell of the single layer, taken equal for all the layers in this work for simplicity. Notice that the $\text{sign}(\omega)$ term is included in the definition of g^2 so that it does not become negative with $\omega \rightarrow -\omega$, due to the property Eq. (A2). Scattering times are therefore always positive definite. Classically, the coupling g_{kl}^2 is the imaginary part of the potential projected on layer k when layer l is perturbed with a normalized charge density perturbation, as sketched in the bottom panel of Fig. 2.

The interaction of electrons of the heterostructure with phonons, plasmons, and any hybrid collective modes is entirely contained in the response of the system. In practice, it is mediated via every kind of collective modes contained inside χ . Only in certain limits, i.e., away from plasmon-phonon hybridization, can the above coupling be formally identified with electron-phonon or electron-plasmon couplings, see discussion in Appendix A.3.

Note also that g_{kl}^2 is the interaction stripped of the Bloch functions overlaps, while the scattering rate expression includes the overlaps. For BN, Bloch overlaps can be approximated to unity or zero at small q . For graphene, this would be notably wrong. Indeed, the wave-function overlap strongly depends on the angle between the momenta of the two electrons. We will nonetheless still study the coupling g_{kl}^2 in the following, and use Eq. (41) with the overlap given under Eq. (26) while studying the impact of remote coupling on graphene’s electron scattering rates.

III. COLLECTIVE MODES

In this section, the VED formalism is used to obtain the electrodynamic excitations of graphene and BN, and their interplay within in the heterostructure. The more general term “collective mode” is also used, with the understanding that in the current context, they are the one driven by long-range electromagnetic interactions. The treatment of the coupling between electrons and collective modes is treated in Sec. IV.

A. Graphene’s plasmons and BN’s phonons before coupling

In this section, the collective modes of multilayer BN and graphene are considered separately, before any coupling between the two, as shown in Fig. 3. We show that the present model reproduces the features of multilayer BN and doped graphene, at the cost of a simple DFPT calculation for a single

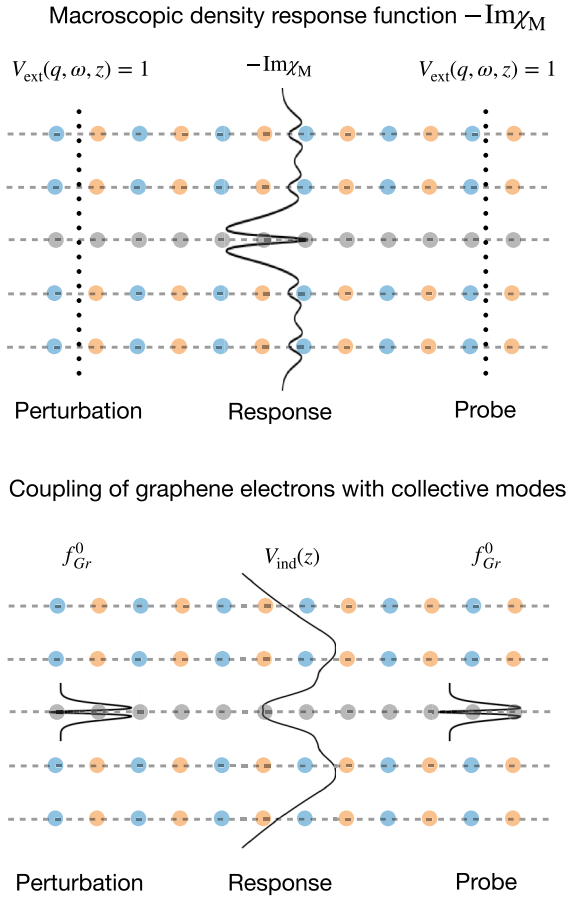


FIG. 2. Sketch of the computation of the macroscopic χ_M and of the coupling between electrons and collective modes in the VED framework. On the top, only the monopole part of the density-density response χ_M is used, since the projection of the dipole part on the probe vanishes. On the bottom, the induced potential response is plotted, which drives the coupling of electrons. The plotted curves are computed with the VED method in 2BN/Gr/2BN for relatively large momentum at $\omega \sim \omega_{LO}$.

layer of each material. Before coupling, those systems are fairly well-known, such that the VED method can be compared to literature and direct DFPT calculations. At the same time, it brings new insight on certain aspects like the relative intensity of the different modes in the EELS intensity.

1. Graphene's plasmons

Graphene is a very promising medium for plasmonics [70,71], due to the strength and tunability of the plasmons. Analytical models [72–74] of their dispersion are obtained by considering the polarizability of doped graphene—Eq. (17) of Ref. [72]—and the RPA relation to obtain the plasmon dispersion. The dielectric environment may be taken into account by a phenomenological background dielectric constant κ . In the small momentum limit, the plasmon dispersion is found to be

$$\hbar\omega_{pl}(q) \underset{q \rightarrow 0}{\sim} \sqrt{\frac{2e^2\varepsilon_F}{\kappa}} \sqrt{q}. \quad (43)$$

Two important features of the plasmon dispersion are shown here: the \sqrt{q} asymptotic behavior, and a dispersion that

scales with the Fermi surface, since $\hbar\omega_{pl}/\varepsilon_F \propto \sqrt{q/k_F}$, with a proportionality constant that depends only on the dielectric environment.

The left panel of Fig. 3 shows $-\text{Im}[\chi_M(q, \omega)]$ for isolated graphene with a Fermi level of $\varepsilon_F = 0.2$ eV and at room temperature. The only chosen parameter is the plasmon linewidth, fixed at $\eta_{pl} = 5$ meV, consistent in order of magnitude with theoretical [75,76] and experimental [11,13] investigations. The maxima of $-\text{Im}[\chi_M(q, \omega)]$ agree well with the asymptotic expression Eq. (43), as represented by the blue continuous line for $\kappa = 1$, at least up to $q/k_F \sim 0.2$. The same results (in units of $\hbar\omega/\varepsilon_F$ and q/k_F) are obtained for different Fermi levels. The main features of the dispersion are thus recovered. Other spectral properties are also consistent with the literature. Notably, the spectral weight scales with ε_F [72].

In the left panel of Fig. 3, different zones are delineated with dashed lines, corresponding to the boundaries of the intra- and interband particle-hole continua. In practice, energy and momentum conservation allow intra- and interband electronic transitions only in zones III and II, respectively. Note that those boundaries are only strict at zero temperature. Otherwise they are smeared by the Fermi-Dirac occupation function.

2. BN's polar-optical phonons

Multilayer BN is ubiquitous in 2D devices [77]. It is often used as an encapsulator, to protect the active layer from the environment and thus get closer to ideal intrinsic properties. By itself, it is a very promising platform for various photonics applications [78]. In particular, BN's phonon-polaritons [15,20,79,80] have attracted a lot of interest based on their ability to shape and control light in matter. In 2D, phonon-polaritons are simply the polar-optical phonons of the system [8], and near-field microscopy techniques developed to probe polaritons in 2D materials are one of the best ways to probe BN's phonon dispersions, e.g., versus number of layers [20,79]. In addition to a detailed microscopic understanding, the VED model provides valuable insights to interpret and predict the results of such experiments. In particular, it clarifies which modes are active and their relative intensities.

The middle panel of Fig. 3 shows the total spectral function $-\text{ImTr}\chi$ for five-layer BN (5-BN). This is computed in the VED model, using inputs from single-layer BN DFPT calculations. The only input parameter is the BN's phonon linewidth $\eta_{LO} = 0.6$ meV, chosen fairly small here to obtain separate peaks. Only phonon excitations are present, and the red crosses indicate phonon frequencies computed directly in DFPT. We observe a fairly good agreement. The error likely comes from modeling approximations, as discussed in Appendix B; also, in DFPT calculation each BN single layer does not possess anymore mirror symmetry as instead it is enforced in our vdWH.

Many interesting characteristics of polar phonons in 2D materials are recovered. The highest branch displays the dimensionality signature of the LO-TO splitting [81–83], i.e., the nonanalytic and vanishing splitting at $q \rightarrow 0$, marked by the linear increase of the dispersion at small but finite momentum. The total number of LO modes is equal to the number of layers. The highest mode corresponds to in-phase

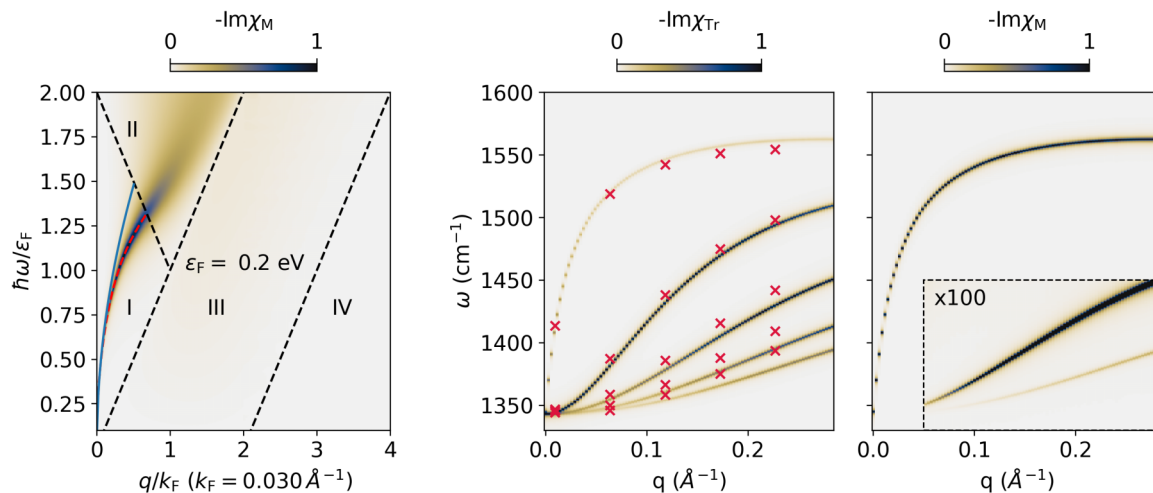


FIG. 3. (Left) Graphene's plasmonic excitation compared to the analytical model of Eq. (43) with $\kappa = 1$ (blue curve). The colormap represents $-\text{Im}\chi_M$, normalized by the global maximum of the intensity. The dashed red curve is the extrapolated maximum of $-\text{Im}\chi_M$. The black dashed lines separate the following zones. I: no electron-hole transition and undamped/dispersed plasmon, II: interband electron-hole continuum, III: intraband electron-hole continuum, IV: no electron-hole transition. (Middle) Polar LO phonon modes of 5-BN from the resonances of the full spectral function $-\text{Im}\chi_{Tr}$, normalized at each momentum. The relative signs of the layer components of the phonon polarizations (corresponding to the sign of $\text{Im}\rho_k^M$, defined in the text) are as follows, from highest to lowest energy mode: $(++++)$, $(--0++)$, $(-++++)$, $(+ - 0 + -)$, $(+ - + - +)$. Red crosses are phonon frequencies computed in DFPT. (Right) $\text{Im}\chi_M$ of 5-BN, normalized at each momentum. The highest LO mode is by far the most intense. Increasing the signal by a factor 100 in the inset reveals that two other modes are active, although much weaker.

contributions from all the layers, while the lower energy modes corresponds to various out-of-phase combinations. The slopes of the latter vanish at $q \rightarrow 0$.

The right panel of Fig. 3 shows $-\text{Im}\chi_M$ for five-layer BN (5-BN). As already mentioned, among all the LO modes, only the symmetric ones appear in $-\text{Im}\chi_M$. Indeed, the perturbation and probe are symmetric in z , implying that the antisymmetric modes are inactive. The symmetry of the modes is obtained via the relative sign of the imaginary part of the density response $\rho_k^M = \sum_l \chi_{kl}^{00}$ to a uniform external perturbation at the different resonances, and it is indicated in the caption of Fig. 3. The relative amplitude of the layers' density response decreases from the center to the outside of the stack, consistent with the relative amplitude of phonon displacement obtained in DFPT. The VED framework provides solid grounds to explain or predict the relative intensity of the modes in, e.g., EELS experiments. In the case of uniform perturbation and probe, note that the intensity of the peaks decreases with energy, and the highest one dominates largely.

B. Interplay of plasmons and phonons

Beyond the interest of graphene and BN taken individually, it is essential to investigate their interactions. Since BN is often used as an encapsulator to protect graphene and other 2D materials, it is important to understand exactly how it can interact and modify the intrinsic properties of the encapsulated layer. The coupling between the two can also be exploited to tailor the polaritons [12,55], thus opening new pathways for electromagnetic waves manipulation; or to better control the energy and momentum relaxation of graphene's electrons [17]. For BN-capped graphene, the main tuning parameters are the Fermi level of graphene and the number of BN layers.

We study the interplay of graphene's plasmons and BN's LO phonons by focusing on two aspects: their dispersion, discussed here, and their scattering of graphene's electrons, discussed in Sec. IV. On top of previous analytical works on plasmon-phonon interactions [23,26,27,76], we bring the quantitative and predictive insight of microscopic *ab initio* simulations.

Figure 4 shows $-\text{Im}\chi_M$ for the prototypical system made of graphene with a Fermi level of $\varepsilon_F = 0.2$ eV encapsulated by 10-BN on each side. The plasmon and phonon linewidths are set to $\eta_{pl} = 5$ meV, $\eta_{LO} = 1$ meV

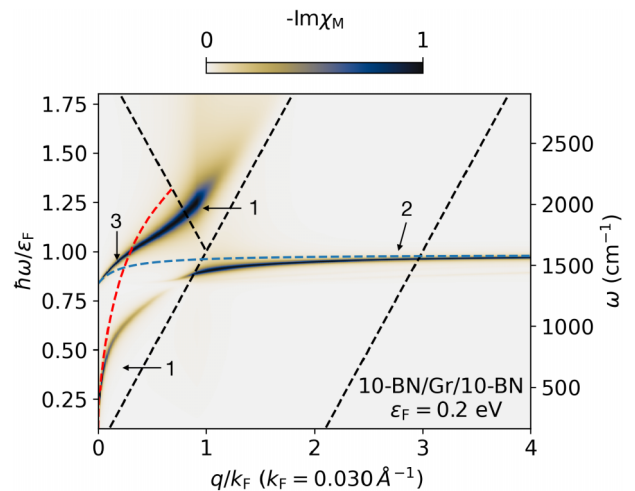


FIG. 4. (Top) Macroscopic $-\text{Im}\chi_M$ for 10-BN/Gr@0.2eV/10-BN, normalized at each momentum. Blue and red dashed lines are the uncoupled excitations: highest LO dispersion of 20 BN layers and plasmon of free-standing graphene, respectively.

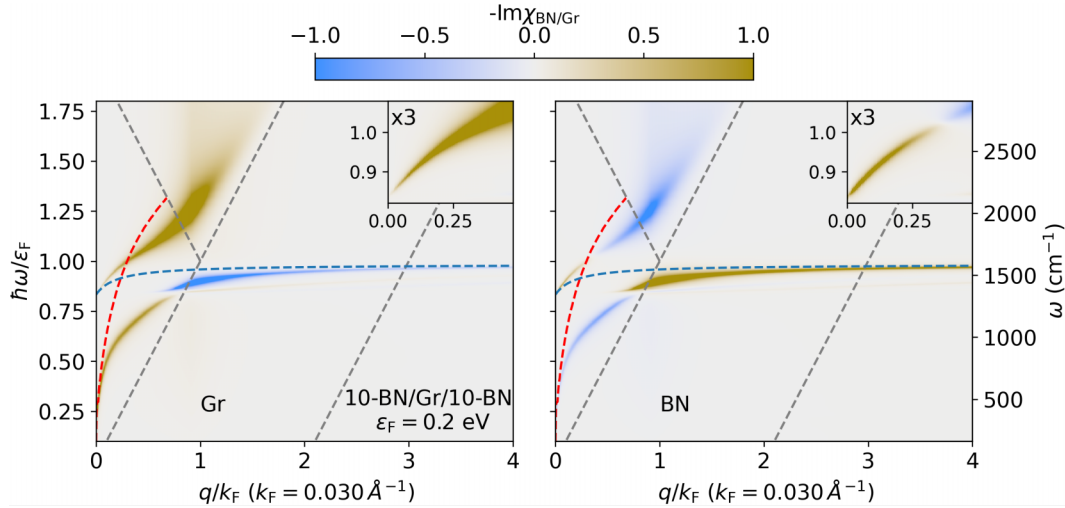


FIG. 5. 10BN/Gr@0.2eV/10BN. Contributions to $-\text{Im}\chi_M$ from graphene and BN, $-\text{Im}\chi_{\text{Gr}}$ and $-\text{Im}\chi_{\text{BN}}$ as described by Eq. (45), normalized at each q point. The inset focuses on the hybrid plasmon-phonon excitation at small q and around $\hbar\omega_{\text{LO}}$, with the intensity magnified by a factor of 3 for better visualization. Blue and red dashed lines are the uncoupled excitations: LO dispersion of 20 BN layers and isolated graphene's plasmon, respectively.

(for numerical efficiency and plotting purposes, within experimental order of magnitude). We clearly observe an anticrossing that indicates the plasmon-LO phonon coupling. Let us already name (q, ω) regions of interest outside of the anticrossing, as annotated in Fig. 4: (1) the plasmon region covers the plasmon dispersion away from the typical LO phonon frequency, $\omega \neq \omega_{\text{LO}}$; (2) the phonon region follows the phonon dispersion at large momenta, to the right of the plasmon dispersion $q/k_F > \hbar\omega_{\text{LO}}/\varepsilon_F$; (3) the plasmon-phonon hybrid region covers the small momenta $q \rightarrow 0$ around the LO phonon frequency $\omega \sim \omega_{\text{LO}}$.

In the plasmon region (1), the plasmon is screened by the presence of BN, pushing its dispersion toward the $\hbar\omega/\varepsilon_F = q/k_F$ dashed line, as expected from external screening in Eq. (43). Along their dispersion, the LO phonons experience different screening regimes from graphene. In the phonon region (2), they experience metallic screening, suppressing the LO-TO splitting and pushing the dispersion downward. Indeed, in the presence of static metallic screening, the slope of the highest mode dispersion at small momenta would vanish. Here, however, in the polariton region (3) the free-carrier screening from graphene is inefficient and we recover the finite slope one would obtain in BN alone for $q \rightarrow 0$ and $\omega \sim \omega_{\text{LO}}$, and a stiffening of the slope at small but finite momenta.

Those results are developed in the following. First, the nature of the excitations is carefully studied, to disentangle, when possible, phonons and plasmons. Second, we consider the case of a surface probing setup to access other collective modes. Third, the effect of the number of BN layers is analysed looking at 1, 10, and 30 BN layers on each side. Finally, the effect of graphene's Fermi level is considered, with two other representative doping: $\varepsilon_F = 0.1$ and 0.3 eV.

1. Nature of the excitations and layer contributions

Here, we look at the layers from which the response originates to unravel the nature of the excitations. This procedure

provides valuable insights into the interplay of phonons and plasmons, showing which mode drives the excitation, and how electrons screen it.

In Fig. 5, a unit potential perturbation is applied to all layers and the response coming from either graphene or BN are separated as follows:

$$\chi_M = \chi_{\text{BN}} + \chi_{\text{Gr}}, \quad (44)$$

$$\chi_{\text{BN}} = \sum_{k=\text{BN},l} \chi_{kl}^{00}, \quad \chi_{\text{Gr}} = \sum_{k=\text{Gr},l} \chi_{kl}^{00}. \quad (45)$$

Notice that the sum over BN runs over all the BN layers. Figure 5 shows $-\text{Im}\chi_{\text{BN}}$ and $-\text{Im}\chi_{\text{Gr}}$. It clearly reveals three types of excitations, clarifying the nomenclature of the three regions of (q, ω) space defined in the previous section. First, in the phonon region (2), we observe a positive contribution from BN layers and a negative one from graphene. Note that the sum of the two is always positive, so that here $|-\text{Im}\chi_{\text{BN}}| > |-\text{Im}\chi_{\text{Gr}}|$. Therefore, the excitation is driven by BN's polar phonons, and graphene is simply responding with (static) free-carrier screening. Second, in the plasmon region (1), we observe instead a positive contribution from graphene, and a negative one from BN layers. Thus, the plasmon is driving the excitation, and BN's electrons respond by screening it. Third, in the plasmon-phonon hybrid region (3) we observe positive contributions from both graphene and BN. This is a true hybrid polariton, driven by both plasmonic and phononic responses. The insets zoom in on this plasmon-phonon hybrid. The dispersions of the modes before the coupling are also plotted, i.e., graphene's plasmon without BN and the highest LO phonon mode corresponding to the total number of BN layers in absence of graphene. The slope of the hybrid excitation dispersion (i.e., the group velocity of the polariton) approaches that of the isolated 20-BN system when $q \rightarrow 0$. In that limit, the polariton gradually becomes pure LO phonon, and contextually $-\text{Im}\chi_{\text{Gr}}$ vanishes. At small but finite q , however, the slope remains fairly high, rather than flattening

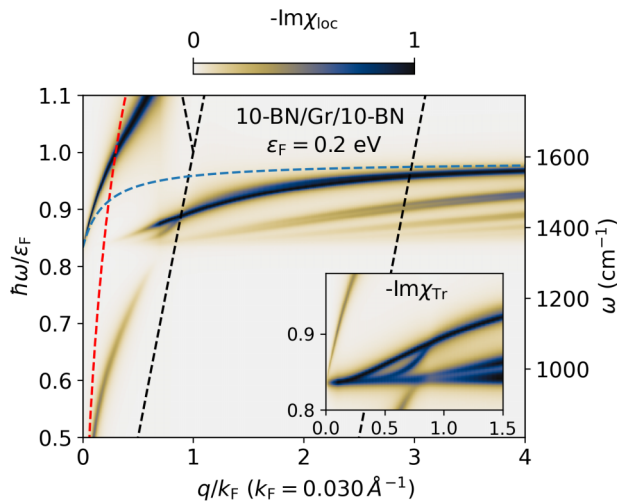


FIG. 6. $-\text{Im}\chi_{\text{loc}}$ normalized at each q in 10-BN/Gr@0.2eV/10-BN, representing the results of a probe measurement at the surface, with the model explained in Sec. II B 1. The inset zooms in on the anticrossing region, and shows the spectral function $-\text{Im}\chi_{\text{Tr}}$.

like that of the intrinsic BN's phonons. This is thanks to a gradual shift of the plasmon-phonon hybrid from phonon to plasmon, as $-\text{Im}\chi_{\text{BN}}$ decreases with increasing q (eventually changing sign) while $-\text{Im}\chi_{\text{Gr}}$ increases. Eventually, following this branch, we fall back on the plasmon-driven excitation. We thus have a clear interpretation of all the excitations and the role played by the electrons, phonons, and plasmons.

2. Probing other modes

The macroscopic response function χ_{M} only probes symmetric modes because perturbation and probe are uniform over the layers. This is not the case of surface spectroscopic techniques, like scattering-type scanning near-field optical microscopy [20] (sSNOM) or 2D High-resolution electron energy loss spectroscopy [84] (2D HREELS). A quantitatively accurate simulation of those experimental setups is out of scope here. However, it is informative to consider a setup where perturbation and probe are localised on the surface, and qualitatively assess the consequences on the activity and relative intensity of the collective modes. Using the model explained in Sec. II B 1, we expect the physical observables to be proportional to $\chi_{\text{loc}}(q, \omega)$, plotted in Fig. 6.

The relative intensities of the modes is very different with respect to the plots of $-\text{Im}\chi_{\text{M}}$, with the out-of-phase LO modes more visible. Interestingly, the most intense phonon-like mode is not the highest LO mode, but the mode corresponding to the BN layers moving in-phase with respect to layers on the same side of the graphene layer, but out-of-phase with respect to the BN layers on the other side of graphene. This mode is unaffected by screening from graphene, since any electric field from phonons on one side of graphene would be equal and opposite to the field from the other side. Thus, the net potential from phonons felt by graphene vanishes, and it does not respond. This mode actually crosses the dispersion of the in-phase LO mode, becoming higher in energy when the latter is strongly screened by graphene. This raises the question of which mode is

actually most seen in surface-probing experiments. Near-field spectroscopy would probe the vicinity of the light cone, dominated by the plasmon-phonon hybrid at vanishing momentum. Techniques probing larger momenta like 2D HREELS [84], however, might very well be dominated by this antisymmetric mode.

3. Effects of number of BN layers

The number of BN layers may vary significantly in different realisation of similar devices. Whether it is a parameter one can control precisely to tailor the properties of the system, or a fluctuating number depending on the experimental realization of the sample, it is important to understand its impact on the collective modes of BN-capped systems. Beyond the fairly obvious increase of the plasmon-phonon coupling, the VED framework enables the quantification and a detailed interpretation of the changes in the collective modes dispersions.

Figure 7 shows $-\text{Im}\chi_{\text{M}}$ for graphene at $\varepsilon_{\text{F}} = 0.2$ eV encapsulated by 1 or 30 layers of BN on each side, on the top and bottom panels, respectively. This complements the dispersion of Fig. 4, with 10-BN on each side. As the number of BN layers increases, the features already noted in the previous sections are enhanced. Due to overall stronger phonon responses, the plasmon-phonon coupling and the size of the anticrossing increase. Also, the stronger electronic screening from BN pushes the plasmonic dispersion closer to the $\hbar\omega/\varepsilon_{\text{F}} = q/k_{\text{F}}$ line. The slope of the polariton at $q \rightarrow 0$ and $\omega \sim \omega_{\text{LO}}$ increases, following that of the intrinsic LO phonon, as the polar contributions from all the layers add up [83].

We remind that, as discussed after Eq. (16), our framework can be applied until the slope of the longitudinal phonon is not so steep to enter in the light-cone region, an event that happens for a certain limiting width of the layer (way beyond what is considered here). Increasing the width further causes relativistic retardation effects to become important and we therefore enter the realm of three-dimensional phonon-polaritonics. Notice that this gives a rigorous criteria to distinguish between a slab and a proper three-dimensional materials from the polaritonics point of view.

4. Effects of graphene's Fermi level

Graphene's Fermi level is often tuned electrostatically [85–87]. Within a field-effect transistor geometry, free carriers are accumulated in graphene, typically up to the order of 10^{13} cm $^{-2}$. This corresponds to Fermi levels of a few hundreds of meV. Thus, in the following, three Fermi levels $\varepsilon_{\text{F}} = 0.1, 0.2, 0.3$ eV are considered and the consequences on the collective modes of the BN-encapsulated graphene are studied. Since the effect of doping on the plasmon are relatively well-known, we focus on the rich and yet unresolved discussion around the dynamical screening of phonons and their coupling to electrons.

Figure 8 shows $-\text{Im}\chi_{\text{M}}$ for graphene encapsulated by 10 BN, at Fermi levels $\varepsilon_{\text{F}} = 0.1$ eV and $\varepsilon_{\text{F}} = 0.3$ eV, in addition to the $\varepsilon_{\text{F}} = 0.2$ eV case from Fig. 4. In all cases, some trends persist. The plasmon-phonon hybrid follows the intrinsic LO phonon dispersion in the $q \rightarrow 0$ limit, while the LO-TO splitting is reduced due to free-carrier screening

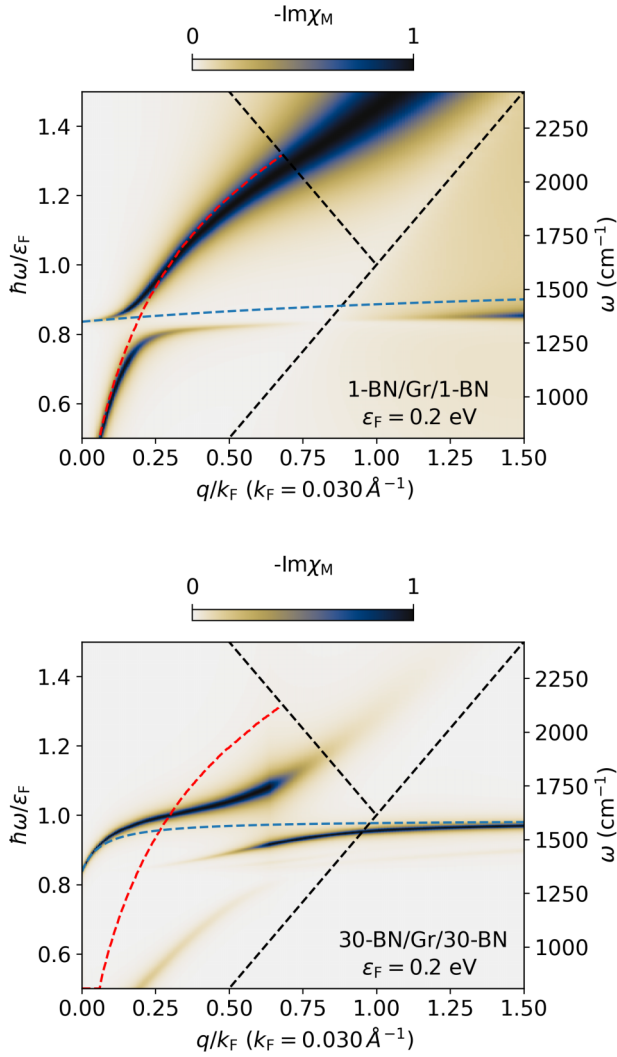


FIG. 7. $-\text{Im}\chi_M$ for 1-BN/Gr@0.2eV/1-BN (top) and 30BN/Gr@0.2/30BN (bottom) normalized at each q . The blue curve and dashed red line are the uncoupled modes (LO dispersion of total number of BN layers in blue, isolated graphene's plasmon in red).

from graphene in the intraband electron-hole continuum, that is for $q > \frac{\hbar\omega_{LO}}{\varepsilon_F} k_F = \frac{\omega_{LO}}{v_F}$. The behavior between those two regimes ($q \rightarrow 0$ and $q > \frac{\omega}{v_F}$), however, is quite sensitive to the Fermi level. In the case of $\varepsilon_F = 0.2$ eV, where phonon energy and Fermi level are similar, the plasmon-phonon anticrossing happens around the middle of the triangular region I. For $\varepsilon_F = 0.3$ eV, this is shifted towards smaller momenta, and so is the region where we can observe the intrinsic LO phonon dispersion. Indeed, assuming the plasmon dispersion to be of the form of Eq. (43), the momentum q where the plasmon and phonon cross is proportional to k_F . For both $\varepsilon_F = 0.2$ eV and $\varepsilon_F = 0.3$ eV, we observe the intrinsic and screened LO dispersion on the left and right of the anticrossing, respectively. The qualitative behavior starts to change significantly when $\hbar\omega_{LO} > \varepsilon_F$, and the crossing of plasmon and phonon dispersions fall into the interband electron-hole continuum. There is no clear anticrossing then. Instead, a collective

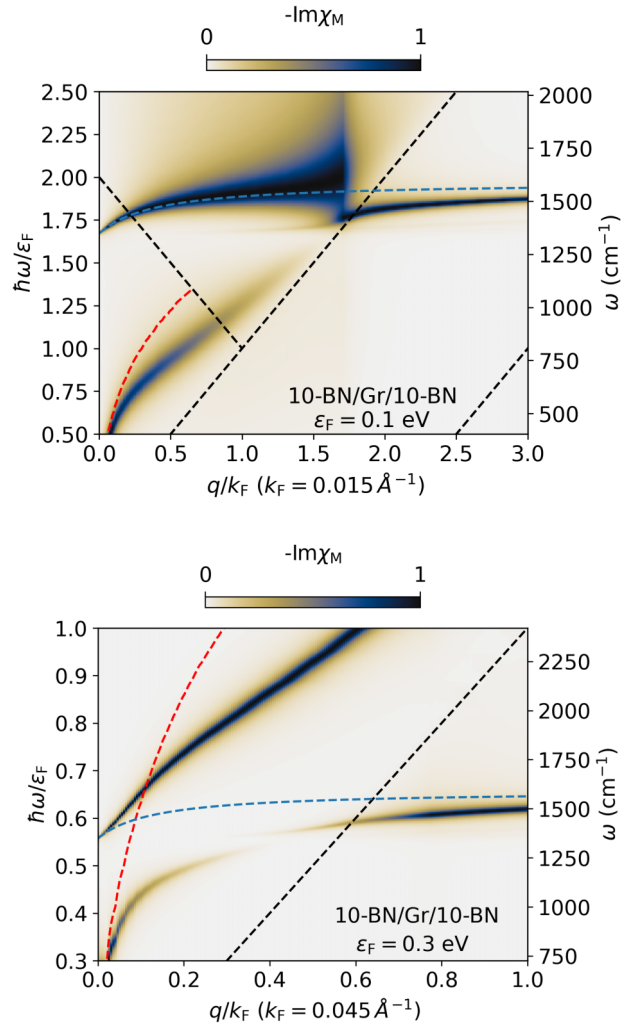


FIG. 8. $-\text{Im}\chi_M$ for 10-BN/Gr@0.1eV/10-BN (top) and 10-BN/Gr@0.3eV/10-BN (bottom), normalized at each q , in the plotted ω window. See also Fig. 4 for the case of $\varepsilon_F = 0.2$ eV. Dashed black lines indicate intra- and interband electron-holes continuum. The dashed red line corresponds to the plasmon dispersion in isolated graphene. The blue line indicates the phonon dispersion of the highest LO mode in 20-BN without graphene.

mode emerges that roughly follows the intrinsic LO phonon dispersion. A clear free carrier screening only starts in the intraband continuum. Qualitatively, the difference between interband and intraband comes from the possibility in the latter case to have Lindhard/Thomas-Fermi type of screening [62,88], ultimately coming down to the non vanishing Bloch overlaps in the $q \rightarrow 0$ limit [65].

IV. ELECTRON SCATTERING

The VED model provides the coupling between electrons and the various collective modes, to be included in the calculations of scattering times. Above, the study of quantities like χ_M or χ_{Tr} informed us about the dispersion and nature of the modes. In this section we investigate how those modes may scatter the electrons of the heterostructure.

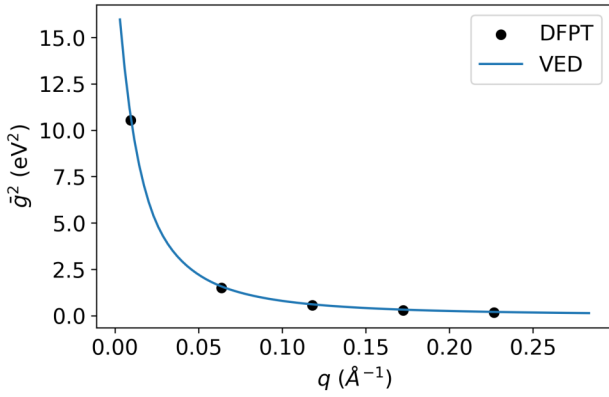


FIG. 9. Total coupling, for a 5-BN heterostructure, compared to DFPT calculations performed as described in Appendix D. The coupling is entirely due to the interaction between electrons and phonons, statically screened by the BN's dielectric function.

A. Validation in multilayer BN

We first validate the method by comparing the VED results on multilayer BN to the DFPT ones, obtained as described in Appendix D. Indeed, since multilayer BN is a large gap semiconductor, all electronic contributions to the response are treated in the static limit within the VED model in that case. This corresponds to the adiabatic Born-Oppenheimer approximation of DFPT, and the results should thus differ only due to the approximations of the VED model (see Appendix B).

Figure 9 shows the electron-phonon coupling with the LO modes in 5-BN. Practically, using Eq. (42) we compute

$$g^2(q, \omega) = \frac{1}{N_l^2} \sum_{kl} g_{kl}^2(q, \omega), \quad (46)$$

which physically is the square of the electron-phonon coupling since other collective modes are absent. We also define

$$\bar{g}^2(q) = \int_0^\infty g^2(q, \omega) d\omega. \quad (47)$$

In the following, the bar sign will be used consistently on all other g^2 quantity to signify integration over ω from zero to infinity. Notice that the sums run on all the BN layers. In fact, in the vdW approximation the Bloch electronic state of the full heterostructure layers are degenerate so that electrons are delocalized over the full structure. The agreement with DFPT is excellent, with the remaining error likely due to aforementioned modeling approximations.

Note that we do not force any phonon perturbation singularly in the VED method. The external perturbation itself excites all the possible phonons modes. Therefore, we get the sum of the couplings with all phonon modes, so we compare with the sum of the (squared) couplings over DFPT modes. Nevertheless, as seen in DFPT and expected in VED, the highest mode largely dominates the coupling. This result also validates the spectral weights of the peaks in the VED method as a function of momentum, which is a significant progress with respect to other *ab initio* works [29].

B. Scattering from coupled plasmon and phonons

We now continue with the prototypical system consisting of graphene sandwiched by n layers of BN on each side. Here we consider the coupling with graphene's electrons, i.e., we compute

$$g_{\text{Gr}}^2(q, \omega) = \sum_{ijk'l'} \frac{-1}{A\pi} \text{Im} [v_{\text{Gr}k'}^{0i}(q) \chi_{k'l'}^{ij}(q, \omega) v_{l'\text{Gr}}^{j0}(q)]. \quad (48)$$

The above equation can be interpreted as using normalized charge densities as perturbation and probes of the system, as sketched in Fig. 2. The coupling of Eq. (48) contains contributions from phonons and plasmons. We plot it in the central column of Fig. 10 in the full (q, ω) plane, normalized at each q , for different n (1, 10, and 30 BN per side) at a doping level of $\varepsilon_F = 0.2\text{eV}$. The left and right panels of Fig. 10 show $g_{\text{Gr}}^2(\omega)$ and its running integral $\int_0^\omega g_{\text{Gr}}^2(\omega') d\omega'$ $q = 1.5k_F$ and $q = 3.8k_F$. In both cases, the number peaks around the phonon energy increases with the number of BN layers. Clearly, graphene's electrons couple to several LO modes with different polarizations. This implies that considering a single surface-optical phonon for the remote coupling between electrons and phonons [58], as routinely done for bulk substrates like SiO_2 [89], is not valid for BN encapsulation and vdWH in general. At $q = 3.8k_F$, up to $\hbar\omega/\varepsilon_F \sim 1.75$, no electron-hole excitation is possible, and the coupling is totally determined by the electron-phonon interaction. For $q = 1.5k_F$, however, $g_{\text{Gr}}^2(\omega)$ contains significant contributions from the low-energy spectrum of the intraband electron-hole continuum for $\hbar\omega/\varepsilon_F < 1$, from the different phononic branches of BN around $\hbar\omega/\varepsilon_F \sim 1$, and finally from the dispersed plasmon dispersion in the interband region for $\hbar\omega/\varepsilon_F > 1.5$.

While it contributes to electronic lifetimes detected, e.g., via ARPES, the scattering of graphene's electrons coming from graphene's own electronic excitations (plasmon and electron-hole excitations) does not necessarily contribute to the momentum relaxation responsible for resistivity (depending on the magnitude and origin of plasmon damping). Indeed, momentum is exchanged with essentially the same entity, i.e., graphene's electrons [26]. Electron-phonon scattering, on the other hand, does. It is then desirable to separate the different couplings arising from the interaction with different collective modes.

1. Separation of the coupling with different modes

In Sec. III B 1 we separated the contributions from graphene and BN to gain insight on the nature of the excitations. Figure 11 shows the results of a similar procedure applied to interaction between electrons and collective mode interactions. We separate the contributions as follows:

$$g_{\text{Gr}}^2 = g_{\text{Gr}}^{2,\text{BN}} + g_{\text{Gr}}^{2,\text{Gr}}, \quad (49)$$

$$g_{\text{Gr}}^{2,\text{BN}}(q, \omega) = \frac{-1}{A\pi} \sum_{k=\text{BN}} \sum_{ijl} v_{\text{Gr},k}^{0,i} \text{Im} [\chi_{kl}^{ij}] v_{l,\text{Gr}}^{j0},$$

$$g_{\text{Gr}}^{2,\text{Gr}}(q, \omega) = \frac{-1}{A\pi} \sum_{k=\text{Gr}} \sum_{ijl} v_{\text{Gr},k}^{0i} \text{Im} [\chi_{kl}^{ij}] v_{l,\text{Gr}}^{j0}. \quad (50)$$

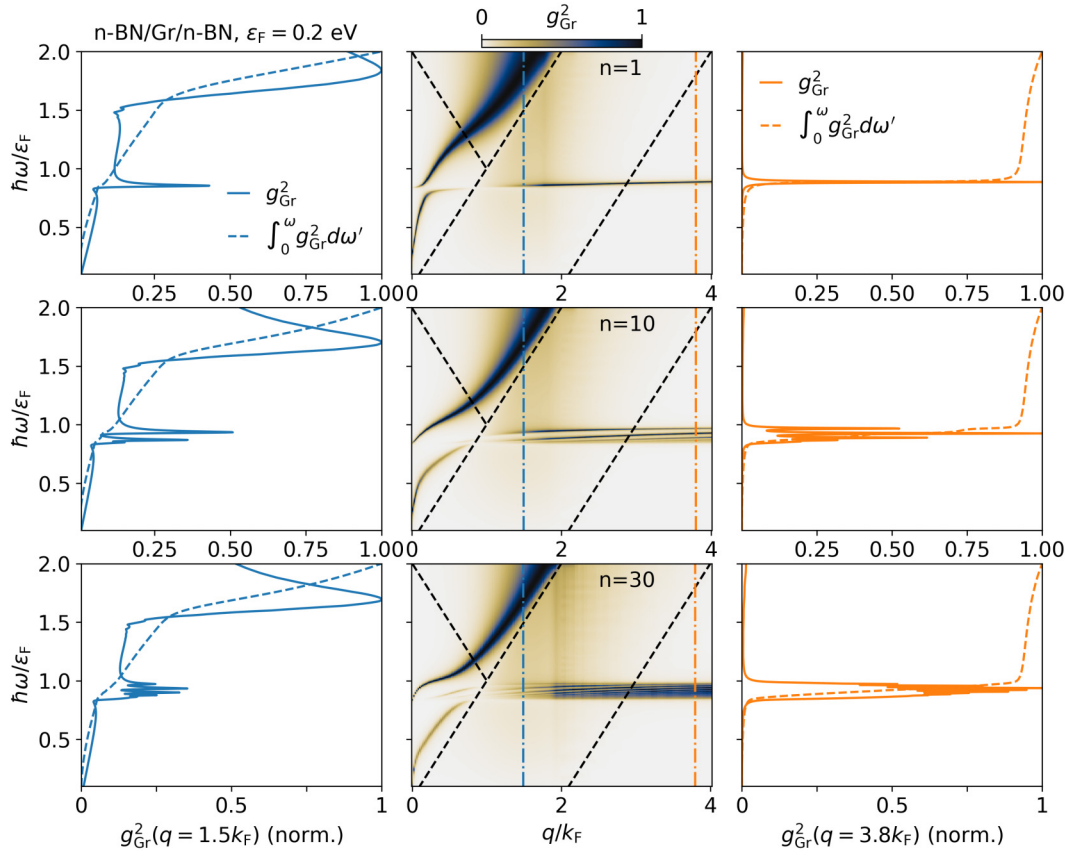


FIG. 10. (Central) $g_{\text{Gr}}^2(q, \omega)$, normalized at each q , for an heterostructure of n-BN/Gr@0.2eV/n-BN, with $n = 1, 10, 30$. The blue and orange vertical lines represent the q values for which $g_{\text{Gr}}^2(\omega)$, and its running integral, are represented in the (left) and (right) panels. In the left panel, the contributions to $g_{\text{Gr}}^2(\omega)$ come from the intraband electron-hole continuum ($\hbar\omega/\varepsilon_{\text{F}} < 1$), from the electron-phonon coupling $\hbar\omega/\varepsilon_{\text{F}} \sim 1$, and from the coupling with the dispersed plasmon in the interband region $\hbar\omega/\varepsilon_{\text{F}} > 1.5$. In the right panel, up to $\hbar\omega/\varepsilon_{\text{F}} > 1.75$ only electron-phonon is present. Notice that the electron-phonon coupling gets contribution from many different modes, contrary to the picture of one single surface phonon responsible for all the interaction.

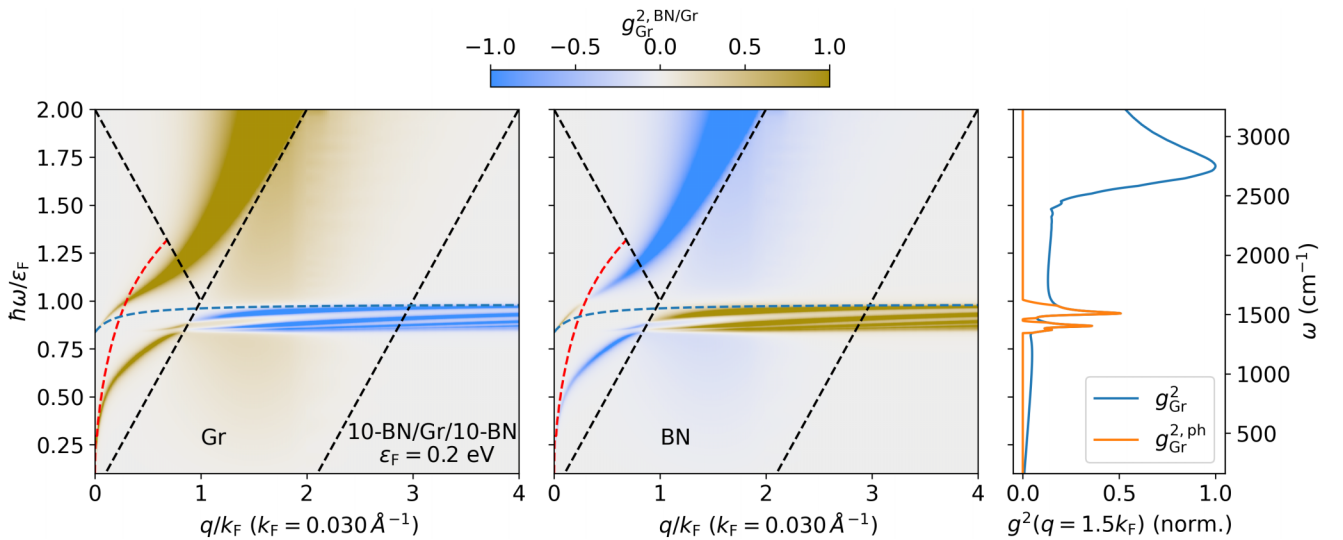


FIG. 11. Contributions to the coupling of graphene's electrons in 10BN/Gr@0.2eV/10BN, i.e., $g_{\text{Gr}}^{2,\text{BN}}(q, \omega)$ and $g_{\text{BN}}^{2,\text{Gr}}(q, \omega)$ as described by Eq. (50), normalized at each q point. We also represent the phonon contribution to the coupling, i.e., $g_{\text{Gr}}^{2,\text{ph}}$ of Eq. (51).

Note that even though each of the above terms may be negative, g_{Gr}^2 is always positive.

We observe similar trends as for the macroscopic $-\text{Im}\chi_M$ of Fig. 5. Three types of coupling emerge: one driven by BN's phonons and screened by graphene when $g_{\text{Gr}}^{2,\text{BN}} > 0$ and $g_{\text{Gr}}^{2,\text{Gr}} < 0$ in region (2); one driven by graphene's plasmon and screened by BN when $g_{\text{Gr}}^{2,\text{Gr}} > 0$ and $g_{\text{Gr}}^{2,\text{BN}} < 0$ in region (1); and one corresponding to a true plasmon-phonon hybrid, when both $g_{\text{Gr}}^{2,\text{BN}} > 0$ and $g_{\text{Gr}}^{2,\text{Gr}} > 0$ in region (3).

Using the information contained within this separation of the contributions, one may define a dynamically screened remote electron-phonon interaction corresponding to the scattering of graphene's electrons by BN's phonons. The phonon-driven contribution to scattering can be systematically extracted, with exact asymptotic limits, as

$$g_{\text{Gr}}^{2,\text{ph}} = \begin{cases} 0 & \text{if } g_{\text{Gr}}^{2,\text{BN}} < 0, \\ g_{\text{Gr}}^{2,\text{BN}} & \text{if } g_{\text{Gr}}^{2,\text{BN}} > 0 \text{ and } g_{\text{Gr}}^{2,\text{Gr}} > 0, \\ g_{\text{Gr}}^2 & \text{if } g_{\text{Gr}}^{2,\text{BN}} > 0 \text{ and } g_{\text{Gr}}^{2,\text{Gr}} < 0. \end{cases} \quad (51)$$

The above procedure of extracting an electron-phonon coupling is arbitrary, but it assures the coupling to be a positive definite quantity. Disentangling plasmon and phonon scattering as such is useful when considering momentum scattering for electronic transport. Despite providing the main contribution, the current procedure does not necessarily provide a full description of the momentum relaxation process. To do so, one could, for example, consider a system of coupled Boltzmann equations for electrons and collective modes [27] for dynamical couplings and carefully extract a momentum relaxation time. We leave this for future studies.

2. Plasmon and phonon contributions

Figure 12 shows the coupling of graphene's electrons with the collective modes for different setups. In the upper panel we plot the total dynamical coupling \bar{g}_{Gr}^2 (black dashed line), compared to electron-phonon part of the coupling $\bar{g}_{\text{Gr}}^{2,\text{ph}}$ (blue line), and to \bar{g}_{Gr}^2 with $Q_{\text{ph,BN}}^0 = 0$ (red line), which represents the plasmon coupling screened by BN's electrons.

The lower panel of Fig. 12 shows the expected asymptotic behaviors for the electron-phonon contribution. At large momenta, $\bar{g}_{\text{Gr}}^{2,\text{ph}}$ coincides with \bar{g}_{Gr}^2 computed with graphene's static electronic response $Q_{\text{el,Gr}}^0(\omega = 0)$. Here, the dynamical nature of the plasmon is not felt, and graphene's free carriers screen the LO phonon statically. We thus recover the static, Born-Oppenheimer approximation of DFPT (see Appendix D for a direct comparison of VED and DFPT electron-phonon couplings in a BN/Graphene system in this regime). In the small momentum limit, the total coupling between electrons and collective modes can be qualitatively divided into two contributions. The dominant part to the total coupling is due to the plasmon (\bar{g}_{Gr}^2 with $Q_{\text{ph,BN}}^0 = 0$). The phonon contribution, $\bar{g}_{\text{Gr}}^{2,\text{ph}}$, is seen to approach \bar{g}_{Gr}^2 with $Q_{\text{el,Gr}}^i = 0$, which represents the electron-phonon coupling obtained by completely suppressing the response from graphene but keeping the static electronic screening from BN. In other words, the phonon is

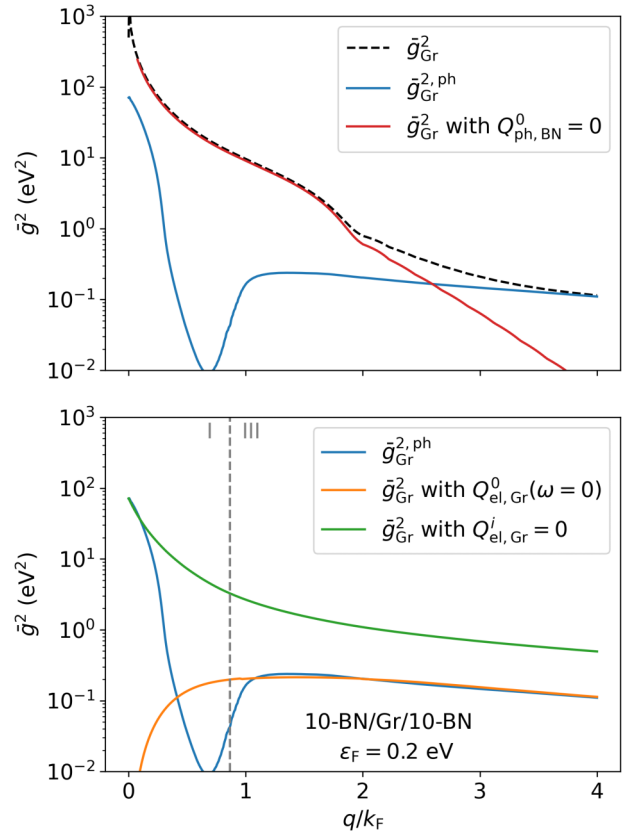


FIG. 12. Coupling between graphene's electrons and collective modes, integrated over positive frequencies, for different setups. (Upper) \bar{g}_{Gr}^2 : in presence of both dynamical phononic and dynamical plasmonic contributions. \bar{g}_{Gr}^2 with $Q_{\text{ph,BN}}^0 = 0$: in the absence of the dynamical phonon contribution from BN, but including the BN's static electronic response. This corresponds to electron-plasmon interaction screened by BN environment. $\bar{g}_{\text{Gr}}^{2,\text{ph}}$: the contribution to the total coupling due to electron-phonon when the responses are all dynamical. (Lower) \bar{g}_{Gr}^2 with $Q_{\text{el,Gr}}^0(\omega = 0)$: in the absence of the dynamical contribution from Gr, i.e., by using the static screening from graphene's electrons. This corresponds to remote electron-phonon coupling screened from graphene in the Born-Oppenheimer approximation, as in DFPT calculations. \bar{g}_{Gr}^2 with $Q_{\text{el,Gr}}^i = 0$: the response of graphene layer is set to zero, i.e., it does not respond to any perturbation. This corresponds to remote electron-phonon coupling screened only by BN's dielectric function. The vertical dashed line indicates the passage from the region where no electron-hole excitation is possible, to the intraband region.

too fast for graphene's electrons to respond. We will refer to the coupling in this region as “intrinsic BN.”

We remind that, following the discussion of Appendix A 3, only in these asymptotic regimes the electron-phonon interaction deduced in this work may be rigorously separated from the electron-plasmon scattering and used inside a Fermi golden rule approach to compute electronic scattering rates due to phonons. In between the asymptotic regimes, following our description there is a region where there is no clear phonon-driven coupling ($g_{\text{Gr}}^{2,\text{BN}} < 0$), which explains the dip in the electron-phonon coupling curve. Nevertheless, the full coupling with the hybrid plasmon-phonon mode could induce some momentum relaxation, which we leave for future

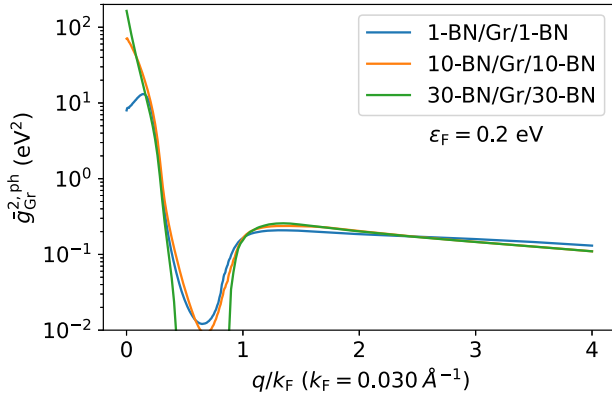


FIG. 13. Evolution of the electron-phonon coupling as a function of the number of BN layers.

studies. Now that we discussed the division of the couplings, we can study the effect of the number of layers and of the Fermi level on the electron-phonon coupling.

3. Effects of number of BN layers

Figure 13 shows the evolution of the electron-phonon coupling as a function of the number of layers. The “intrinsic BN” $q \rightarrow 0$ limit of the (unsquared) electron-phonon coupling increases as $g \propto \frac{n}{\sqrt{n}} = \sqrt{n}$, where n is the number of BN layers. This numerator comes from the sum of the dipole fields over the layers, while the denominator accounts for the the highest LO phonon eigenvector normalization [83]. The coupling decreases with the number of layers at large q . This can be traced back to the intrinsic screening from BN, of the form $\epsilon \sim 1 + N\alpha q + o(q^2)$. There is a saturation in this decrease of the coupling at large q . Indeed, the reach of the interlayer Coulomb interactions goes as e^{-qd} where d is the distance between two given layers. At a given q , graphene only feels BN layers at distance such that $qd \sim 1$. At large q , the threshold d decreases and BN layers added beyond that will not interact with graphene’s electrons.

For the system with only 1 BN on each side and at small q , the coupling can actually be stronger than the “intrinsic BN” coupling, just before reaching it in the $q \rightarrow 0$ limit. The phonon part of the plasmon-phonon hybrid is thus stronger than the intrinsic phonon itself. One may consider that the plasmon is driving the phonon part beyond the normal self-sustained phonon excitation. This is likely due to the relative strength of the plasmon with respect to the phonons.

4. Effects of graphene’s Fermi level

We verified that the plasmon part of the coupling, which is dominant in the $q \rightarrow 0$ limit, reaches a maximum value independent of ϵ_F . Also, removing the atomic contribution to the screening, the electron-plasmon coupling was checked to be mostly independent of the Fermi level in units of q/k_F . Thus, differences in the total coupling at different doping levels are mostly due to the phonon contribution, which we study here.

The upper panel Fig. 14 shows the electron-phonon coupling as a function of the Fermi level in graphene.

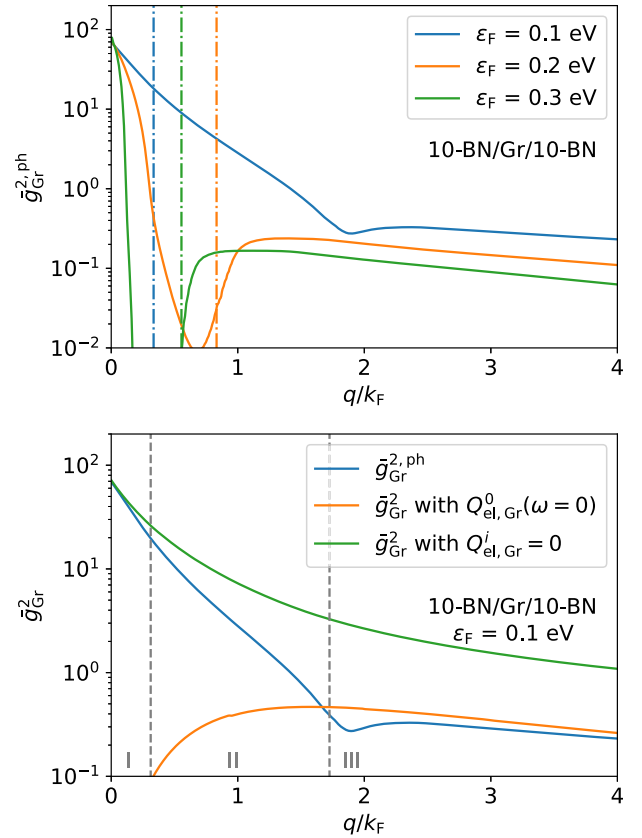


FIG. 14. (Upper) Evolution of the electron-phonon coupling as a function of doping. The vertical dash-dot lines represents the limit of the electron-hole continuum. For transport, only the momenta larger than this limit matter (not a hard limit, modulated by temperature). (Lower) Asymptotic limits of the electron-phonon coupling, as in Fig. 12, but for $\epsilon_F = 0.1$ eV. The vertical dashed lines indicate the passage from the region where no electron-hole excitation is possible, to the interband and then intraband regions.

The VED framework offers an interesting opportunity to elucidate how the electron-phonon interaction is screened by free-carriers as a function of doping. As discussed further in Sec. IV D, this is a nontrivial question in the case of doped 2D semiconductors.

Neglecting screening from graphene is only valid in the $q \rightarrow 0$ limit, where the electron-phonon coupling tends to the intrinsic LO phonon coupling (see lower panels of Figs. 12 and 14). The vertical dashed lines in Fig. 14 show the momenta at which the electron-hole continuum is entered. For $\epsilon_F = 0.2$ and 0.3 eV, this coincides with the onset of strong metallic screening as obtained in the static limit of graphene’s response. Only in the case of $\epsilon_F = 0.1$ eV does the coupling maintain a large value for a considerable interval of wave vectors when entering the electron-hole continuum.

The reason can be traced back to the crossing the interband region II of the electron-hole continuum. In fact, for $\epsilon_F = 0.1$ eV (lower panel of Fig. 14) region I is encountered when $0 < q/k_F < 0.4$, region II when $0.4 < q/k_F < 2$ and region III when $q/k_F > 2$. Instead, for $\epsilon_F = 0.2$ (lower panel of Fig. 12) we have that region II is not encountered, and the

phonons directly cross from regions I to III at $q/k_F \sim 0.9$. At large momenta, for all the Fermi energies the coupling is statically screened by graphene's free carriers. The difference between the curves of Fig. 14 at $q > 2k_F$ is due to q/k_F scale, since graphene's screening is constant and the coupling is independent of k_F .

We conclude that within the electron-hole continuum, the screening of the electron-phonon interaction by graphene's free carriers is always well approximated by its static limit in the intraband continuum. Only when the phonon dispersion crosses the interband continuum does it significantly weaken. In that situation, as shown in Fig. 8, the anticrossing disappears to be replaced by a collective mode which mostly follows the intrinsic LO phonon dispersion. Note that the case of semimetallic graphene is peculiar, since interband transitions are easily accessible, as discussed in Sec. IV D in details.

C. Remote versus intrinsic scattering of graphene's electrons

As a final demonstration of the insight brought by the VED framework, we compare the remote scattering from BN's phonons to the intrinsic scattering from graphene's optical phonons. We focus here on momentum scattering, which contributes to the resistivity of graphene. Following Ref. [63], in graphene, one may define an isotropic and energy-dependent transport scattering time τ^{Tr} from which the resistivity may be expressed as

$$\frac{1}{\rho} = \frac{e^2}{\pi \hbar^2} \int_{-\infty}^{\infty} d\varepsilon |\varepsilon| \tau^{\text{Tr}}(\varepsilon) \left(-\frac{\partial n_{\varepsilon}^{\text{FD}}}{\partial \varepsilon} \right). \quad (52)$$

In general, $\tau^{\text{Tr}}(\varepsilon)$ is obtained by solving the full Boltzmann transport equations, i.e., a set of coupled equations relating τ^{Tr} at different energies [63]. All phonons contribute to each of the coupled equations, and it is not straightforward to separate their respective contributions to $\tau^{\text{Tr}}(\varepsilon)$. However, within the relaxation time approximation ($\tau^{\text{Tr}}(\varepsilon)$ weakly dependent on energy), the equations decouple and the scattering rate $\tau^{\text{Tr},-1}(\varepsilon)$ (i.e., the inverse of the scattering time) is trivially expressed as a sum over phonon modes. The quantitative impact on the intrinsic resistivity is negligible at room temperature and in the range of Fermi levels studied here (see Fig. 6 of Ref. [63]). Within this approximation, it is thus reasonable to compute and compare scattering rates from each type of phonons. $\tau^{\text{Tr},-1}$ then differs from the self-energy/ARPES scattering rates τ^{-1} [Eq. (41)] by an additional $(1 - \cos \theta)$ term inside the angular integration, where θ is the scattering angle between \mathbf{k} and $\mathbf{k} + \mathbf{q}$. That term gives more importance to the back-scattering transitions [63] ($\theta = \pi$). Finally, notice that those approximations preserve the electron-hole symmetry of scattering rates.

For *intrinsic scattering mechanisms* in graphene, we use results from Appendix B of Ref. [63]. We focus on the scattering rates coming from LO and TO phonons at zone center ($q \sim \Gamma$) with frequency $\omega_{\text{LO}\Gamma} = \omega_{\text{TO}\Gamma} = \omega_0 \sim 0.2\text{eV}$, and A_1 phonons at zone border ($q \sim K$) with frequency $\omega_K \sim 0.15\text{eV}$. Keeping only phonon-dependent quantities, the

transport scattering rate from the sum of LO and TO phonons is proportional to

$$\begin{aligned} \tau_0^{\text{tr},-1}(\varepsilon) &= \frac{\hbar \beta_0^2}{2M\omega_0} \mathcal{W}_{\pm}(\hbar\omega_0, \varepsilon), \quad (53) \\ \mathcal{W}_{\pm}(\hbar\omega_0, \varepsilon) &= \left(n_{\omega_0}^{\text{BE}} + \frac{1}{2} \mp \frac{1}{2} \right) \\ &\quad \times \frac{|\varepsilon \pm \hbar\omega_0|}{(\hbar v_F)^2 (1 - n_{\varepsilon \pm \hbar\omega_0}^{\text{FD}})}, \quad (54) \end{aligned}$$

where the summation over both the \pm terms is intended (“+” stands for absorption and “−” for emission). β_0 is the strength of the optical electron-phonon coupling, with $\frac{\hbar \beta_0^2}{2M\omega_0} = 0.11 \text{ eV}^2$ as obtained from GW calculations. M is the mass of carbon atoms, and n^{BE} and n^{FD} are taken at room temperature here. The scattering rate for the zone-border phonon at K reads

$$\begin{aligned} \tau_K^{\text{tr},-1}(\varepsilon) &= \frac{\hbar \beta_K^2}{2M\omega_K} \mathcal{W}_{\pm}(\hbar\omega_K, \varepsilon) \int \frac{d\theta}{2\pi} (1 - s_K \cos \theta) \\ (1 - \cos \theta) &= \frac{\hbar \beta_K^2}{2M\omega_K} \mathcal{W}_{\pm}(\hbar\omega_K, \varepsilon) \left(1 + s_K \frac{1}{2} \right), \quad (55) \end{aligned}$$

where $s_K = \text{sign}(\varepsilon) \text{sign}(\varepsilon \pm \hbar\omega_K)$ is positive (negative) for intraband (interband) transitions, and $\frac{\hbar \beta_K^2}{2M\omega_K} = 0.18 \text{ eV}^2$ as obtained from GW calculations at large doping [90]. The calculation of the correct value for β_K , in particular at small doping, is still matter of active theoretical and experimental research [43,91,92]. The value used here is a lower limit, such that the scattering from those phonons is likely much stronger in practice. The first factor in the integral comes from the angular dependence of the wave functions bracketing the electron-phonon interaction, with a different sign of the cosine for intraband and interband transitions. The second is the usual angular term in transport giving more importance to the back-scattering transitions.

For *remote scattering from BN's phonons*, we compute the scattering time as explained in Appendix A 4. In particular, we start from Eq. (41) and insert the $(1 - \cos \theta)$ term. Then, as for the intrinsic scattering, we assume that the relevant BN's phonons are dispersionless phonons of frequency $\sim \omega_{\text{BN}} = 0.18\text{eV}$. We then consider only contributions coming from electron-phonon scattering, i.e., we consider only the coupling $\bar{g}_{\text{Gr}}^{2,\text{ph}}$, which is isotropic in momentum space to a very good approximation. Energy conservation is imposed, and the sum over \mathbf{q} points transform in an angular integral. Since energy conservation changes from emission to absorption, we define the admitted scattering wave vectors, at a given θ , as q_{θ}^{\pm} (see Fig. 15). As detailed in Appendix A 4 we obtain that the remote phonon scattering rate is proportional to

$$\begin{aligned} \tau_{\text{BN}}^{\text{tr},-1}(\varepsilon) &= \mathcal{W}_{\pm}(\hbar\omega_{\text{BN}}, \varepsilon) \int \frac{d\theta}{2\pi} \bar{g}_{\text{Gr}}^{2,\text{ph}}(q_{\theta}^{\pm}) \frac{1 + s_{\text{BN}} \cos \theta}{2} \\ &\quad \times (1 - \cos \theta), \quad (56) \end{aligned}$$

where $s_{\text{BN}} = \text{sign}(\varepsilon) \text{sign}(\varepsilon \pm \hbar\omega_{\text{BN}})$. The value of $\bar{g}_{\text{Gr}}^{2,\text{ph}}(q_{\theta}^{\pm})$ is taken from Fig. 14. Note that the sign of the cosine in the first term of in the angular integral of Eq. (56), still depending on whether the transition is intra- or interband, is reversed with respect to Eq. (55). This is easily understood noting that

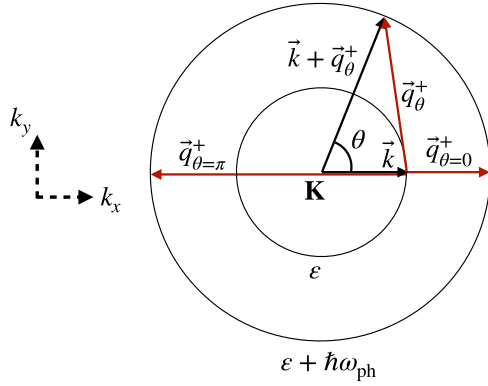


FIG. 15. Scattering process for an electron with an initial energy ε . Graphical representation of the isoenergetic surface at ε and $\varepsilon + \hbar\omega_{\text{ph}}$, on which the electron ends up after an absorption of a phonon of frequency ω_{ph} . In this case, we are representing an electron-doped Dirac cone. Several different setups of the Fermi surface and the isoenergetic surfaces are possible in dependence of the relative magnitude of ε and ω_{ph} , and considering also the emission case.

the zone border phonon at \mathbf{K} leads to an intervalley transition, while BN's phonons scatter within the same \mathbf{K} valley.

We evaluate the transport scattering rates for $\varepsilon = \varepsilon_{\text{F}} = 0.1, 0.2, 0.3$ eV for heterostructures with n -BN layers on each side, $n = 1, 10, 30$, at room temperature (300 K). The results are presented in Table I. For $\varepsilon_{\text{F}} = 0.2, 0.3$ eV, we find that $\tau_{\text{BN}}^{\text{tr},-1}(\varepsilon_{\text{F}})/\tau_{\text{O}}^{\text{tr},-1}(\varepsilon_{\text{F}}) < 1$ while $\tau_{\text{BN}}^{\text{tr},-1}(\varepsilon_{\text{F}})/\tau_{\text{K}}^{\text{tr},-1}(\varepsilon_{\text{F}}) \ll 1$. For these doping levels $\varepsilon_{\text{F}} > \hbar\omega_{\text{BN}}$, therefore the admitted scattering is intraband. The remote coupling with BN's LO phonon is always screened by graphene. To understand why in this case remote scattering is smaller than the intrinsic zone center optical scattering, we remark that the electron-phonon coupling for graphene's intrinsic LO and TO phonons is $\frac{\hbar\beta_{\text{O}}^2}{2M\omega_{\text{O}}} = 0.11$ eV², independent of the scattering angle [63]. Figure 14 shows coupling strengths around the same value for BN's polar phonons. However, the scattering rates also include graphene's electronic wave-function overlap. Since for intraband transitions this factor vanishes in back-scattering geometry ($s_{\text{BN}} = 1$), i.e., the most important for transport, one obtains a contribution smaller than graphene's zone center

TABLE I. Ratio of remote transport scattering rates $\tau_{\text{BN}}^{\text{tr},-1}(\varepsilon_{\text{F}})$ and the intrinsic zone-center $\tau_{\text{O}}^{\text{tr},-1}(\varepsilon_{\text{F}})$ or zone-boundary $\tau_{\text{K}}^{\text{tr},-1}(\varepsilon_{\text{F}})$ ones, for a temperature of $T = 300$ K.

ε_{F} (eV)	n	$\tau_{\text{BN}}^{\text{tr},-1}(\varepsilon_{\text{F}})/\tau_{\text{O}}^{\text{tr},-1}(\varepsilon_{\text{F}})$	$\tau_{\text{BN}}^{\text{tr},-1}(\varepsilon_{\text{F}})/\tau_{\text{K}}^{\text{tr},-1}(\varepsilon_{\text{F}})$
0.1	1	2.24	0.20
	10	2.80	0.25
	30	2.23	0.20
0.2	1	0.87	0.052
	10	0.92	0.055
	30	0.92	0.055
0.3	1	0.67	0.04
	10	0.67	0.04
	30	0.78	0.05

optical phonons in transport, themselves scattering much less than zone border A_1 phonons. This holds also for large number of BN layers, since the coupling is essentially independent of the number of layers for large enough momenta; see Fig. 13. Increasing doping further only weakens the relative contribution from BN's phonons.

For $\varepsilon_{\text{F}} = 0.1$ eV, the situation is different. We find that $\tau_{\text{BN}}^{\text{tr},-1}(\varepsilon_{\text{F}})/\tau_{\text{O}}^{\text{tr},-1}(\varepsilon_{\text{F}}) > 1$, but still $\tau_{\text{BN}}^{\text{tr},-1}(\varepsilon_{\text{F}})/\tau_{\text{K}}^{\text{tr},-1}(\varepsilon_{\text{F}}) < 1$. To understand why now remote phonons are more important than intrinsic zone-center phonons, we notice that at small doping the possibility of unscreened interband transitions increases the scattering rate due to a strong coupling, as shown in Fig. 14. Further, for interband process the overlap of graphene's wave functions now reaches a maximum in the back-scattering geometry ($s_{\text{BN}} = -1$). The contribution of BN's LO phonons to graphene's resistivity is thus larger and comparable to the intrinsic contribution from graphene's LO and TO phonons. However, we find that the scattering from BN's phonons remains smaller than the contribution of intrinsic optical A_1 phonons at \mathbf{K} at room temperature, despite the overall larger coupling. This is due to the strong reduction of the remote phonon scattering at small θ , and therefore small q , due to the $(1 - \cos \theta)^2$ angular factor, and to the role played by phonon occupation factors at room temperature. For the intraband contribution (related to phonon absorption), the final electronic states are at $\varepsilon_{\text{F}} = 0.3$ eV, and the norm of the corresponding momenta go from $2k_{\text{F}}$ to $4k_{\text{F}}$, where the remote coupling is screened. Let us underscore the use of a conservative estimate for coupling to the optical A_1 phonons at \mathbf{K} , such that they would scatter *at least* four times more than remote BN phonons.

In conclusion, remote electron-phonon coupling with BN's LO phonons does not seem to explain the discrepancies seen between *ab initio* simulations of intrinsic phonon-limited transport in graphene and experiments in BN-capped graphene at room temperature and higher [63,93,94]. However, while we do not expect the dominance of the A_1 phonons at \mathbf{K} to be challenged, a more accurate assessment of BN's remote contributions to graphene's resistivity is left for future investigations. Indeed, BN's out-of-plane ZO phonons would also participate to electron scattering and, as mentioned before, the definition of electron-phonon coupling proposed here does not describe the full momentum relaxation process from the plasmon-phonon excitation.

D. Discussion: Screening of electron-phonon interactions in doped 2D semiconductors

In this work we specifically quantify the remote scattering of graphene's electrons from BN's phonons. More generally, qualitative conclusions can be drawn on the scattering from long-range polar phonons in doped 2D semiconductors. In particular, the VED framework sheds some light on the screening of those phonons from the free carriers added by doping.

Without computing the full dynamical response as done here, there are two easily accessible limits used in the literature: static screening or no screening. It is general knowledge that static screening should be used at high doping when the plasma frequency (which increases with free carrier

density) is expected to be well above the phonon frequency, i.e., phonons are much slower than free carriers. In the opposite small doping limit, one may neglect free-carrier screening if the plasma frequency is much smaller than the phonon, i.e., phonons are much faster than free carriers. In the case of 2D materials, the universal square root behavior of the plasmon dispersion $\omega_{\text{pl}} \propto \sqrt{q}$ (as opposed to a constant in 3D) somewhat complicates the picture, as there is no single plasma frequency to compare to. The systems studied in this work are then an instructive example for the 2D case.

We only consider scattering rates that involve real states, i.e., within the electron-hole continua. Since the scattering mechanisms sensitive to screening mostly come from polar-optical phonons, we can assume the existence of a constant typical phonon frequency ω_{ph} , despite the presence of a linear dispersion at small momenta. If ω_{ph} is lower than the onset of the interband electron-hole continuum ω_{inter} , i.e., if $\omega_{\text{ph}} < \omega_{\text{inter}}$, then the screening of scattering from polar phonons by free carriers is always effective, as in the case of the lower panel of Fig. 12. Indeed, in this case the phonon dispersion only crosses the electron-hole continuum in the intraband Landau damping region. When $\omega_{\text{ph}} > \omega_{\text{inter}}$, the situation is similar to the lower panel of Fig. 14. While screening remains effective in the intraband continuum, the phonon also crosses the interband continuum, where free-carrier screening vanishes or at least is weaker.

Graphene being gapless, ω_{inter} can be made very small with respect to ω_{ph} by lowering the doping. Typical high-mobility doped semiconductors, however, have a well-isolated transport band [95], and ω_{inter} remains finite even at vanishing doping. Further, other bands are far enough that $\omega_{\text{ph}} < \omega_{\text{inter}}$, in which case the strong screening from free carriers is effective. Of course, the assessment of a realistic situations is more complex, with multiple phonon frequencies and multiple onsets of interband transitions to be considered.

Nevertheless, given the above arguments, we conclude that simply neglecting free-carrier screening in 2D doped semiconductors is not valid, even in the low doping limit. Yet, this approximation is often done in state-of-the-art first-principles electronic transport calculations [96–104]. Instead, without access to the full dynamical screening, using the static free-carrier screening might be a more reasonable and robust approximation [19,53,65,95,105,106].

V. CONCLUSIONS

In summary, we have developed an *ab initio* computational technique capable of describing plasmons, phonons and their mixing in Van der Waals heterostructures. We avoid the computational effort of simulating the full heterostructure. Instead, single-layer response functions are computed and inserted in a system of equations that takes into account the electrodynamic interactions between different layers. Despite the reduced computational cost, our method is able to reproduce the results obtained by full *ab initio* calculations in the static limit of electronic responses, and extends to the dynamical case. Those developments are applied to BN-capped graphene, where we study the features of the collective excitations and their evolution when changing the number of BN layers and the doping level. In particular, we show that the phonon and plasmon

mode mixing generates interesting observable results, such as the stiffening of the plasmon-phonon-polariton group velocity due to both vanishing remote screening of BN’s phonons from graphene and the interplay with the plasmon. We also obtain the coupling of the collective modes with electrons of the heterostructure. In particular, we investigate the role played by the plasmon in screening the remote electron-phonon coupling between graphene’s electrons and BN’s LO phonons. We quantitatively describe the crossover between the regions where the coupling is screened by graphene’s free carriers (intraband region), to the one where it is not (interband region). This implies a contribution to graphene’s low doping resistivity from remote BN’s LO phonons that is similar to graphene’s zone-center optical phonons, but it is still negligible with respect to the scattering from intrinsic zone-border optical phonons. Thus, it is not sufficient to explain the large discrepancy between experiments and state-of-the-art *ab initio* simulations [63,93,94,107]. For a general heterostructure, one expects the interplay between plasmons and phonons to increase in complexity. This may be due to a complex band structure of the metallic layer presenting, e.g., subbands [108], intersubband or multivalley [109] plasmons, or to an increased importance of cross-talks between in-plane and out-of-plane electrostatics [60]. Both of these cases are exciting perspectives for this work.

ACKNOWLEDGMENTS

We thank A. Guandalini, P. Barone, M. Stengel, M. Gibertini, and G. Cassabois for useful discussions. F. Mauri and F. Macheda acknowledge the MORE-TEM ERC-SYN project, Grant Agreement No. 95121. F. Mauri and F. Macheda acknowledge the EuroHPC Joint Undertaking for awarding this project access to the EuroHPC supercomputer LUMI, hosted by CSC (Finland) and the LUMI consortium through a EuroHPC Regular Access call. First-principles calculations were performed with the support of the ISDM-MESO Platform at the University of Montpellier funded under the CPER by the French Government, the Occitanie Region, the Metropole of Montpellier and the University of Montpellier.

APPENDIX A: THEORETICAL ASPECTS OF DISPERSIONS, COUPLINGS, AND SCATTERING RATES

1. Basic definitions

In this Appendix we restore the possible anisotropy of the system using the vector symbols (as, e.g., \mathbf{q} and \mathbf{r}) for momentum and space related quantities. We assume time-reversal symmetry in the whole manuscript. We define a generic retarded response as

$$f^{\text{R}}(\mathbf{r}, \mathbf{r}', t) = -\frac{i}{\hbar} \theta(t) \langle [\hat{A}(\mathbf{r}, t), \hat{A}(\mathbf{r}')] \rangle, \quad (\text{A1})$$

where $\langle \rangle$ indicates the average over the ground state (or the thermal average), θ is the Heaviside function, and \hat{A} is a generic operator. Its Fourier transform satisfies the property

$$f^{\text{R}}(\mathbf{q}, \omega) = [f^{\text{R}}(\mathbf{q}, -\omega)]^*. \quad (\text{A2})$$

The retarded density-density response function in the RPA is expressed as a function of the irreducible independent-particle

density-density response $\chi_{\text{irr}}^{\text{R}}$ as in Eq. (26). The noninteracting retarded Green function for a phonon of branch μ at zero temperature may be written as a function of the harmonic oscillator ladder operators a, a^\dagger in real time as

$$D_\mu^{\text{R}}(\mathbf{q}, t) = -i\theta(t)\langle \hat{a}_{\mu\mathbf{q}}^\dagger(t)a_{\mu\mathbf{q}}^\dagger + a_{\mu-\mathbf{q}}(t)a_{\mu-\mathbf{q}}^\dagger \rangle, \quad (\text{A3})$$

and in the frequency space as

$$D_\mu^{\text{R}}(\mathbf{q}, \omega) = \frac{2\hbar\omega_{\mu\mathbf{q}}}{(\hbar\omega + i\hbar\eta)^2 - \hbar^2\omega_{\mu\mathbf{q}}^2} = \quad (\text{A4})$$

$$-\frac{1}{\hbar\omega + \hbar\omega_{\mu\mathbf{q}} + i\hbar\eta} + \frac{1}{\hbar\omega - \hbar\omega_{\mu\mathbf{q}} + i\hbar\eta}. \quad (\text{A5})$$

As shown later, the expression of the total inverse dielectric function contains the density-density response and the phonon propagator, both in the retarded flavor. We drop the retarded apex everywhere in the text, so that any Green/response function is to be intended as retarded. We also remind that to deduce the finite temperature expression of the retarded Green/response functions, one computes their time ordered expression in the Matsubara formalism and then performs the substitution $i\hbar\omega_n \rightarrow \hbar\omega + i\hbar\eta$ [69]. As a consequence of using retarded Green functions, all the computed quantities will be analytical and will therefore respect the Kramers-Kronig relations [110].

2. Long-range atomic-mediated inverse dielectric function/screened Coulomb

The goal of this section is to justify the form of Eq. (28) for a wide gap semiconductor such as BN. Therefore, we here perform the derivation of the long-range atomic-mediated inverse dielectric function and the related screened Coulomb interaction. We start from the derivation for the 3D case. In this case, following Ref. [111] we use the RPA approximation for the electronic response and obtain that the atomic-mediated inverse dielectric function can be expressed in terms of effective charges. We then use the conclusions and procedures of Ref. [65] to extend the results to the case of a 2D single layer of small width.

a. Three-dimensional expression for the inverse dielectric function

The screened electronic interaction is defined as [4]

$$v(\mathbf{r}) = \frac{4\pi e^2}{|\mathbf{r}|}, \quad (\text{A6})$$

$$w(41) = \int d\mathbf{r}'' \epsilon^{-1}(4, \mathbf{r}'', t_1) v(\mathbf{r}'' - \mathbf{r}_1), \quad (\text{A7})$$

where the compact notation $1 = (\mathbf{r}_1, t_1)$ has been introduced. The total inverse dielectric function—and consequently the Coulomb potential—is usually split into “electronic” (clamped-ion) and “phononic” (total minus clamped-ion) contributions as

$$\epsilon^{-1} = \epsilon_{\text{el}}^{-1} + \epsilon_{\text{ph}}^{-1}, \quad w = w_{\text{el}} + w_{\text{ph}}. \quad (\text{A8})$$

Such separation bring great simplification if vertex corrections that couple the systems are small [69], as assumed here. The

phononic part of the screened Coulomb interaction may be written, following Refs. [112–114], as

$$\begin{aligned} \epsilon_{\text{ph}}^{-1}(12) &= \sum_{\substack{s\alpha p \\ s'\alpha' p'}} \int d(34) \epsilon_{\text{el}}^{-1}(13) (\nabla_{\mathbf{r}_3})_\alpha V_s(\mathbf{r}_3 - \mathbf{u}_s^p) \\ &\times D_{s\alpha p, s'\alpha' p'}(t_3 t_4) \frac{-\nabla_{\mathbf{r}_4}^2}{4\pi e^2} \epsilon_{\text{el}}^{-1}(42) (\nabla_{\mathbf{r}_4})_{\alpha'} \\ &\times V_{s'}(\mathbf{r}_4 - \mathbf{u}_{s'}^{p'}), \end{aligned} \quad (\text{A9})$$

where D is the dressed phonon propagator. $\mathbf{u}_s^p = \mathbf{R}_p + \boldsymbol{\tau}_s$ are the atomic equilibrium positions, which in reciprocal space representation read as

$$\mathbf{u}_s^{\mathbf{q}} = \sum_p e^{i\mathbf{q}\cdot(\mathbf{R}+\boldsymbol{\tau}_s)} \mathbf{u}_s^p. \quad (\text{A10})$$

V_s indicates, in the all-electron formalism, the ion-electron interaction due to the ion at site s , and its Fourier transform is

$$V_{s\alpha}(\mathbf{q} + \mathbf{G}) = \frac{1}{e} v(\mathbf{q} + \mathbf{G}) \rho_{s\alpha}^{\text{ext}}(\mathbf{q} + \mathbf{G}), \quad (\text{A11})$$

$$\rho_{s\alpha}^{\text{ext}}(\mathbf{q} + \mathbf{G}) = -i \frac{\mathcal{Z}_s e}{V} [(q_\alpha + G_\alpha) e^{-i\mathbf{G}\cdot\boldsymbol{\tau}_s}], \quad (\text{A12})$$

where \mathcal{Z}_s are the ionic charges. We assume to be looking at times large enough that all the response functions depend only on relative time, the retardation condition restoring the causality at the end. We express the phonon propagator as

$$\begin{aligned} D_{s\alpha p, s'\alpha' p'}(\omega) &= \frac{1}{\sqrt{M_s M_{s'}}} \sum_\mu \int \frac{d\mathbf{q}}{V_{\text{BZ}}} \\ &\times \frac{e^{s\alpha} e^{i\mathbf{q}\cdot(\mathbf{R}_p+\boldsymbol{\tau}_s)} e^{s'\alpha' *} e^{-i\mathbf{q}\cdot(\mathbf{R}_{p'}+\boldsymbol{\tau}_{s'})}}{(\hbar\omega + i\hbar\eta)^2 - \hbar^2\omega_{\mu\mathbf{q}}^2}, \end{aligned} \quad (\text{A13})$$

where $e_{\mu\mathbf{q}}^{s\alpha}$ are eigenvectors of the dynamical matrix and $\omega_{\mu\mathbf{q}}$ its eigenvalues. Notice that we have written the phonon propagator but did not explicit the value of the poles. The poles are determined by a Dyson equation which takes into account the effects of electronic screening on the phonon self-energy [69]. In a simple Frölich model Hamiltonian, the poles determined as the frequency of the TO mode renormalized by the real part of the phonon self-energy of the Frölich model, computed with appropriate dynamical screening; notice that in our formalism this dynamical renormalization is automatically taken into account. Indeed, we specify the value of the phonon poles only for the single-layer BN, for which they coincide with the LO frequencies. Notice also that we disregard imaginary parts of the phononic self-energy in the following, considering the phonon propagator in the “clean limit.”

We now introduce the in-plane screened and unscreened charge densities, and related effective charges, in the RPA approximation for $\epsilon_{\text{el}}^{-1}$ [65,111,115–118]. These read as

$$\rho_{s\alpha}(\mathbf{q}, \omega) = \epsilon_{\text{el}}^{-1}(\mathbf{q}, \omega) \bar{\rho}_{s\alpha}(\mathbf{q}, \omega), \quad (\text{A14})$$

$$\bar{Z}_{s\alpha}(\mathbf{q}, \omega) = i \frac{V}{e\mathbf{q}} \bar{\rho}_{s\alpha}(\mathbf{q}, \omega). \quad (\text{A15})$$

An explicit expression for the effective charges is found as

$$\begin{aligned} \bar{Z}_{s\alpha}(\mathbf{q}, \omega) &= \frac{Z_s}{qv(\mathbf{q})} \sum_{\mathbf{G}} \frac{\epsilon_{\text{el}}^{-1}(\mathbf{q}, \mathbf{q} + \mathbf{G}, \omega)}{\epsilon_{\text{el}}^{-1}(\mathbf{q}, \omega)} (q_\alpha + G_\alpha) \\ &\times v(\mathbf{q} + \mathbf{G}) e^{-i\mathbf{G} \cdot \boldsymbol{\tau}_s}, \end{aligned} \quad (\text{A16})$$

$$\begin{aligned} w_{\text{ph}}(\mathbf{q}, \omega) &= -\frac{1}{V} q^2 [w_{\text{el}}(\mathbf{q}, \omega)]^2 \frac{1}{\sqrt{M_s M_{s'}}} \sum_{\mu} \frac{(\sum_{s\alpha} \bar{Z}_{s\alpha}(\mathbf{q}, \omega) e_{\mu\mathbf{q}}^{s\alpha}) (\sum_{s'\alpha'} \bar{Z}_{s'\alpha'}(-\mathbf{q}, \omega) e_{\mu-\mathbf{q}}^{s'\alpha'})}{(\hbar\omega + i\hbar\eta)^2 - \hbar^2 \omega_{\mu\mathbf{q}}^2} \\ &= \frac{V}{e^2} [w_{\text{el}}(\mathbf{q}, \omega)]^2 \frac{1}{\sqrt{M_s M_{s'}}} \sum_{\mu} \frac{(\sum_{s\alpha} \bar{\rho}_{s\alpha}(\mathbf{q}, \omega) e_{\mu\mathbf{q}}^{s\alpha}) (\sum_{s'\alpha'} \bar{\rho}_{s'\alpha'}(-\mathbf{q}, \omega) e_{\mu-\mathbf{q}}^{s'\alpha'})}{(\hbar\omega + i\hbar\eta)^2 - \hbar^2 \omega_{\mu\mathbf{q}}^2}, \end{aligned} \quad (\text{A17})$$

where

$$e_{\mu-\mathbf{q}}^{s'\alpha'} = e_{\mu\mathbf{q}}^{s'\alpha'*}. \quad (\text{A18})$$

For an isolant such as BN, for frequencies much smaller than the band gap, we have

$$\epsilon_{\text{el}}^{-1}(\mathbf{q}, \omega) \sim \epsilon_{\text{el}}^{-1}(\mathbf{q}), \quad \bar{Z}(\mathbf{q}, \omega) \sim \bar{Z}(\mathbf{q}). \quad (\text{A19})$$

The unscreened effective charges have an expansion of the form [65,111]

$$\begin{aligned} \bar{Z}_{s\alpha}(\mathbf{q}) &= \frac{q_\beta}{q} \bar{Z}_{s\beta\alpha} - \frac{i}{2} \frac{q_\beta}{q} q_\gamma Q_{s\alpha\beta\gamma} + -\frac{1}{3!} \frac{q_\beta}{q} q_\gamma q_\delta O_{s\alpha\beta\gamma\delta} \\ &+ \mathcal{O}(q^3), \end{aligned}$$

where the various orders of the expansion are the Born effective charges, dynamical quadrupoles and octupoles, as so on. With the above expansion, at leading order in q , one can rewrite Eq. (A17) as

$$\begin{aligned} w_{\text{ph}}(\mathbf{q}, \omega) &= \frac{1}{V} \sum_{s\alpha\beta, s'\alpha'\beta'} [w_{\text{el}}(\mathbf{q})]^2 \frac{1}{\sqrt{M_s M_{s'}}} \\ &\times \sum_{\mu} \frac{(\sum_{s\alpha\beta} \bar{Z}_{s\beta\alpha} q_\beta e_{\mu\mathbf{q}}^{s\alpha}) (\sum_{s'\alpha'\beta'} \bar{Z}_{s'\beta'\alpha'} q_{\beta'} e_{\mu-\mathbf{q}}^{s'\alpha'*})}{(\hbar\omega + i\hbar\eta)^2 - \hbar^2 \omega_{\mu\mathbf{q}}^2}, \end{aligned} \quad (\text{A20})$$

which is consistent with the form obtained in Ref. [4]. Equation (A20) includes only the leading order Frölich coupling [119–123], whereas Eq. (A17) include quadrupoles and higher multipolar order expansions [60,97,124]. Using the form of Eq. (28) of Ref. [65], one can rewrite the equivalent of Eq. (A17) for the inverse dielectric matrix in the static case as a function of the long-range component of the dynamical matrix:

$$\epsilon_{\text{ph}}^{-1}(\mathbf{q}, \omega) = \epsilon_{\text{el}}^{-1}(\mathbf{q}) \sum_{\mu} \frac{\mathbf{e}_{\mu\mathbf{q}} \mathcal{D}^{\text{L}}(\mathbf{q}) \mathbf{e}_{\mu\mathbf{q}}^*}{(\hbar\omega + i\hbar\eta)^2 - \hbar^2 \omega_{\mu\mathbf{q}}^2}. \quad (\text{A21})$$

b. Two-dimensional case for a single BN single layer

As in the rest of this work, for a BN single layer we only consider in-plane displacements of atoms, and suppose

where \mathbf{G} are reciprocal lattice vectors. Using all the above expressions, and Fourier transforming Eq. (A9), we find for the atomic-mediated macroscopic component of the Coulomb interaction

that there are no cross-talks between in-plane and out-of-plane components of the response functions. The error of this assumption, since our single layers always present in-plane mirror symmetry, is of order $\mathcal{O}(q^2 z^2)$. As explained in Ref. [65], if one also assumes that the material thickness is much smaller than the wavelength of the perturbation (thin limit), one can then forget about the out-of-plane direction of the electrostatic problem and, for the formulas of Appendix A 2 a, replace the three-dimensional Coulomb kernel with its two-dimensional counterpart, and volume-intensive quantities with the area-intensive ones. In this work, we extend the validity of 2D formulas beyond the thin limit by using Eq. (16) to describe the 2D Coulomb interaction. We finally obtain for the LO phonon, assuming a small finite lifetime

$$[\epsilon_{\text{IL,ph}}^{-1}]^0(\mathbf{q}, \omega) = [\epsilon_{\text{IL,el}}^{-1}]^0(\mathbf{q}) \frac{\mathbf{e}_{\text{LOq}} \mathcal{D}^{\text{L}}(\mathbf{q}) \mathbf{e}_{\text{LOq}}^*}{(\hbar\omega + i\hbar\eta_{\text{LO}})^2 - \hbar^2 \omega_{\text{LOq}}^2}, \quad (\text{A22})$$

$$[\epsilon_{\text{IL,el}}^{-1}]^0(\mathbf{q}) = 1 + v_{\text{BN, BN}}^{\text{00}}(\mathbf{q}) Q_{\text{el}}^0(\mathbf{q}), \quad (\text{A23})$$

$$[\epsilon_{\text{IL,ph}}^{-1}]^1(\mathbf{q}, \omega) = 0. \quad (\text{A24})$$

The above equations are the one used, for the isotropic case, in Sec. II A 6. The explicit expression of the numerator of Eq. (A22) for the thin limit is [65]

$$\begin{aligned} \mathbf{e}_{\text{LOq}} \mathcal{D}^{\text{L}}(\mathbf{q}) \mathbf{e}_{\text{LOq}}^* &= \frac{2\pi A}{q} \left(\sum_{s\alpha} \rho_{s\alpha}(\mathbf{q}) \frac{e_{\text{LOq}}^{s\alpha}}{\sqrt{M_s}} \right) \\ &\times \left(\sum_{s'\alpha'} \bar{\rho}_{s'\alpha'}(\mathbf{q}) \frac{e_{\text{LOq}}^{s'\alpha'}}{\sqrt{M_{s'}}} \right)^*. \end{aligned} \quad (\text{A25})$$

In the approximation of this work that the atomic profile density is the same of the electronic one, we extend the above expression to

$$\begin{aligned} \mathbf{e}_{\text{LOq}} \mathcal{D}^{\text{L}}(\mathbf{q}) \mathbf{e}_{\text{LOq}}^* &= A v_{\text{BN, BN}}^{\text{00}} \left(\sum_{s\alpha} \rho_{s\alpha}(\mathbf{q}) \frac{e_{\text{LOq}}^{s\alpha}}{\sqrt{M_s}} \right) \\ &\times \left(\sum_{s'\alpha'} \bar{\rho}_{s'\alpha'}(\mathbf{q}) \frac{e_{\text{LOq}}^{s'\alpha'}}{\sqrt{M_{s'}}} \right)^*. \end{aligned} \quad (\text{A26})$$

In the hypothesis that exchange-correlation effects are negligible, using the Poisson equation we obtain an equivalent formula

$$\mathbf{e}_{\text{LOq}} \mathcal{D}^L(\mathbf{q}) \mathbf{e}_{\text{LOq}}^* = \frac{A}{v_{\text{BN,BN}}^{00}(\mathbf{q})} \int f_{\text{BN}}^0(z) \bar{V}_{\text{LO}}(\mathbf{q}, z) dz \times \int f_{\text{BN}}^0(z) V_{\text{LO}}^*(\mathbf{q}, z) dz. \quad (\text{A27})$$

In the above equation we have used the abbreviation $\bar{V}_{\text{LO}}(\mathbf{q}, z) = \sum_{s,\alpha} \frac{e_{\text{LOq}}^{\alpha}}{\sqrt{M_s}} \frac{\partial \bar{V}_{\text{KS}}(\mathbf{q}, z)}{\partial u_{s,\alpha}^q}$, which is the projection on the LO mode of $\frac{\partial \bar{V}_{\text{KS}}(\mathbf{q}, z)}{\partial \mathbf{u}_q^q}$ (and the same for nonbarred potential; ‘‘KS’’ indicates the Khon-Sham potential). \bar{V}_{LO} is computed in this work as explained in Ref. [65]. The approximation of Eq. (A27) can be bettered assuming that the difference between longitudinal and transverse optical phonon frequencies is all attributable to the long-range component of the dynamical matrix—i.e., short range interactions differences between LO and TO are negligible. This amounts to writing

$$\mathbf{e}_{\text{LOq}} \mathcal{D}^L(\mathbf{q}) \mathbf{e}_{\text{LOq}}^* = \hbar^2 \omega_{\text{LOq}}^2 - \hbar^2 \omega_{\text{TOq}}^2, \quad (\text{A28})$$

as it is customarily done, e.g., for 3D cases. This is the same approximation included in Eq. (30) in the isotropic case. The difference between using Eqs. (A28) and (A27) is commented in Appendix B.

Inserting Eq. (A28) into Eq. (A22), we end up with

$$[\epsilon_{\text{IL,ph}}^{-1}]^0(\mathbf{q}, \omega) = [\epsilon_{\text{IL,el}}^{-1}]^0(\mathbf{q}) \frac{\hbar^2 \omega_{\text{LOq}}^2 - \hbar^2 \omega_{\text{TOq}}^2}{(\hbar\omega + i\hbar\eta_{\text{LO}})^2 - \hbar^2 \omega_{\text{LOq}}^2}, \quad (\text{A29})$$

which in the isotropic case directly leads to Eq. (32). If both the positive and negative phonon spectral functions are very sharp, then for positive frequencies we have

$$-\text{Im}[\epsilon_{\text{IL,ph}}^{-1}]^0(\mathbf{q}, \omega) \underset{\omega \sim \omega_{\text{LOq}}}{\sim} \pi [\epsilon_{\text{IL,el}}^{-1}]^0(\mathbf{q}) \frac{\hbar^2 \omega_{\text{LOq}}^2 - \hbar^2 \omega_{\text{TOq}}^2}{2\hbar\omega_{\text{LOq}}} \times \delta(\hbar\omega - \hbar\omega_{\text{LOq}}). \quad (\text{A30})$$

In the above derivations we have always treated the phonon system in the clean limit; this hypothesis may be lifted by dressing the phonon propagator with the appropriate self-energies, also with the inclusion of phonon-phonon interactions. This treatment goes beyond the scopes of this work. Here, we simplify the treatment by using for η a finite constant value compatible with experimental observations, i.e., η_{LO} .

c. Rewriting atomic-mediated screened Coulomb as a function of electron-phonon in the static case

In the same approximations of Appendixes A 2 a and A 2 b, Eq. (A17) can be rewritten in an interesting fashion for the static case via the Frölich electron-phonon coupling stripped of the Bloch functions overlaps. In fact, using Eq. (36) of

Ref. [65] we define

$$g_{\text{LOq}}^{\text{Fr}} = \frac{i}{A} w_{\text{el}}(\mathbf{q}) \sum_{s\alpha\beta} q_\beta \bar{Z}_{s\beta\alpha} e_{\text{LOq}}^{s\alpha} \times \left(\frac{\hbar}{2M_s \omega_{\text{LOq}}} \right)^{1/2}. \quad (\text{A31})$$

Equation (A17) then becomes

$$w_{\text{ph}}(\mathbf{q}, \omega) = A |g_{\text{LOq}}^{\text{Fr}}|^2 \frac{2\hbar\omega_{\text{LOq}}}{(\hbar\omega + i\hbar\eta_{\text{LO}})^2 - \hbar^2 \omega_{\text{LOq}}^2}, \quad (\text{A32})$$

with

$$-\text{Im}[w_{\text{ph}}(\mathbf{q}, \omega)] \underset{\omega \sim \omega_{\text{LOq}}}{\sim} \pi A |g_{\text{LOq}}^{\text{Fr}}|^2 \delta(\hbar\omega - \hbar\omega_{\text{LOq}}). \quad (\text{A33})$$

This means that the weight of the poles of $w_{\text{ph}}(\mathbf{q}, \omega_{\text{LO}})$ is proportional to the squared modulus of the Frölich coupling.

In the general case where the static approximation for the electronic screening cannot be performed, the imaginary part of the screened Coulomb interaction will contain both electron-electron and electron-phonon contributes. The interplay of the electronic system and the phononic one determines the dispersion of plasmon and phonon poles, and their coupling.

3. Scattering rates and g^2

The scattering rate τ^{-1} of electrons relates to the retarded electronic self-energy as

$$-\text{Im}\Sigma_{\text{el}} = \frac{\hbar}{2} \tau^{-1}. \quad (\text{A34})$$

Following Refs. [23] and [27], one can deduce the depopulation rate of electrons, i.e., scattering times, using the structure factor and the fluctuation-dissipation theorem, obtaining an expression proportional to $-\text{Im}[\epsilon^{-1}(\mathbf{q})]v(\mathbf{q})$. We generalize such 3D expressions to the 2D case. We take into account the matricial ordering of the inverse dielectric matrix and Coulomb kernel (not relevant in the purely 3D case) by noting that the electronic self-energy reads [125]

$$\Sigma_{\text{el}}(12) = i\hbar \int d(34)G(13)\Gamma(324)w(41^+). \quad (\text{A35})$$

The scattering rate for a Bloch electron $n\mathbf{k}$ is then obtained as

$$k_{\text{B}}T \frac{\partial f_{n\mathbf{k}}}{\partial \epsilon_{n\mathbf{k}}} \tau_{n\mathbf{k}}^{-1} = \frac{2\pi}{\hbar} \frac{1}{AN_{\mathbf{q}}} \sum_{\mathbf{q}} \int_{-\infty}^{\infty} d\omega \int d\mathbf{r} d\mathbf{z} d\mathbf{r}' d\mathbf{z}' d\bar{z} \times n_{\epsilon_{n\mathbf{k}}}^{\text{FD}} (1 - n_{\epsilon_{n\mathbf{k}+\mathbf{q}}}^{\text{FD}}) (1 + n_{\omega}^{\text{BE}}) \times u_{n\mathbf{k}}^*(\mathbf{r}, z) u_{n\mathbf{k}}(\mathbf{r}', z') u_{m\mathbf{k}+\mathbf{q}}(\mathbf{r}, z) u_{m\mathbf{k}+\mathbf{q}}^*(\mathbf{r}', z') \times \text{Im} \left[-\epsilon^{-1}(\mathbf{q}, z, \bar{z}, \omega) \frac{v(\mathbf{q}, \bar{z}, z')}{\pi} \right] \times \delta(\hbar\omega + \epsilon_{m\mathbf{k}+\mathbf{q}} - \epsilon_{n\mathbf{k}}), \quad (\text{A36})$$

where we have assumed that final states are represented by noninteracting electrons. Depending on the derivation, the overlap factor comes from bringing the self-energy in the basis of the Bloch basis functions, and taking its diagonal components (see, e.g., Eq. (157) of Ref. [125]), or from the connection between the scattering rate and the structure factor (see, e.g., Eq. (5) of Ref. [23]). The integral over positive frequencies will produce the scattering due to phonon/plasmon

emission, while the one over negative frequencies is related to absorption because $1 + n_{-\omega}^{\text{BE}} = -n_{\omega}^{\text{BE}}$, where the minus sign is compensated by the property (A2) applied on the inverse dielectric matrix. To connect with usual formulas, by using the algebraic relations discussed in the Supplemental Material of Ref. [40], one finds

$$\begin{aligned} \tau_{nk}^{-1} &= \frac{2\pi}{\hbar} \frac{1}{AN_{\mathbf{q}}} \sum_{\mathbf{q}} \int_{-\infty}^{\infty} d\omega \int d\mathbf{r} d\mathbf{z} d\mathbf{r}' d\mathbf{z}' d\bar{z} \text{sign}(\omega) \mathcal{A}(\omega) \\ &\times u_{nk}^*(\mathbf{r}, z) u_{nk}(\mathbf{r}', z') u_{m\mathbf{k}+\mathbf{q}}(\mathbf{r}, z) u_{m\mathbf{k}+\mathbf{q}}^*(\mathbf{r}', z') \\ &\times \text{Im} \left[-\epsilon^{-1}(\mathbf{q}, z, \bar{z}, \omega) \frac{v(\mathbf{q}, \bar{z}, z')}{\pi} \right] \\ &\times \delta(\hbar\omega + \varepsilon_{m\mathbf{k}+\mathbf{q}} - \varepsilon_{nk}), \\ \mathcal{A}(\omega) &= \left[n_{\omega}^{\text{BE}} + \frac{1}{2} + \text{sign}(\omega) \frac{1}{2} - \text{sign}(\omega) n_{\varepsilon_{m\mathbf{k}+\mathbf{q}}}^{\text{FD}} \right]. \end{aligned} \quad (\text{A37})$$

In the dual basis set used in this work we have

$$\begin{aligned} \int d\bar{z} \epsilon^{-1}(\mathbf{q}, z, \bar{z}, \omega) v(\mathbf{q}, \bar{z}, z') &= \sum_{\substack{i'j' \\ kk'l'l}} \phi_k^i(z) v_{kk'}^{i'j'}(\mathbf{q}) \chi_{k'l'}^{j'j} \\ &\times (\mathbf{q}, \omega) v_{l'l}^{j'j} \phi_l^j(z'). \end{aligned} \quad (\text{A38})$$

In the scattering rate expression we have pairs of cell-periodic Bloch functions which are building blocks for the density, which gets coherently bracketed with the basis set of Eq. (4). In fact, Eq. (A37) becomes

$$\begin{aligned} \tau_{nk}^{-1} &= \sum_{\substack{i'j' \\ kk'l'l}} \frac{2\pi}{\hbar} \frac{1}{AN_{\mathbf{q}}} \sum_{\mathbf{q}} \int_{-\infty}^{\infty} d\omega \langle u_{nk} | \phi_k^i | u_{m\mathbf{k}+\mathbf{q}} \rangle \\ &\times \langle u_{m\mathbf{k}+\mathbf{q}} | \phi_l^j | u_{nk} \rangle \text{sign}(\omega) \mathcal{A}(\omega) \\ &\times \text{Im} \left[-\frac{1}{\pi} v_{kk'}^{i'j'}(\mathbf{q}) \chi_{k'l'}^{j'j}(\mathbf{q}, \omega) v_{l'l}^{j'j}(\mathbf{q}) \right] \\ &\times \delta(\hbar\omega + \varepsilon_{m\mathbf{k}+\mathbf{q}} - \varepsilon_{nk}). \end{aligned} \quad (\text{A39})$$

a. BN single layer in the static case: Electron-phonon

The scattering rate due to electron-phonon coupling for a BN single layer is obtained by using that the density-density response function is of the form of Eq. (12), where the atomic-mediated contribution to the response is obtained from Eqs. (A22) and (A24). Due to in-plane mirror symmetry, the unperturbed Bloch wave functions are even with respect to the layer position, so that in Eq. (A39) one has the selection rule $i = j = 0$. The scattering rate may then be written as

$$\begin{aligned} \tau_{nk}^{-1, \text{LO}} &= \frac{1}{A} \frac{2\pi}{\hbar} \int_{-\infty}^{\infty} \hbar d\omega |\langle u_{nk} | u_{m\mathbf{k}+\mathbf{q}} \rangle|^2 \text{sign}(\omega) \mathcal{A}(\omega) \\ &\times \text{Im} \left[-\left[\epsilon_{\text{IL,ph}}^{-1} \right]^0(\mathbf{q}, \omega) \frac{v_{\text{BN,BN}}^{00}(\mathbf{q})}{\pi} \right] \\ &\times \delta(\hbar\omega + \varepsilon_{m\mathbf{k}+\mathbf{q}} - \varepsilon_{nk}), \end{aligned} \quad (\text{A40})$$

which using Eqs. (A32) and (A5) becomes the standard expression

$$\begin{aligned} \tau_{nk}^{-1, \text{LO}} &= \frac{2\pi}{\hbar} \frac{1}{N_{\mathbf{q}}} \sum_{\mathbf{q}} |\delta_{\text{LOq}}^{\text{Fr}}|^2 |\langle u_{nk} | u_{m\mathbf{k}+\mathbf{q}} \rangle|^2 \\ &\times \left[(1 + n_{\omega_{\text{LOq}}}^{\text{BE}} - n_{\varepsilon_{m\mathbf{k}+\mathbf{q}}}^{\text{FD}}) \delta(\hbar\omega_{\text{LOq}} + \varepsilon_{m\mathbf{k}+\mathbf{q}} - \varepsilon_{nk}) \right. \\ &\left. + (n_{\omega_{\text{LOq}}}^{\text{BE}} + n_{\varepsilon_{m\mathbf{k}+\mathbf{q}}}^{\text{FD}}) \delta(-\hbar\omega_{\text{LOq}} + \varepsilon_{m\mathbf{k}+\mathbf{q}} - \varepsilon_{nk}) \right]. \end{aligned} \quad (\text{A41})$$

b. Heterostructures

In general, one can express the imaginary part of the screened Coulomb as a squared modulus times a δ (with a minus sign), i.e., as in Eq. (A33), only when one electronic dielectric function can be treated as static. In the heterostructures studied in this work, this is not always the case, due to the coupling of plasmons and phonons. Nevertheless, there exist limits where one can use $w_{\text{el}}(\mathbf{q}, \omega) \sim w_{\text{el}}(\mathbf{q}, 0)$. They correspond to the cases where the coupling is screened statically by graphene and BN (large $|\mathbf{q}|$ limit), or just by BN (small $|\mathbf{q}|$ limit). Only in these asymptotic limits, decoupling the electron-phonon and electron-plasmon contribution to the total coupling is not ambiguous. For example, one could determine a screened electron-phonon coupling directly using $\epsilon_{\text{el}}^{-1}$ [126]. The same conclusions can be obtained looking at the electronic contribution to the screened Coulomb kernel, for a system without atomic polarization. In that case, one finds that the pole residue is related to the electron-plasmon coupling [127].

The general expression Eq. (A39) can nevertheless be simplified in some situations. Bloch overlaps are important to understand selection rules and the localization of the indexes k and l . If, e.g., a Bloch electron is delocalized in the out-of-plane direction over the whole structure, such as in the case of a purely BN heterostructure, then brackets with $k \neq l$ are all relevant. If instead we are interested in the electron-phonon coupling between graphene's Bloch electrons, which are localized on the graphene's plane, then we must have $k = l = \text{Gr}$, since the overlap vanish for the other cases. Moreover, as done for the single layer, we still assume the unperturbed Bloch wave functions are even with respect to the layer position, so that in Eq. (A39) one has $i = j = 0$. The result of this operation is

$$\begin{aligned} \tau_{nk}^{-1} &= \frac{2\pi}{\hbar} \frac{1}{AN_{\mathbf{q}}} \sum_{\mathbf{q}} \sum_{\substack{i'j' \\ kk'l'l}} \langle u_{nk} | \phi_k^0 | u_{m\mathbf{k}+\mathbf{q}} \rangle \langle u_{m\mathbf{k}+\mathbf{q}} | \phi_l^0 | u_{nk} \rangle \\ &\times \int_{-\infty}^{\infty} d\omega \text{sign}(\omega) \mathcal{A}(\omega) \text{Im} \\ &\times \left[-\frac{1}{\pi} v_{kk'}^{0i'}(\mathbf{q}) \chi_{k'l'}^{i'j'}(\mathbf{q}, \omega) v_{l'l}^{j'0}(\mathbf{q}) \right] \\ &\times \delta(\hbar\omega + \varepsilon_{m\mathbf{k}+\mathbf{q}} - \varepsilon_{nk}). \end{aligned} \quad (\text{A42})$$

In the above expression, in the asymptotic limits where we can decouple the electron-phonon from the electron-electron interaction, $-\text{Im}v\chi v$ reduces to the squared modulus of the electron-phonon coupling. Motivated by this observation, we

recast the above expression with the following notation:

$$\begin{aligned} \tau_{nk}^{-1} &= \frac{2\pi}{\hbar} \frac{1}{N_{\mathbf{q}}} \sum_{\mathbf{q}} \int_{-\infty}^{\infty} d\omega \mathcal{A}(\omega) \delta(\hbar\omega + \varepsilon_{m\mathbf{k}+\mathbf{q}} - \varepsilon_{nk}) \\ &\times \sum_{kl} \langle u_{nk} | \phi_k^0 | u_{m\mathbf{k}+\mathbf{q}} \rangle \langle u_{m\mathbf{k}+\mathbf{q}} | \phi_l^0 | u_{nk} \rangle g_{kl}^2(\mathbf{q}, \omega), \end{aligned} \quad (\text{A43})$$

where $g_{kl}^2(\mathbf{q}, \omega)$ is given by Eq. (42).

4. Practical expression for the remote phonon transport scattering rates

Equation (A39) is the most general expression for the scattering rate of a heterostructure. Neglecting the scalar product of Bloch functions with ϕ^1 , one obtains Eq. (A43).

Here, we are interested in the scattering rates where the initial and final states are electrons of graphene, and the scattering is mediated by remote phonons. In the Dirac cone approximation, we take \mathbf{k} to be a vector around \mathbf{K} . Without loss of generality due to isotropy, we consider a \mathbf{k} on the horizontal axis, as depicted in Fig. 15. In Fig. 15 we consider initial electrons belonging to isosurface ε . We then define the θ angle as the scattering angle between \mathbf{k} and $\mathbf{k} + \mathbf{q}$, i.e., $\theta = \theta(\mathbf{q})$. The transport scattering time due to remote phonon scattering is then obtained as

$$\begin{aligned} \tau_{nk}^{\text{tr},-1} &= \frac{2\pi}{\hbar} \frac{1}{N_{\mathbf{q}}} \sum_{\mathbf{q}} \int_{-\infty}^{\infty} d\omega \mathcal{A}(\omega) \delta(\hbar\omega + \varepsilon_{m\mathbf{k}+\mathbf{q}} - \varepsilon_{nk}) \\ &\times \sum_{kl} \langle u_{nk} | \phi_k^0 | u_{m\mathbf{k}+\mathbf{q}} \rangle \langle u_{m\mathbf{k}+\mathbf{q}} | \phi_l^0 | u_{nk} \rangle g_{\text{Gr}}^{2,\text{ph}}(\mathbf{q}, \omega) \\ &\times [1 - \cos \theta(\mathbf{q})], \end{aligned} \quad (\text{A44})$$

where $g_{\text{Gr}}^{2,\text{ph}}$ is defined by Eq. (51). To have more manageable expressions, we now approximate the phonon frequency to be dispersionless, i.e., we assume that $g_{\text{Gr}}^{2,\text{ph}}$ is peaked at $\omega = \pm\omega_{\text{ph}}$ and approximate

$$g_{\text{Gr}}^{2,\text{ph}}(\mathbf{q}, \omega) \sim \bar{g}_{\text{Gr}}^{2,\text{ph}}(q) \delta(\omega \pm \omega_{\text{ph}}). \quad (\text{A45})$$

We recall that the above coupling is of long-range nature, and it is in very good approximation isotropic, as we used in the right-hand side of the equation. Given this coupling, if we consider the special case $\varepsilon = \varepsilon_{\text{F}}$ the two energy conserving Dirac δ functions of Eq. (A44) (for positive and negative frequencies, i.e., emission of absorption) imply that $\mathbf{k} + \mathbf{q}$ lies on the isoenergetic lines $|\varepsilon_{\text{F}} \pm \hbar\omega_{\text{ph}}|$. As presented in Fig. 15 for an absorption process, q and θ are now related geometrically, i.e., we can write q_{θ} . Since for a given θ we have two different values of q for emission and absorption, we will call them q_{θ}^{\pm} , respectively. They respect the following relations:

$$q_{\theta=0}^{\pm} \leq q_{\theta}^{\pm} \leq q_{\theta=\pi}^{\pm}, \quad (\text{A46})$$

$$\frac{q_{\theta=0}^{\pm}}{k_{\text{F}}} = \frac{||\varepsilon_{\text{F}} \pm \hbar\omega_{\text{ph}}| - |\varepsilon_{\text{F}}||}{|\varepsilon_{\text{F}}|}, \quad (\text{A47})$$

$$\frac{q_{\theta=\pi}^{\pm}}{k_{\text{F}}} = \frac{||\varepsilon_{\text{F}}| + |\varepsilon_{\text{F}} \pm \hbar\omega_{\text{ph}}||}{|\varepsilon_{\text{F}}|}. \quad (\text{A48})$$

Now, the sum over \mathbf{q} can then be transformed in just an angular integration, keeping in mind that the volume element

$q dq$ will bring a factor $|\varepsilon_{\text{F}} \pm \omega_{\text{ph}}|$. The Bloch overlaps of graphene can be written in the form given below Eq. (26). With algebraic rewriting of the statistical occupation factors, at last we obtain Eq. (54), if we choose $\omega_{\text{ph}} = \omega_{\text{BN}}$.

APPENDIX B: COMPUTATIONAL DETAILS

In this Appendix we detail the numerical computation of the ingredients of the VED method.

1. DFT calculations

DFT and DFPT calculations of ground states, dielectric responses and phonons are carried out with the QUANTUM ESPRESSO package [128,129], with 2D boundary conditions [130], and optimized norm-conserving Vanderbilt pseudopotentials [131] from the pseudo-DOJO library [132].

a. Single-layer static electronic response from DFPT

The parametrization of single-layer static electronic responses is detailed in Ref. [19]. In the framework of DFPT, the layer is perturbed with a monochromatic in-plane periodic function of the form $V^i(q, z) = V_0 \phi^i$. The density response ρ^i is extracted from DFPT, renormalized by V_0 and integrated to obtain $Q^i(q)$. Examples of plots of $Q^i(q)$ can be found in Fig. 9 of Ref. [19]. The profile function is then defined as $\rho^i(q, z)/Q^i(q)$. A small q -dependence of the profile function exists in practice, but has a small impact on the observables.

b. In-plane contribution to atomic response

Here we discuss the calculation of $\mathbf{e}_{\text{LO}q} \mathcal{D}^{\text{L}}(q) \mathbf{e}_{\text{LO}q}^*$ from DFPT, and in particular two possible approximations mentioned above: Eqs. (A27) and (30). In Eq. (A27) the potential is computed using a procedure similar to Ref. [65]—an exact procedure may be developed following Ref. [60], but we leave it for further developments. As anticipated in the main text, this assumes that the LO potentials are generated by a charge density with the same profile as the electronic response f_{BN}^0 . In practice that is not exactly true. Instead, we expect that using Eq. (A27), as done in this work, is a better approximation. In any case, we find that the difference of implementing Eq. (A27) instead of Eq. (30) is on the order of 5% at the largest momenta considered here.

2. Neglect of out-of-plane atomic contribution

An upper limit estimation of the atomic contribution to Eq. (24) in the long wavelength limit is given by

$$Q_{\text{ph}}^1(q, \omega) \sim \frac{1}{AM^*} \frac{|Z^{\perp}|^2}{(\omega + i\eta_{\text{ZO}})^2 - \omega_{\text{ZO}}^2}, \quad (\text{B1})$$

where M^* is the reduced mass, we have neglected the wave-vector dependence of the phonon frequency $\omega_{\text{ZO}} \sim 800\text{cm}^{-1}$, and $|Z^{\perp}| = 0.245$ is the absolute value of the Born effective charges of BN as computed from DFPT calculations performed at $q = 0$. With respect to the expression for the in-plane atomic response Eq. (32), in Eq. (B1) we have approximated the out-of-plane dielectric function to unity, thus expecting an overestimation of $Q_{\text{ph}}^1(q, \omega)$, in line with what discussed in the previous section in Fig. 19. The smearing

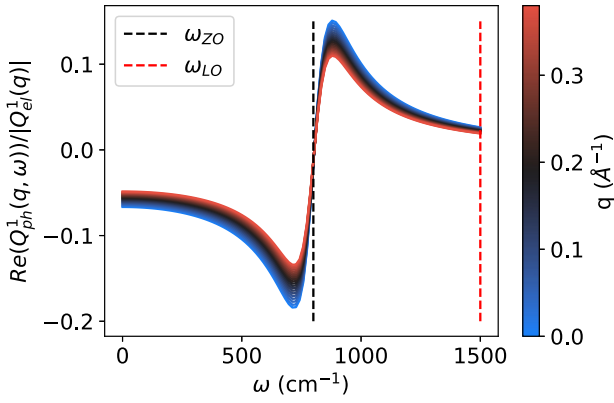


FIG. 16. $\text{Re}(Q_{\text{ph}}^1(q, \omega))/|Q_{\text{el}}^1(q)|$ as a function of ω , for the wave vectors relevant for this work. For the ZO mode at $\sim 800\text{cm}^{-1}$ (black line), $\eta_{\text{ZO}} \sim 80\text{cm}^{-1}$ is employed for representation purposes, the values at $\omega = \omega_{\text{LO}}$ (red line) not being influenced by this choice. We notice that the estimated upper limit of the ratio between the atomic and electronic contribution reaches a small value of $\sim 5\%$ at $\omega = \omega_{\text{LO}}$.

is taken as at an unphysical value of $\eta_{\text{ZO}} \sim 80\text{cm}^{-1}$, for representation aims. In Fig. 16 we plot the real part of the ratio $Q_{\text{ph}}^1(q, \omega)/|Q_{\text{el}}^1(q)|$.

As seen from the plot, Eq. (B1) has a 5% influence on the total value of Q^1 at $\omega = \omega_{\text{LO}}$ (vertical red line), meaning Eq. (24) is a good approximation for the BN single layer. Nevertheless, contributions may add up when adding several layers in a vdWH, i.e., going towards the hexagonal bulk limit. Even in this case though, the atomic contribution to Q_{ph}^1 is negligible. In fact, we can write

$$\epsilon_0^{zz} = \epsilon_{\infty}^{zz} + \frac{4\pi e^2}{V} \frac{|Z^{zz}|^2}{M^* \omega_{\text{ZO}}^2}, \quad (\text{B2})$$

where $|Z^{zz}| = 0.76$ and $\epsilon_{\infty}^{zz} = 2.729$ as from DFPT calculations at zone centers, concluding that $(\epsilon_0^{zz} - \epsilon_{\infty}^{zz})/\epsilon_{\infty}^{zz} \sim 7\%$. Even in this case, the effect of the ZO degrees of freedom is small on the total value of the dielectric function. Since the ZO phonon frequency is roughly equidistant from $\omega = 0$ and ω_{LO} , the approximation of Eq. (24) remains good for the determination of LO dispersions even when stacking multiple BN layers.

APPENDIX C: COMPARISON OF DIFFERENT MODEL

1. VED versus EDC

Electrodynamic continuum (EDC) models to study polaritons are based on the transfer matrix method [133]. The various components of the heterostructure are considered as uniform slabs of dielectric or metallic materials. They are used in most experimental studies of phonon-polaritons [13,20,55,134]. Here, we consider a heterostructure made of 5 BN, with each layer being of thickness $d = 3.3\text{\AA}$. The full heterostructure of thickness $D = 5d$ is suspended in air having a dielectric constant $\epsilon_a = 1$. In Fig. 3 we compare our LO phonon dispersion curves with the polariton dispersions for the in-plane modes found in Ref. [20]. These are determined

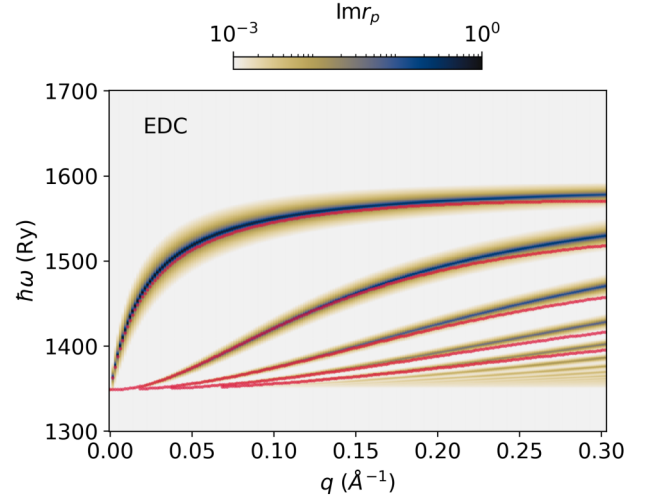


FIG. 17. Dispersions of the electrodynamic excitations in five layers of BN, obtained as the normalized peaks of the imaginary part of the complex reflectivity, according to the EDC model solved with the transfer matrix method. For comparison, we also plot in red the dispersions of the polar optical phonons obtained via the VED model.

by the peak of the imaginary part of the complex reflectivity r_p , given by

$$r_p = r_a \frac{1 + e^{i2k_z^z d}}{1 + r_a^2 e^{i2k_z^z D}}, \quad (\text{C1})$$

$$r_a = \frac{\epsilon_{\parallel} k_a^z - \epsilon_a k_e^z}{\epsilon_{\parallel} k_a^z + \epsilon_a k_e^z}. \quad (\text{C2})$$

In the above equations all the (q, ω) dependencies have been left implicit. ϵ_{\parallel} is the BN bulk dielectric constant in the plane perpendicular to the c axis, while ϵ_{\perp} is the one along the c axis. k^z are the z component of the photon's momentum:

$$k_e^z = \sqrt{\epsilon_{\parallel} \frac{\omega^2}{c^2} - \frac{\epsilon_{\parallel}}{\epsilon_z} q^2}, \quad k_a^z = \sqrt{\epsilon_a \frac{\omega^2}{c^2} - q^2}. \quad (\text{C3})$$

Neglecting the terms in ω/c , one simply has

$$k_a^z = iq, \quad k_e^z = iq \sqrt{\frac{\epsilon_{\parallel}}{\epsilon_{\perp}}}. \quad (\text{C4})$$

Finally, ϵ_{\parallel} can be expressed as

$$\epsilon_{\parallel} = \epsilon_{\parallel}^{\infty} \left(1 + \frac{\omega_{\text{LO}}^2 - \omega_{\text{TO}}^2}{\omega_{\text{TO}}^2 - (\omega + i\eta_{\text{LO}})^2} \right), \quad (\text{C5})$$

where all the parameters are intended as the BN bulk ones. For a fair comparison, we evaluate them in the same first-principles framework as our calculations, i.e., we use $\omega_{\text{LO}} = 1590\text{cm}^{-1}$ and $\omega_{\text{TO}} = 1348\text{cm}^{-1}$ and $\epsilon_{\parallel}^{\infty} = 4.98$.

It is evident from Fig. 17 that the VED and the highest 5 EDC dispersions agree in an excellent way. Moreover, while not reported here, we checked that the same agreement is found for heterostructures of BN/Gr/BN.

a. Identification of EDC polaritons and VED excitations

Let us consider an in-plane isotropic monolayer system with planar conductivity σ , suspended in vacuum, and

with negligible out-of-plane size. Then, for a transverse magnetic (TM) electromagnetic wave propagating inside a two-dimensional dielectric/metallic plane, the boundary conditions lead to the following form for the dispersion relation [8]:

$$q = \frac{2i\omega\epsilon_0}{\sigma(q, \omega)}. \quad (\text{C6})$$

At the same time, for two-dimensional systems in the long-wavelength limit it holds that [135,136]

$$\epsilon(q, \omega) = 1 + i \frac{\sigma(q, \omega)q}{2\epsilon_0\omega}. \quad (\text{C7})$$

It is clear that the curves that satisfy Eq. (C6) also display $\epsilon(q, \omega) = 0$ due to Eq. (C7), i.e., they are the divergences of $\text{Im}\epsilon^{-1}(q, \omega)$ or, in other words, the peaks of $\text{Im}\chi(q, \omega)$. We remind that this is not the case for three-dimensional materials, where, e.g., a LO phonon is associated with only a longitudinal propagating electric field with null magnetic field, and therefore a null Poynting vector. Of course, the above considerations are valid once an effective sheet conductivity $\sigma(q, \omega)$ can be identified; for EDC, it can be determined from r_p , while from VED it can be obtained directly via $\text{Im}\epsilon^{-1}(q, \omega)$, and as confirmed by Fig. 17 they are expected to display the same electrodynamic excitations.

2. VED and QEH

To compare with the Quantum ELectrostatic Heterostructures (QEH) model [29], we use the QEH parametrization of the response function for single-layer BN, based on zone center quantities, and insert it in the VED model. In particular, we define the following irreducible response function for the phonons:

$$\chi_{\text{ph}}^{\text{irr}}(q, \omega) = \frac{q}{2\pi e^2} \frac{S_{\Gamma} q}{(\hbar\omega + i\hbar\eta_{\text{LO}})^2 - \hbar^2\omega_{\text{TO}}^2}, \quad (\text{C8})$$

$$S_{\Gamma} = \lim_{q \rightarrow 0} \frac{\mathbf{e}_{\text{LO}q} \mathcal{D}^{\text{L}}(\mathbf{q}) \mathbf{e}_{\text{LO}q}^*}{q}, \quad (\text{C9})$$

where one can recognize S_{Γ} as the slope of the LO dispersion for $q \rightarrow 0$ and the inverse of the coulomb kernel without form-factor $2\pi e^2/q$. The irreducible response function of the electronic contribution is written

$$\chi_{\text{el}}^{\text{irr}}(q, \omega) = \frac{1}{1 + \frac{2\pi e^2}{q} Q_{\text{BN,el}}^0}, \quad (\text{C10})$$

and added to the phonon contribution to get

$$Q_{\text{BN}}^0(q, \omega) = \frac{1}{1 - \frac{2\pi e^2}{q} (\chi_{\text{el}}^{\text{irr}} + \chi_{\text{ph}}^{\text{irr}})}, \quad (\text{C11})$$

always using the simple Coulomb kernel $2\pi e^2/q$. Figure 18 shows an excellent agreement for the top branch in the $q \rightarrow 0$ limit, but a clear disagreement starting from $q = 0.1 \text{ \AA}^{-1}$ and for the lower branches in general.

Figure 19 shows the comparison between VED and QEH for the electron-phonon coupling in single-layer BN. It further reveals that the main discrepancy, at least in the case of BN, comes from the form factors $F_{\text{BN,BN}}^{00}$.

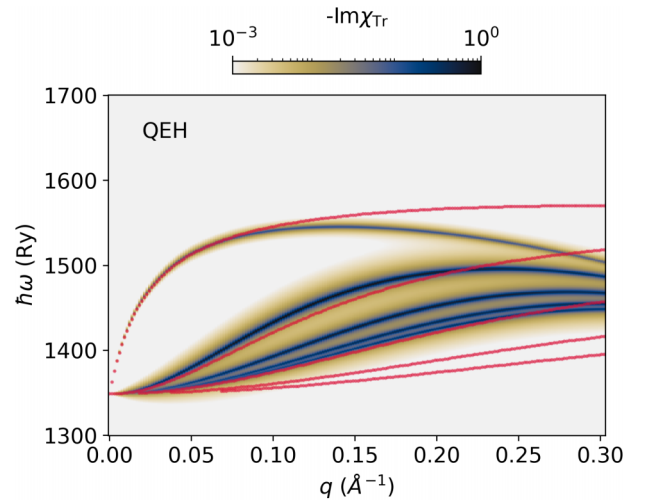


FIG. 18. Dispersion of the electrodynamic modes due to longitudinal polar optical phonons in five layers of BN according to QEH [29]. For comparison, we also plot in red the dispersion obtained in the VED model.

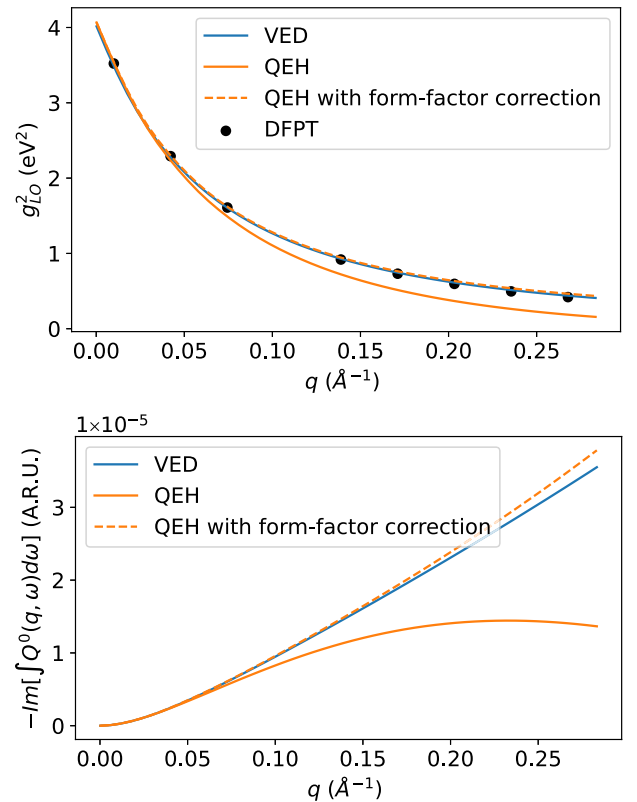


FIG. 19. (Top) Comparison of \bar{g}^2 in single-layer BN, obtained via the VED model and the QEH model of Ref. [29], reducing to the LO phonon coupling. The discrepancy is attributed to the different evaluation of $-\text{Im}[\int_0^\infty Q^0(q, \omega)d\omega]$ (Bottom). Notice that the QEH error is up to 38% at the largest value of q with respect to DFPT values, that are on top of the results of this work. There main source of error is the use, in the QEH method, of the strictly 2D Coulomb kernel $\frac{2\pi}{q}$ rather than the more appropriate $v_{\text{BN,BN}}^{00}$ to deduce the interacting response function $Q^0(q, \omega)$ from the irreducible response functions of electrons and phonons. Correcting this error, the QEH methodology is very near to our results.

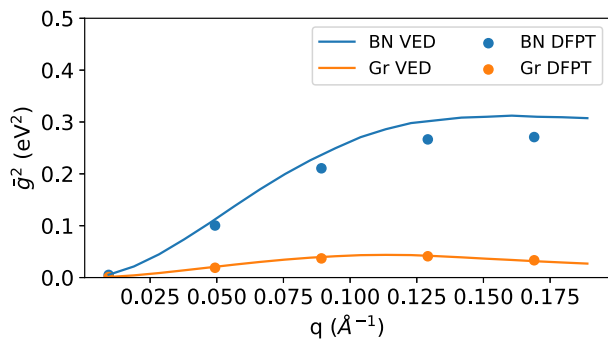


FIG. 20. Comparison of electron-phonon coupling matrix elements in VED (\bar{g}_{Gr}^2 and \bar{g}_{BN}^2) and DFPT results in BN/Gr. In the VED method, the static limit of graphene's electronic response is used, so that the coupling is only of electron-phonon type.

APPENDIX D: COMPARISON OF SCREENED ELECTRON-PHONON COUPLING IN VED AND DFPT

When considering only the static limit of electronic responses, the VED method reproduces electron-phonon interactions obtained in DFPT calculations in the Born-Oppenheimer approximation. The g coupling is extracted from DFPT for a given mode μ on layer k as

$$g_{\mu,k}^{\text{DFPT}}(\mathbf{q}) = \left| \int dz f_k(z) V_{\mu}(\mathbf{q}, z) \right|, \quad (\text{D1})$$

where $\bar{V}_{\mu}(\mathbf{q}, z) = \sum_s \frac{e_{\mu\mathbf{q}}^s}{\sqrt{M_s}} \cdot \frac{\partial V_{\text{KS}}(\mathbf{q}, z)}{\partial \mathbf{u}_{\mathbf{q}}^s}$. In the above expression we can take the modulus because the coupling is always positive. From a practical point of view, it is implemented to remove the phase uncertainty of the phonon polarization vectors coming out from first-principles calculations. Notice that in DFPT the perturbation is explicitly inserted in the system via a displacement of the atoms, therefore we

cannot choose the layer on which the external perturbation is applied. This is the reason why Eq. (D1) presents only one layer index, that is treated as the first index (probe index) of g_{kl}^2 .

In this section, we consider a simple system made of BN and graphene. Ground state DFT calculations are performed with a nonuniform grid of momenta to properly sample the small Fermi surface of graphene and be able to use a electronic smearing corresponding to the Fermi-Dirac distribution at room temperature. The nonuniform grid varies from 12×12 to the equivalent of 196×196 around the Fermi surface. Graphene is doped with an extra density of electrons $n = 10^{13} \text{ cm}^{-2}$, corresponding to a Fermi level $\sim 0.3 \text{ eV}$. Phonons are simulated at five momenta in the Γ -M direction. We then select the electron-phonon coupling coming from the (only) LO mode of BN.

To compute the comparable quantity in the VED method, we use the static limit of the electronic response of graphene's electrons, computed directly in the single-layer graphene's system with the same parameters as the BN/Graphene system. We then compute $\bar{g}_{\text{Gr}}^2(q)$ and $\bar{g}_{\text{BN}}^2(q)$ from Eq. (48).

Figure 20 shows a good agreement between direct DFPT and the VED method for the main quantity of interest in this work $\bar{g}_{\text{Gr}}^2(q)$. Along with Fig. 9, this confirms that the VED method reproduces DFPT in the static limit of electronic responses even when metallic screening is present. A larger error is observed for $\bar{g}_{\text{BN}}^2(q)$ in this case, with respect to Fig. 9. This may be explained by the fact that the total effective potential, i.e., the potential generated by LO phonons and screened by electrons, displays much sharper variations in the out-of-plane direction due to the strong metallic screening from graphene. This would enhance errors related to the approximation of atomic profile functions with the electronic ones in the VED model.

- [1] A. Castellanos-Gomez, X. Duan, Z. Fei, H. R. Gutierrez, Y. Huang, X. Huang, J. Querada, Q. Qian, E. Sutter, and P. Sutter, Van der Waals heterostructures, *Nat. Rev. Methods Primers* **2**, 58 (2022).
- [2] K. S. Novoselov, A. Mishchenko, A. Carvalho, and A. H. Castro Neto, 2D materials and van der Waals heterostructures, *Science* **353**, aac9439 (2016).
- [3] Y. Liu, N. O. Weiss, X. Duan, H.-C. Cheng, Y. Huang, and X. Duan, Van der Waals heterostructures and devices, *Nat. Rev. Mater.* **1**, 16042 (2016).
- [4] L. V. Keldysh, A. A. Maradudin, and D. A. Kirzhnits, *The Dielectric Function of Condensed Systems* (Elsevier Science, Amsterdam, 2014).
- [5] P. Nozières and D. Pines, *Theory Of Quantum Liquids: Superfluid Bose Liquids* (Westview Press, New York, NY, 1999).
- [6] D. N. Basov, M. M. Fogler, and F. J. García De Abajo, Polaritons in van der Waals materials, *Science* **354**, aag1992 (2016).
- [7] T. Low, A. Chaves, J. D. Caldwell, A. Kumar, N. X. Fang, P. Avouris, T. F. Heinz, F. Guinea, L. Martin-Moreno, and F. Koppens, Polaritons in layered two-dimensional materials, *Nat. Mater.* **16**, 182 (2017).
- [8] N. Rivera, T. Christensen, and P. Narang, Phonon polaritonics in two-dimensional materials, *Nano Lett.* **19**, 2653 (2019).
- [9] J. Chen, M. Badioli, P. Alonso-González, S. Thongrattanasiri, F. Huth, J. Osmond, M. Spasenović, A. Centeno, A. Pesquera, P. Godignon, A. Zurutuza Elorza, N. Camara, F. J. G. De Abajo, R. Hillenbrand, and F. H. L. Koppens, Optical nano-imaging of gate-tunable graphene plasmons, *Nature (London)* **487**, 77 (2012).
- [10] Z. Fei, A. S. Rodin, G. O. Andreev, W. Bao, A. S. McLeod, M. Wagner, L. M. Zhang, Z. Zhao, M. Thiemens, G. Dominguez, M. M. Fogler, A. H. C. Neto, C. N. Lau, F. Keilmann, and D. N. Basov, Gate-tuning of graphene plasmons revealed by infrared nano-imaging, *Nature (London)* **487**, 82 (2012).
- [11] H. Yan, T. Low, W. Zhu, Y. Wu, M. Freitag, X. Li, F. Guinea, P. Avouris, and F. Xia, Damping pathways of mid-infrared plasmons in graphene nanostructures, *Nat. Photon.* **7**, 394 (2013).
- [12] V. W. Brar, M. S. Jang, M. Sherrott, S. Kim, J. J. Lopez, L. B. Kim, M. Choi, and H. Atwater, Hybrid surface-phonon-plasmon polariton modes in graphene/monolayer h-BN heterostructures, *Nano Lett.* **14**, 3876 (2014).

- [13] A. Woessner, M. B. Lundeberg, Y. Gao, A. Principi, P. Alonso-González, M. Carrega, K. Watanabe, T. Taniguchi, G. Vignale, M. Polini, J. Hone, R. Hillenbrand, and F. H. L. Koppens, Highly confined low-loss plasmons in graphene–boron nitride heterostructures, *Nat. Mater.* **14**, 421 (2015).
- [14] E. Yoxall, M. Schnell, A. Y. Nikitin, O. Txoperena, A. Woessner, M. B. Lundeberg, F. Casanova, L. E. Hueso, F. H. L. Koppens, and R. Hillenbrand, Direct observation of ultraslow hyperbolic polariton propagation with negative phase velocity, *Nat. Photon.* **9**, 674 (2015).
- [15] N. Li, X. Guo, X. Yang, R. Qi, T. Qiao, Y. Li, R. Shi, Y. Li, K. Liu, Z. Xu, L. Liu, F. J. García De Abajo, Q. Dai, E.-G. Wang, and P. Gao, Direct observation of highly confined phonon polaritons in suspended monolayer hexagonal boron nitride, *Nat. Mater.* **20**, 43 (2021).
- [16] M. Chen, Y. Zhong, E. Harris, J. Li, Z. Zheng, H. Chen, J.-S. Wu, P. Jarillo-Herrero, Q. Ma, J. H. Edgar, X. Lin, and S. Dai, Van der Waals isotope heterostructures for engineering phonon polariton dispersions, *Nat. Commun.* **14**, 4782 (2023).
- [17] K. J. Tielrooij, N. C. Hesp, A. Principi, M. B. Lundeberg, E. A. Pogna, L. Banszerus, Z. Mics, M. Massicotte, P. Schmidt, D. Davydovskaya, D. G. Purdie, I. Goykhman, G. Soavi, A. Lombardo, K. Watanabe, T. Taniguchi, M. Bonn, D. Turchinovich, C. Stampfer, A. C. Ferrari, G. Cerullo, M. Polini, and F. H. Koppens, Out-of-plane heat transfer in van der Waals stacks through electron-hyperbolic phonon coupling, *Nat. Nanotechnol.* **13**, 41 (2018).
- [18] W. Yang, S. Berthou, X. Lu, Q. Wilmart, A. Denis, M. Rosticher, T. Taniguchi, K. Watanabe, G. Fève, J.-M. Berroir *et al.*, A graphene Zener–Klein transistor cooled by a hyperbolic substrate, *Nat. Nanotechnol.* **13**, 47 (2018).
- [19] T. Sohier, M. Gibertini, and M. J. Verstraete, Remote free-carrier screening to boost the mobility of Fröhlich-limited two-dimensional semiconductors, *Phys. Rev. Mater.* **5**, 024004 (2021).
- [20] S. Dai, Z. Fei, Q. Ma, A. S. Rodin, M. Wagner, A. S. McLeod, M. K. Liu, W. Gannett, W. Regan, K. Watanabe *et al.*, Tunable phonon polaritons in atomically thin van der Waals crystals of boron nitride, *Science* **343**, 1125 (2014).
- [21] R. Fuchs and K. L. Kliewer, Optical modes of vibration in an ionic crystal slab, *Phys. Rev.* **140**, A2076 (1965).
- [22] E. N. Economou, Surface plasmons in thin films, *Phys. Rev.* **182**, 539 (1969).
- [23] M. E. Kim, A. Das, and S. D. Senturia, Electron scattering interaction with coupled plasmon-polar-phonon modes in degenerate semiconductors, *Phys. Rev. B* **18**, 6890 (1978).
- [24] B. A. Sanborn, Electron-electron interactions, coupled plasmon-phonon modes, and mobility in *n*-type GaAs, *Phys. Rev. B* **51**, 14256 (1995).
- [25] S. Fratini and F. Guinea, Substrate-limited electron dynamics in graphene, *Phys. Rev. B* **77**, 195415 (2008).
- [26] Z.-Y. Ong and M. V. Fischetti, Theory of interfacial plasmon-phonon scattering in supported graphene, *Phys. Rev. B* **86**, 165422 (2012).
- [27] A. Hauber and S. Fahy, Scattering of carriers by coupled plasmon-phonon modes in bulk polar semiconductors and polar semiconductor heterostructures, *Phys. Rev. B* **95**, 045210 (2017).
- [28] K. Andersen, S. Latini, and K. S. Thygesen, Dielectric genome of van der Waals heterostructures, *Nano Lett.* **15**, 4616 (2015).
- [29] M. N. Gjerding, L. S. R. Cavalcante, A. Chaves, and K. S. Thygesen, Efficient *Ab Initio* modeling of dielectric screening in 2D van der Waals materials: Including phonons, substrates, and doping, *J. Phys. Chem. C* **124**, 11609 (2020).
- [30] L. Sponza and F. Ducastelle, Proper *ab initio* dielectric function of 2D materials and their polarizable thickness, [arXiv:2011.07811](https://arxiv.org/abs/2011.07811).
- [31] Y. in't Veld, M. I. Katsnelson, A. J. Millis, and M. Rösner, Screening induced crossover between phonon- and plasmon-mediated pairing in layered superconductors, *2D Mater.* **10**, 045031 (2023).
- [32] W. Ma, P. Alonso-González, S. Li, A. Y. Nikitin, J. Yuan, J. Martín-Sánchez, J. Taboada-Gutiérrez, I. Amenabar, P. Li, S. Vélez *et al.*, In-plane anisotropic and ultra-low-loss polaritons in a natural van der Waals crystal, *Nature (London)* **562**, 557 (2018).
- [33] A. I. F. Tresguerres-Mata, C. Lanza, J. Taboada-Gutiérrez, J. R. Matson, G. Álvarez-Pérez, M. Isobe, A. Tarazaga Martín-Luengo, J. Duan, S. Partel *et al.*, Observation of naturally canalized phonon polaritons in LiV₂O₅ thin layers, *Nat. Commun.* **15**, 2696 (2024).
- [34] G.-Q. Hai, N. Studart, and G. E. Marques, Plasmon-phonon coupling in δ -doped polar semiconductors, *Phys. Rev. B* **55**, 1554 (1997).
- [35] S. Poncé, F. Macheda, E. R. Margine, N. Marzari, N. Bonini, and F. Giustino, First-principles predictions of Hall and drift mobilities in semiconductors, *Phys. Rev. Res.* **3**, 043022 (2021).
- [36] M. V. Fischetti, Effect of the electron-plasmon interaction on the electron mobility in silicon, *Phys. Rev. B* **44**, 5527 (1991).
- [37] V. A. Jhalani, J.-J. Zhou, J. Park, C. E. Dreyer, and M. Bernardi, Piezoelectric electron-phonon interaction from *ab initio* dynamical quadrupoles: Impact on charge transport in wurtzite GaN, *Phys. Rev. Lett.* **125**, 136602 (2020).
- [38] F. Macheda and N. Bonini, Magnetotransport phenomena in *p*-doped diamond from first principles, *Phys. Rev. B* **98**, 201201(R) (2018).
- [39] G. Brunin, Henrique Pereira Coutada Miranda, M. Giantomassi, M. Royo, M. Stengel, M. J. Verstraete, X. Gonze, G.-M. Rignanese, and G. Hautier, Electron-phonon beyond Fröhlich: Dynamical quadrupoles in polar and covalent solids, *Phys. Rev. Lett.* **125**, 136601 (2020).
- [40] F. Macheda, S. Poncé, F. Giustino, and N. Bonini, Theory and computation of Hall scattering factor in graphene, *Nano Lett.* **20**, 8861 (2020).
- [41] S. Gopalan, M. L. Van de Put, G. Gaddemane, and M. V. Fischetti, Theoretical study of electronic transport in two-dimensional transition metal dichalcogenides: Effects of the dielectric environment, *Phys. Rev. Appl.* **18**, 054062 (2022).
- [42] S. Piscanec, M. Lazzeri, F. Mauri, A. C. Ferrari, and J. Robertson, Kohn anomalies and electron-phonon interactions in graphite, *Phys. Rev. Lett.* **93**, 185503 (2004).
- [43] T. Venanzi, L. Graziotto, F. Macheda, S. Sotgiu, T. Ouaj, E. Stellino, C. Fasolato, P. Postorino, V. Mišeiškis, M. Metzelaars *et al.*, Probing enhanced electron-phonon coupling in graphene by infrared resonance Raman spectroscopy, *Phys. Rev. Lett.* **130**, 256901 (2023).
- [44] A. Grüneis, J. Serrano, A. Bosak, M. Lazzeri, S. L. Molodtsov, L. Wirtz, C. Attaccalite, M. Krisch, A. Rubio, F. Mauri, and T. Pichler, Phonon surface mapping of graphite: Disentangling

- quasi-degenerate phonon dispersions, *Phys. Rev. B* **80**, 085423 (2009).
- [45] R. Kim, V. Perebeinos, and P. Avouris, Relaxation of optically excited carriers in graphene, *Phys. Rev. B* **84**, 075449 (2011).
- [46] G. Marini and M. Calandra, Lattice dynamics of photoexcited insulators from constrained density-functional perturbation theory, *Phys. Rev. B* **104**, 144103 (2021).
- [47] M. Harb, R. Ernstorfer, T. Dartigalongue, C. T. Hebeisen, R. E. Jordan, and R. J. D. Miller, Carrier relaxation and lattice heating dynamics in silicon revealed by femtosecond electron diffraction, *J. Phys. Chem. B* **110**, 25308 (2006).
- [48] M. Bernardi, D. Vigil-Fowler, J. Lischner, J. B. Neaton, and S. G. Louie, *Ab Initio* study of hot carriers in the first picosecond after sunlight absorption in silicon, *Phys. Rev. Lett.* **112**, 257402 (2014).
- [49] A. C. Betz, S. H. Jhang, E. Pallecchi, R. Ferreira, G. Fève, J.-M. Berroir, and B. Plaças, Supercollision cooling in undoped graphene, *Nat. Phys.* **9**, 109 (2013).
- [50] J. Bardeen, L. N. Cooper, and J. R. Schrieffer, Theory of superconductivity, *Phys. Rev.* **108**, 1175 (1957).
- [51] J. R. Schrieffer, *Theory of Superconductivity*, 4th ed., Advanced Book Classics (Westview Press, Bolder, CO, 1999).
- [52] F. Marsiglio, Eliashberg theory: A short review, *Ann. Phys.* **417**, 168102 (2020).
- [53] T. Sohier, D. Campi, N. Marzari, and M. Gibertini, Mobility of 2D materials from first principles in an accurate and automated framework, *Phys. Rev. Mater.* **2**, 114010 (2018).
- [54] S. Poncé, W. Li, S. Reichardt, and F. Giustino, First-principles calculations of charge carrier mobility and conductivity in bulk semiconductors and two-dimensional materials, *Rep. Prog. Phys.* **83**, 036501 (2020).
- [55] S. Dai, Q. Ma, M. K. Liu, T. Andersen, Z. Fei, M. D. Goldflam, M. Wagner, K. Watanabe, T. Taniguchi, M. Thiemens *et al.*, Graphene on hexagonal boron nitride as a tunable hyperbolic metamaterial, *Nat. Nanotechnol.* **10**, 682 (2015).
- [56] J. Sonntag, K. Watanabe, T. Taniguchi, B. Beschoten, and C. Stampfer, Charge carrier density dependent Raman spectra of graphene encapsulated in hexagonal boron nitride, *Phys. Rev. B* **107**, 075420 (2023).
- [57] M. Yankowitz, Q. Ma, P. Jarillo-Herrero, and B. J. LeRoy, Van der Waals heterostructures combining graphene and hexagonal boron nitride, *Nat. Rev. Phys.* **1**, 112 (2019).
- [58] C. Tan, D. Adinehloo, J. Hone, and V. Perebeinos, Phonon-limited mobility in h-BN encapsulated AB-stacked bilayer graphene, *Phys. Rev. Lett.* **128**, 206602 (2022).
- [59] T. Sohier, VED, GitLab repository, available at <https://gitlab.com/tsohier/ved> (2024).
- [60] M. Royo and M. Stengel, Exact long-range dielectric screening and interatomic force constants in quasi-two-dimensional crystals, *Phys. Rev. X* **11**, 041027 (2021).
- [61] We can now clarify the meaning of the dual basis set in mathematical terms: At each fixed z , χ_{iL} is an element of the dual space of the potentials. The separability of χ_{iL} and the property $\chi_{iL}(q, \omega, z, z') = (\chi_{iL}(q, \omega, z', z))^*$ imply that the basis set of the densities is the same as of the dual space, justifying our nomenclature choice.
- [62] G. Grosso and G. Pastori Parravicini, *Solid State Physics* (Academic Press, San Diego, CA, 2000).
- [63] T. Sohier, M. Calandra, C.-H. C.-H. Park, N. Bonini, N. Marzari, and F. Mauri, Phonon-limited resistivity of graphene by first-principles calculations: Electron-phonon interactions, strain-induced gauge field, and Boltzmann equation, *Phys. Rev. B* **90**, 125414 (2014).
- [64] T. Sohier, M. Calandra, and F. Mauri, Density-functional calculation of static screening in two-dimensional materials: The long-wavelength dielectric function of graphene, *Phys. Rev. B* **91**, 165428 (2015).
- [65] F. Macheda, T. Sohier, P. Barone, and F. Mauri, Electron-phonon interaction and phonon frequencies in two-dimensional doped semiconductors, *Phys. Rev. B* **107**, 094308 (2023).
- [66] V. U. Nazarov, Electronic excitations in quasi-2D crystals: What theoretical quantities are relevant to experiment? *New J. Phys.* **17**, 073018 (2015).
- [67] K. Sturm, Dynamic structure factor: An introduction, *Z. Naturforsch. A: Phys. Sci.* **48**, 233 (1993).
- [68] R. Senga, K. Suenaga, P. Barone, S. Morishita, F. Mauri, and T. Pichler, Position and momentum mapping of vibrations in graphene nanostructures in the electron microscope, *Nature (London)* **573**, 247 (2019).
- [69] G. D. Mahan, *Many-Particle Physics*, 2nd ed., Physics of Solids and Liquids (Plenum Press, New York, NY, 1990).
- [70] A. N. Grigorenko, M. Polini, and K. S. Novoselov, Graphene plasmonics, *Nat. Photonics* **6**, 749 (2012).
- [71] A. Politano and G. Chiarello, Plasmon modes in graphene: Status and prospect, *Nanoscale* **6**, 10927 (2014).
- [72] E. H. Hwang and S. Das Sarma, Dielectric function, screening, and plasmons in two-dimensional graphene, *Phys. Rev. B* **75**, 205418 (2007).
- [73] M. Polini, R. Asgari, G. Borghi, Y. Barlas, T. Pereg-Barnea, and A. H. MacDonald, Plasmons and the spectral function of graphene, *Phys. Rev. B* **77**, 081411(R) (2008).
- [74] A. Hill, S. A. Mikhailov, and K. Ziegler, Dielectric function and plasmons in graphene, *Europhys. Lett.* **87**, 27005 (2009).
- [75] A. Principi, G. Vignale, M. Carrega, and M. Polini, Intrinsic lifetime of Dirac plasmons in graphene, *Phys. Rev. B* **88**, 195405 (2013).
- [76] A. Principi, M. Carrega, M. B. Lundeberg, A. Woessner, F. H. L. Koppens, G. Vignale, and M. Polini, Plasmon losses due to electron-phonon scattering: The case of graphene encapsulated in hexagonal boron nitride, *Phys. Rev. B* **90**, 165408 (2014).
- [77] K. Zhang, Y. Feng, F. Wang, Z. Yang, and J. Wang, Two-dimensional hexagonal boron nitride (2D-hBN): Synthesis, properties and applications, *J. Mater. Chem. C* **5**, 11992 (2017).
- [78] J. D. Caldwell, I. Aharonovich, G. Cassabois, J. H. Edgar, B. Gil, and D. N. Basov, Photonics with hexagonal boron nitride, *Nat. Rev. Mater.* **4**, 552 (2019).
- [79] Z. Shi, H. A. Bechtel, S. Berweger, Y. Sun, B. Zeng, C. Jin, H. Chang, M. C. Martin, M. B. Raschke, and F. Wang, Amplitude- and phase-resolved nanospectral imaging of phonon polaritons in hexagonal boron nitride, *ACS Photonics* **2**, 790 (2015).
- [80] S. Dai, W. Fang, N. Rivera, Y. Stehle, B.-Y. Jiang, J. Shen, R. Y. Tay, C. J. Ciccarino, Q. Ma, D. Rodan-Legrain *et al.*, Phonon polaritons in monolayers of hexagonal boron nitride, *Adv. Mater.* **31**, 1806603 (2019).

- [81] D. Sánchez-Portal and E. Hernández, Vibrational properties of single-wall nanotubes and monolayers of hexagonal BN, *Phys. Rev. B* **66**, 235415 (2002).
- [82] K. H. Michel and B. Verberck, Theory of elastic and piezoelectric effects in two-dimensional hexagonal boron nitride, *Phys. Rev. B* **80**, 224301 (2009).
- [83] T. Sohier, M. Gibertini, M. Calandra, F. Mauri, and N. Marzari, Breakdown of optical phonons' splitting in two-dimensional materials, *Nano Lett.* **17**, 3758 (2017).
- [84] J. Li, L. Wang, Y. Wang, Z. Tao, W. Zhong, Z. Su, S. Xue, G. Miao, W. Wang, H. Peng, J. Guo, and X. Zhu, Observation of the nonanalytic behavior of optical phonons in monolayer hexagonal boron nitride, *Nat. Commun.* **15**, 1938 (2024).
- [85] K. S. Novoselov, A. K. Geim, S. V. Morozov, D. Jiang, Y. Zhang, S. V. Dubonos, I. V. Grigorieva, and A. A. Firsov, Electric field effect in atomically thin carbon films, *Science* **306**, 666 (2004).
- [86] F. Schwierz, Graphene transistors, *Nat. Nanotechnol.* **5**, 487 (2010).
- [87] A. C. Ferrari, F. Bonaccorso, V. Fal'ko, K. S. Novoselov, S. Roche, P. Bøggild, S. Borini, F. H. L. Koppens, V. Palermo, N. Pugno *et al.*, Science and technology roadmap for graphene, related two-dimensional crystals, and hybrid systems, *Nanoscale* **7**, 4598 (2015).
- [88] G. Giuliani and G. Vignale, *Quantum Theory of the Electron Liquid* (Cambridge University Press, Cambridge, UK, 2005).
- [89] S. Q. Wang and G. D. Mahan, Electron scattering from surface excitations, *Phys. Rev. B* **6**, 4517 (1972).
- [90] C. Attaccalite, L. Wirtz, M. Lazzeri, F. Mauri, and A. Rubio, Doped graphene as tunable electron-phonon coupling material, *Nano Lett.* **10**, 1172 (2010).
- [91] L. Graziotto, F. Macheda, T. Sohier, M. Calandra, and F. Mauri, Theory of infrared double-resonance Raman spectrum in graphene: The role of the zone-boundary electron-phonon enhancement, *Phys. Rev. B* **109**, 075420 (2024).
- [92] L. Graziotto, F. Macheda, T. Venanzi, G. Marchese, S. Sotgiu, T. Ouaj, E. Stellino, C. Fasolato, P. Postorino, M. Metzelaars *et al.*, Infrared resonance Raman of bilayer graphene: Signatures of massive fermions and band structure on the 2D peak, *Nano Lett.* **24**, 1867 (2024).
- [93] L. Banszerus, T. Sohier, A. Epping, F. Winkler, F. Libisch, F. Haupt, K. Watanabe, T. Taniguchi, K. Müller-Caspary, N. Marzari, F. Mauri, B. Beschoten, and C. Stampfer, Extraordinary high room-temperature carrier mobility in graphene-WSe₂ heterostructures, [arXiv:1909.09523](https://arxiv.org/abs/1909.09523).
- [94] L. Wang, I. Meric, P. Y. Huang, Q. Gao, Y. Gao, H. Tran, T. Taniguchi, K. Watanabe, L. M. Campos, D. A. Muller *et al.*, One-dimensional electrical contact to a two-dimensional material, *Science* **342**, 614 (2013).
- [95] T. Sohier, M. Gibertini, and N. Marzari, Profiling novel high-conductivity 2D semiconductors, *2D Mater.* **8**, 015025 (2020).
- [96] K. Kaasbjerg, K. S. Thygesen, and K. W. Jacobsen, Phonon-limited mobility in *n*-type single-layer MoS₂ from first principles, *Phys. Rev. B* **85**, 115317 (2012).
- [97] S. Poncé, M. Royo, M. Gibertini, N. Marzari, and M. Stengel, Accurate prediction of Hall mobilities in two-dimensional materials through gauge-covariant quadrupolar contributions, *Phys. Rev. Lett.* **130**, 166301 (2023).
- [98] C. Zhang, R. Wang, H. Mishra, and Y. Liu, Two-dimensional semiconductors with high intrinsic carrier mobility at room temperature, *Phys. Rev. Lett.* **130**, 087001 (2023).
- [99] L. Cheng, C. Zhang, and Y. Liu, Intrinsic charge carrier mobility of 2D semiconductors, *Comput. Mater. Sci.* **194**, 110468 (2021).
- [100] X. Duan, T. Wang, Z. Fu, L. Liu, and J.-Y. Yang, Nontrivial role of polar optical phonons in limiting electron mobility of two-dimensional Ga₂O₃ from first-principles, *Phys. Chem. Chem. Phys.* **25**, 10175 (2023).
- [101] J. Ma, D. Xu, R. Hu, and X. Luo, Examining two-dimensional Fröhlich model and enhancing the electron mobility of monolayer InSe by dielectric engineering, *J. Appl. Phys.* **128**, 035107 (2020).
- [102] L. Cheng and Y. Liu, What limits the intrinsic mobility of electrons and holes in two dimensional metal dichalcogenides? *J. Am. Chem. Soc.* **140**, 17895 (2018).
- [103] S. Song, Y. Sun, S. Liu, J.-H. Yang, and X.-G. Gong, General rules and applications for screening high phonon-limited mobility in two-dimensional semiconductors, *Phys. Rev. B* **107**, 155101 (2023).
- [104] W. Li, S. Poncé, and F. Giustino, Dimensional crossover in the carrier mobility of two-dimensional semiconductors: The case of InSe, *Nano Lett.* **19**, 1774 (2019).
- [105] N. Ma and D. Jena, Charge scattering and mobility in atomically thin semiconductors, *Phys. Rev. X* **4**, 011043 (2014).
- [106] T. Sohier, M. Gibertini, D. Campi, G. Pizzi, and N. Marzari, Valley-engineering mobilities in two-dimensional materials, *Nano Lett.* **19**, 3723 (2019).
- [107] C.-H. Park, N. Bonini, T. Sohier, G. Samsonidze, B. Kozinsky, M. Calandra, F. Mauri, and N. Marzari, Electron-phonon interactions and the intrinsic electrical resistivity of graphene, *Nano Lett.* **14**, 1113 (2014).
- [108] S.-C. Lee and I. Galbraith, Intersubband and intrasubband electronic scattering rates in semiconductor quantum wells, *Phys. Rev. B* **59**, 15796 (1999).
- [109] T. Sohier, E. Ponomarev, M. Gibertini, H. Berger, N. Marzari, N. Ubrig, and A. F. Morpurgo, Enhanced electron-phonon interaction in multivalley materials, *Phys. Rev. X* **9**, 031019 (2019).
- [110] R. de L. Kronig, On the theory of dispersion of x-rays, *J. Optic. Soc. Amer.* **12**, 547 (1926).
- [111] F. Macheda, P. Barone, and F. Mauri, Electron-phonon interaction and longitudinal-transverse phonon splitting in doped semiconductors, *Phys. Rev. Lett.* **129**, 185902 (2022).
- [112] L. Hedin and S. Lundqvist, Effects of electron-electron and electron-phonon interactions on the one-electron states of solids, in *Solid State Physics* (Elsevier, Amsterdam, 1970), Vol. 23, pp. 1–181.
- [113] O. V. Dolgov, D. A. Kirzhnits, and E. G. Maksimov, On an admissible sign of the static dielectric function of matter, *Rev. Mod. Phys.* **53**, 81 (1981).
- [114] A. E. Karakozov and E. G. Maksimov, Influence of anharmonicity on superconductivity, *Sov. Phys. JETP (English translation)* **47**, 2 (1978).
- [115] L. Binci, P. Barone, and F. Mauri, First-principles theory of infrared vibrational spectroscopy of metals and semimetals: Application to graphite, *Phys. Rev. B* **103**, 134304 (2021).

- [116] G. Marchese, F. Macheda, L. Binci, M. Calandra, P. Barone, and F. Mauri, Born effective charges and vibrational spectra in superconducting and bad conducting metals, *Nat. Phys.* **20**, 88 (2023).
- [117] C. E. Dreyer, S. Coh, and M. Stengel, Nonadiabatic born effective charges in metals and the Drude weight, *Phys. Rev. Lett.* **128**, 095901 (2022).
- [118] C.-Y. Wang, S. Sharma, E. K. U. Gross, and J. K. Dewhurst, Dynamical Born effective charges, *Phys. Rev. B* **106**, L180303 (2022).
- [119] H. Fröhlich, Electrons in lattice fields, *Adv. Phys.* **3**, 325 (1954).
- [120] J. Sjakste, N. Vast, M. Calandra, and F. Mauri, Wannier interpolation of the electron-phonon matrix elements in polar semiconductors: Polar-optical coupling in GaAs, *Phys. Rev. B* **92**, 054307 (2015).
- [121] C. Verdi and F. Giustino, Fröhlich electron-phonon vertex from first principles, *Phys. Rev. Lett.* **115**, 176401 (2015).
- [122] P. Vogl, Microscopic theory of electron-phonon interaction in insulators or semiconductors, *Phys. Rev. B* **13**, 694 (1976).
- [123] R. M. Pick, M. H. Cohen, and R. M. Martin, Microscopic theory of force constants in the adiabatic approximation, *Phys. Rev. B* **1**, 910 (1970).
- [124] S. Poncé, M. Royo, M. Stengel, N. Marzari, and M. Gibertini, Long-range electrostatic contribution to electron-phonon couplings and mobilities of two-dimensional and bulk materials, *Phys. Rev. B* **107**, 155424 (2023).
- [125] F. Giustino, Electron-phonon interactions from first principles, *Rev. Mod. Phys.* **89**, 015003 (2017).
- [126] C. Verdi, F. Caruso, and F. Giustino, Origin of the crossover from polarons to Fermi liquids in transition metal oxides, *Nat. Commun.* **8**, 15769 (2017).
- [127] F. Caruso and F. Giustino, Theory of electron-plasmon coupling in semiconductors, *Phys. Rev. B* **94**, 115208 (2016).
- [128] P. Giannozzi, S. Baroni, N. Bonini, M. Calandra, R. Car, C. Cavazzoni, D. Ceresoli, G. L. Chiarotti, M. Cococcioni, I. Dabo *et al.*, QUANTUM ESPRESSO: A modular and open-source software project for quantum simulations of materials, *J. Phys.: Condens. Matter* **21**, 395502 (2009).
- [129] P. Giannozzi Jr., O. Andreussi, T. Brumme, O. Bunau, M. Buongiorno Nardelli, M. Calandra, R. Car, C. Cavazzoni, D. Ceresoli, M. Cococcioni *et al.*, Advanced capabilities for materials modeling with QUANTUM ESPRESSO, *J. Phys.: Condens. Matter* **29**, 465901 (2017).
- [130] T. Sohler, M. Calandra, and F. Mauri, Density functional perturbation theory for gated two-dimensional heterostructures: Theoretical developments and application to flexural phonons in graphene, *Phys. Rev. B* **96**, 075448 (2017).
- [131] D. R. Hamann, Optimized norm-conserving Vanderbilt pseudopotentials, *Phys. Rev. B* **88**, 085117 (2013).
- [132] M. J. van Setten, M. Giantomassi, E. Bousquet, M. J. Verstraete, D. R. Hamann, X. Gonze, and G. M. Rignanese, The PSEUDOJOJO: Training and grading a 85 element optimized norm-conserving pseudopotential table, *Comput. Phys. Commun.* **226**, 39 (2018).
- [133] T. Zhan, X. Shi, Y. Dai, X. Liu, and J. Zi, Transfer matrix method for optics in graphene layers, *J. Phys.: Condens. Matter* **25**, 215301 (2013).
- [134] S. Dai, J. Quan, G. Hu, C.-W. Qiu, T. H. Tao, X. Li, and A. Alù, Hyperbolic phonon polaritons in suspended hexagonal boron nitride, *Nano Lett.* **19**, 1009 (2019).
- [135] P. Cudazzo, I. V. Tokatly, and A. Rubio, Dielectric screening in two-dimensional insulators: Implications for excitonic and impurity states in graphane, *Phys. Rev. B* **84**, 085406 (2011).
- [136] A. Guandalini, R. Senga, Y.-C. Lin, K. Suenaga, P. Barone, F. Mauri, T. Pichler, and C. Kramberger, Direct observation of the vanishing EELS cross section in graphene, [arXiv:2406.02998](https://arxiv.org/abs/2406.02998).